Ply Drop-off Regions within Thermoset Composites

Influence of ply drop-off regions on the cure-induced residual stress development within thermoset composites manufactured by resin transfer moulding

T.M.J. van Loon

MSc. Thesis
Faculty of Aerospace Engineering
Delft University of Technology

TU Delft

Ply Drop-off Regions within Thermoset Composites

Influence of ply drop-off regions on the cure-induced residual stress development within thermoset composites manufactured by liquid transfer moulding

by

T.M.J. van Loon

to obtain the degree of Master of Science
at the Delft University of Technology,
to be defended publicly on Friday May 28, 2021 at 01:00 PM.

Student number:	4615123	
Project duration:	September 2, 2019 – May 14, 2021	
Thesis committee:	Prof. ir. Clemens A. Dransfeld,	TU Delft, chair holder
	Asst. Prof. dr. ir. Julie J.E. Teuwen,	TU Delft, supervisor
	Dr. ir. Julien M.J.F. van Campen,	TU Delft, examiner
	Ir. Peet A.M. Vergouwen,	GKN Aerospace, supervisor

TU Delft

Fokker

GKN AEROSPACE

Preface

With this thesis I am concluding my period as student at the Delft University of Technology by receiving a master's degree in Aerospace Engineering. After completing my literature review last year, I did not realise how difficult the upcoming period would be. Not only due to all the COVID-19 circumstances which made it more challenging, but also because the directions in which my research would continue were not always straightforward to me. Nevertheless, I am very satisfied with the final result and I am proud that I made it through the end.

First of all, I would like to thank the colleagues at GKN - Fokker Landing Gear B.V. Although the circumstances unfortunately changed the way I finished my thesis project, the times I was allowed to be present at the company were always pleasant. My special thanks goes to my daily supervisor, Peet Vergouwen, who gave me the opportunity to work on my thesis project within his department. By challenging me to be critical when interpreting results, but more important reminding me often to put things in perspective whenever I got lost in detail, I have learned more from this project than I could imagine at first.

I would also like to express my gratitude to my TU Delft supervisor, Julie Teuwen, whom provided me with critical, but very helpful feedback which improved both my thesis and academic skills in various ways. Even though most contact moments were digital, her guidance did not become less valuable. I also want to thank Giacomo Struzziero, as he was always available to discuss the difficulties I encountered during the initial part of my research project.

Last but not least, I would like to thank my girlfriend, friends in Dongen and Delft, and family for the continuous support and encouragement throughout the entire project. Without all this, I cannot imagine I would have been able to finish this thesis.

T.M.J. van Loon
Dongen (NL), May 2021

Summary

Laminate distortions around ply drop-off regions were observed by GKN - Fokker Landing Gear B.V. as result of the cure phase, which is part of the Resin Transfer Moulding (RTM) process. The necessity of implementing ply drop-off regions originates from thickness transitions within their composite landing gear parts. The aim of this study is to analyse the influence of ply drop-off regions and related parameters such as the pocket geometry, laminate design and cure cycle, to obtain a more thoroughly understanding regarding the cure-induced residual stress generation and distortions around these regions.

RTM can be categorized under Liquid Composite Moulding, which is based on the injection or drawing of a low viscosity thermoset resin into a dry-fibre preform which is enclosed in a sealed cavity between multiple moulding parts and cured afterwards. Vacuum-Assisted RTM (VARTM) differs from this process by requiring one single-sided mould with a flexible vacuum bag. The cure phase implies the polymerization reaction of the resin, where monomers are bonded by chemical cross-links into a single continuous molecular structure. As result of this reaction, for which the progression can be expressed in Degree of Cure (DOC), volumetric shrinkage and changes in thermal-chemical and thermal-mechanical properties of the resin take place. This together with differences in thermal expansion and contraction causes the fundamental mechanisms of cure-induced residual stress within composite laminates. Out-of-plane tensile stress is the most detrimental concerning process defects such as ply delamination and matrix cracking, which becomes even more critical around ply drop-off regions as these have been identified as discontinuities and therefore stress risers. The resin pocket, resulting from the ply termination within this drop-off, can be idealized by a right-angled triangle in which the aspect ratio defines the height and base length. When multiple drop-off regions are implemented, the stagger distance defines the distance between each drop-off.

Cure simulations has been carried out by using a thermal-mechanical Finite Element Analysis (FEA) model, established within the FEA environment Abaqus and coupled with multiple user subroutines. All thermal-chemical and thermal-mechanical material properties of the composite constituents are included, where most are dependent on time, temperature and DOC. Verification of the model was accomplished by comparing both final stress and warpage predictions with a study considering cure-induced warpage in thermoset laminates manufactured by VARTM and validated by experiments. It was concluded that the thermal-mechanical model was suitable as basis for the ply drop-off models required for this study. Multiple models were created, based on single and multiple drop-off regions being implemented within thin- and thick composite laminates. Two different topologies were used for the multiple drop-off regions, based on either a common core- or belt ply. As different parameters were investigated, material properties, resin pocket geometry, ply orientations, cure temperature profiles and stagger distance all were implemented as variable. Required boundary conditions related to VARTM were kept equal for each model.

Varying resin pocket material properties showed that during the heating stage the thermal expansion and chemical shrinkage evolve in counteracting manner. As result, an almost stress-free state was present at the end of this stage. Chemical shrinkage surpasses the thermal expansion throughout the dwell stage, where combined with thermal contraction during cool down it results in significant out-of-plane stress built-up within the core- and belt ply. The geometry of the resin pocket was varied together with the ply orientation of the laminate. Increased out-of-plane tenisle stress levels were observed for both an increasing aspect ratio and in-plane stiffness in the drop-off direction of the core- and belt ply. The orientation of the terminated ply also appeared to be of influence, as large in-plane tensile stress regions within this ply resulted in increased stress levels. As stress levels only became significant from upon the dwell stage, the dwell temperature and cool down rate were both selected to be analysed regarding its influence on stress development. Prior to analysing these process parameters, the transition to thick laminates was evaluated, which only resulted in stress increases related to the already observed influencing ply orientations. An increased cool down rate resulted in lower final stress

values. This effect originated from postponing and therefore lowering vitrification temperatures, which resulted in less thermal contraction in glassy state of the resin during cool down. A distinct relation between dwell temperature and stress increases could only be observed via the DOC, where higher dwell temperatures resulted in increased DOC and subsequently stress levels.

By implementing multiple drop-offs, the influence of stagger distance and stress interactions within these regions as result of different ply orientations were analysed. It was found that even when stress interactions are neglected, implementing multiple drop-offs results in higher stress levels at the 1st drop-off, and lower stress levels at the 2nd and 3rd drop-off, compared to a single drop-off implementation. When including different ply orientations for common core ply topologies, all stress levels appeared higher than the single drop-off, where at the 1st drop-off the stress decreases, and at the 2nd and 3rd drop-off it increases with increasing stagger distance. Stress levels within multiple drop-off regions using common belt ply topologies were more in line with the results when stress interactions were neglected. Where stress levels at the 1st drop-off significantly increased, stress levels at the 2nd and 3rd drop-off remained lower than the single drop-off. Only minor decreases at the 1st drop-off and increases at the 2nd drop-off in stress were observed with increasing stagger distance, where only at the 3rd drop-off stress levels increased to single drop-off values. The influencing stress interactions were mainly based on increased in-plane tensile stress regions between-, and decreased in-plane compressive stress regions above and below drop-offs. These regions were of influence whenever these occurred near the resin pocket within core- and belt ply.

It can be concluded that multiple influences on the cure-induced stress around ply drop-off regions can be identified. As result of the material property evolutions of the resin pocket, stress levels only become significant during the dwell- and cool down stage, which are therefore more critical. For the latter stage, higher cool down rates decreases the final stress levels. Furthermore, ply orientations are of influence by resulting in higher final stress levels with increased in-plane stiffness of the surrounding plies in the drop-off direction. This effect is further increased whenever high in-plane tensile stress regions occur within the terminated ply, resulting from higher in-plane shrinkage and contraction in the drop-off direction. Multiple drop-off regions introduce stress interactions whenever different ply orientations are implemented. These interactions introduce in-plane tensile- and compressive stress regions around drop-offs, which increase and decrease the maximum out-of-plane stress, respectively. These regions become less effective with increasing stagger distance.

From these conclusions multiple design guidelines were formulated, which can be used for future implementation of drop-off regions to avoid undesired stress increase. These guidelines consist of selecting ply orientations to reduce local stress interactions which can increase the stress levels within drop-off regions. Also, these guidelines include selecting process parameters as such to avoid unnecessary cure-induced stress generation and selecting the least critical multiple drop-off topology.

Contents

List of Figures

List of Tables

List of Acronyms

CFRP	Carbon Fibre Reinforced Polymer
CTE	Coefficient of Thermal Expansion
DOC	Degree of Cure
DSC	Differential Scanning Calorimetry
FDM	Finite Difference Method
FEA	Finite Element Analysis
FLG	GKN - Fokker Landing Gear B.V.
FVF	Fibre Volume Fraction
LCM	Liquid Composite Moulding
MRCC	Manufacturer Recommended Cure Cycle
NCF	Non-crimp fabric
RTM	Resin Transfer Moulding
SDV	Solution Dependent State Variable
Tg	Glass transition temperature
TS	Thermosetting
VARTM	Vacuum-Assisted RTM

List of Symbols

E_l	Young's modulus composite, longitudinal direction	GPa
E_r	Young's modulus resin	GPa
E_t	Young's modulus composite, transverse direction	GPa
E_{glassT}	Temperature dependency of Young's modulus resin in glassy state	GPa °C^{-1}
E_{glass}	Young's modulus resin, glassy state	GPa
E_{lf}	Young's modulus fibre, longitudinal direction	GPa
E_{rub}	Young's modulus resin, rubbery state	GPa
E_{tf}	Young's modulus fibre, transverse direction	GPa
G_r	Shear modulus resin	GPa
G_{12f}	Shear modulus fibre, in-plane direction	GPa
G_{12}	Shear modulus composite, in-plane direction	GPa
H_T	Total reaction heat	J kg^{-1}
K_l	Thermal conductivity composite, longitudinal direction	W m^{-1} °C^{-1}
K_r	Thermal conductivity resin	W m^{-1} °C^{-1}
K_t	Thermal conductivity composite, transverse direction	W m^{-1} °C^{-1}
K_{lf}	Thermal conductivity fibre, longitudinal direction	W m^{-1} °C^{-1}
K_{tf}	Thermal conductivity fibre, transverse direction	W m^{-1} °C^{-1}
T_g	Instantaneous glass transition temperature	°C
T_{g0}	Glass transition temperature unreacted resin	°C
$T_{g\infty}$	Glass transition temperature fully cured resin	°C
α	Degree of cure	-
α_T	Temperature dependency of degree of cure	°C^{-1}
α_c	Critical degree of cure	-
α_{c0}	Critical degree of cure at absolute zero temperature	-
$\dot{Q}$	Heat generation per unit time and volume	J m^{-3} s^{-1}
γ_α	Maximum resin shrinkage	-
γ_l	Shrinkage composite, longitudinal direction	-
γ_r	Resin shrinkage	-
γ_t	Shrinkage composite, transverse direction	-
ν_r	Poisson's ratio resin	-
ν_{12f}	Poisson's ratio fibre, in-plane direction	-
ν_{12}	Poisson's ratio composite, in-plane direction	-
ν_{glass}	Poisson's ratio resin, glassy state	-
ν_{rub}	Poisson's ratio resin, rubbery state	-
ρ_c	Density composite	kg m^{-3}
ρ_f	Density fibre	kg m^{-3}
ρ_r	Density resin	kg m^{-3}
σ_v	Von Mises stress	MPa
σ_{11}	In-plane direct stress, longitudinal direction	MPa
σ_{33}	Out-of-plane direct stress	MPa
ε	Total strain	-
ε^M	Mechanical strain	-

ε^{Sh}	Chemical strain	-
ε^{T}	Thermal strain	-
a_l	Coefficient of thermal expansion composite, longitudinal direction	$°C^{-1}$
a_r	Coefficient of thermal expansion resin	$°C^{-1}$
a_t	Coefficient of thermal expansion composite, transverse direction	$°C^{-1}$
a_{lf}	Coefficient of thermal expansion fibre, longitudinal direction	$°C^{-1}$
a_{tf}	Coefficient of thermal expansion fibre, transverse direction	$°C^{-1}$
$c_{p,c}$	Specific heat capacity composite	$J\,g^{-1}\,°C^{-1}$
$c_{p,f}$	Specific heat capacity fibre	$J\,g^{-1}\,°C^{-1}$
$c_{p,r}$	Specific heat capacity resin	$J\,g^{-1}\,°C^{-1}$
t	Time	s
v_f	Fibre volume fraction	-
v_r	Resin volume fraction	-
w_f	Weight fraction fibre	-

1 Introduction

Within section 1.1 the project background is given together with the motivation why this project is initiated. Hereafter, the proposed research questions are presented in section 1.2. These are based on the research gap which resulted from the literature review described in chapter 2. Section 1.3 provides the thesis outline for this report.

1.1. Project Motivation

The use of composite materials within the aeronautical industry has grown considerably for the past couple of decades [1]. The success of this type of material is mainly due to their superior strength to weight ratio which can result in significant weight savings in the primary load-carrying structures [1, 2]. With the demand for these composite materials to be used as primary structures, the complexity and high end-quality of these parts is generally the main challenge during manufacturing [2]. Because these parts require continuous reinforcing fibres to ensure high structural performance, the Resin Transfer Moulding (RTM) process was introduced from the automotive industry and adapted for composite manufacturing to produce high quality, net-shaped parts [3]. This RTM process knows many variations but the fundamental steps are based on the injection of low viscosity thermoset resin under high pressure in a closed-cavity mould in which dry-fibre preforms are fixated and enclosed. This injection is followed by a cure phase and results in a nearly net-shaped part which consist of multiple resin-enclosed continuous fibre layers with different orientations that are combined within a single laminate. During this cure phase, multiple material properties change as result of the chemical cross-linking reaction of the resin. The combination of these changes of material properties and the material properties being anisotropic for continuous-fibre composite materials, can result in residual stress generation within the part. When these stresses increase significantly, which is often the effect whenever the thickness of the part increases, distortions and process-induced defects within the laminate can be the result.

This research project is initiated on behalf of GKN - Fokker Landing Gear B.V. (FLG), which is conducting research and development on the design and prototyping of thick-walled Carbon Fibre Reinforced Polymer (CFRP) structures, such as landing gear components, to make their entry in industry. As result of the cure phase being part of the used RTM manufacturing process, different types of laminate distortions around ply drop-off regions within their parts are observed. The ply drop-off is introduced whenever a single laminate layer, knows as the ply, is terminated with the aim to change the overall thickness and mechanical properties of the laminate. The necessity of ply drop-off regions originates from the transition between the constant thickness mid-section region and the end-sections of the composite landing gear parts, where for these latter sections the thickness must be larger at the flanges to ensure load transfer via the composite lug sections. An example of these complex parts is illustrated in figure 1.1, where the difference in overall thickness can be observed between the lugs that are connected to the mid-section and end-section. By analysing the different influencing parameters such as the resin pocket geometry, laminate design and cure cycle, a more thoroughly understanding of the influence of these parameters on the residual stress generation and related distortions around ply drop-off regions can be achieved. This can help the company during the design phase of their components.

Figure 1.1: CFRP drag stay for the A350-1000, designed by FLG and NLR. Obtained from [4]

1.2. Research Questions

For this project, the main research question is stated as follows:

> 'What is the influence of ply drop-off regions and related process and laminate parameters within thick composite laminates on the cure-induced residual stress generation and related distortions as result of RTM manufacturing processes?'

Based on this main research question, multiple sub-questions are proposed. By answering all these sub-questions individually, a structured approach towards the result of this research project can be ensured. In addition, using the answers of these sub-questions, a well-argued concluding answer on the main research question can be given. The following listing are the proposed sub-questions with each having one or multiple fundamental questions underneath.

1. What is the influence of ply drop-off regions within fibre-reinforced laminates on the cure-induced residual stress and resulting laminate distortions?
   (a) What is the effect of cure-induced residual stress on laminate distortions without the application of ply drop-off regions?
   (b) What is the change in the effect on cure-induced residual stress with the implementation of ply drop-off regions compared to constant thickness laminates?
   (c) What is the influence of the material property evolutions of the resin pocket as result of the cure process?
   (d) What is the influence of the geometry of the resin pocket?
2. How do the laminate- and process parameters influence the cure-induced residual stress and related distortions resulting from ply drop-off regions?
   (a) How do the ply parameters influence the cure-induced residual stress around ply drop-off regions?
   (b) How do the process parameters influence the cure-induced residual stress around ply drop-off regions?
3. What is the influence of multiple ply drop-off regions on the cure-induced residual stress within laminates?
   (a) What interactions caused by ply orientations are introduced as result of the cure-induced residual stress around multiple ply drop-off regions?
   (b) What is the influence of the topology + stagger distance between ply drop-off regions on these interactions?

1.3. Thesis Outline

The literature review conducted for this research study in presented in chapter 2. Within this chapter an introduction to RTM and a detailed description of the cure phase is given. In addition, the physics and governing equations to describe the cure phase, and the fundamental mechanisms of cure-induced residual stress are included. In chapter 3 the implementation of all material models required for the coupled thermal-mechanical cure model are presented. The sensitivity analysis and verification of this model are included at the end of this chapter. Chapter 4 describes each ply drop-off model which is used for this study, together with the required model assumptions and mesh convergence studies. In chapter 5 all results concerning implementation of single ply drop-off regions within thin- and thick laminates are presented. The results obtained by implementing multiple ply drop-off regions using two different topologies are presented in chapter 6. In chapter 7 the conclusions based on the obtained observations are given together with answers to the research questions. In addition, multiple design guidelines to reduce cure-induced residual stress around ply drop-off regions are proposed. This report is ended with recommendations for further research.

2

Literature Review

Within section 2.1 an introduction to the RTM process is given. Section 2.2 includes a more detailed elaboration on the cure phase. Mechanisms causing cure-induced residual stress are described within section 2.3. Section 2.4 focuses on cure phase simulations, where distinction is made between thermal-chemical and thermal-mechanical modelling. An introduction to ply drop-off regions and the most relevant research studies are discussed within section 2.5.

2.1. An Introduction to Resin Transfer Moulding

RTM is a production method which can be categorized under the Liquid Composite Moulding (LCM) process [3]. LCM is based on the principle of the injection or drawing of a low viscosity resin into a dry-fibre preform which is enclosed in a sealed cavity between two or more matching rigid mould parts [1, 3]. Within the LCM industry, generally only Thermosetting (TS) resins are involved for the manufacturing of composite parts due to its low viscosity and therefore better injection and flow capabilities required for RTM [3]. Although thermoplastic resins with low viscosity do exist and the interest to use these materials within LCM increases, the scope of this literature review is limited to TS matrix materials only [5, 6].

RTM originates from the automotive industry, where the high volume and net-shaped production potential were the main benefits [3]. Primarily, this process was used for injection moulding of resin into short-fibre fabric material, depicted by figure a within figure 2.1.

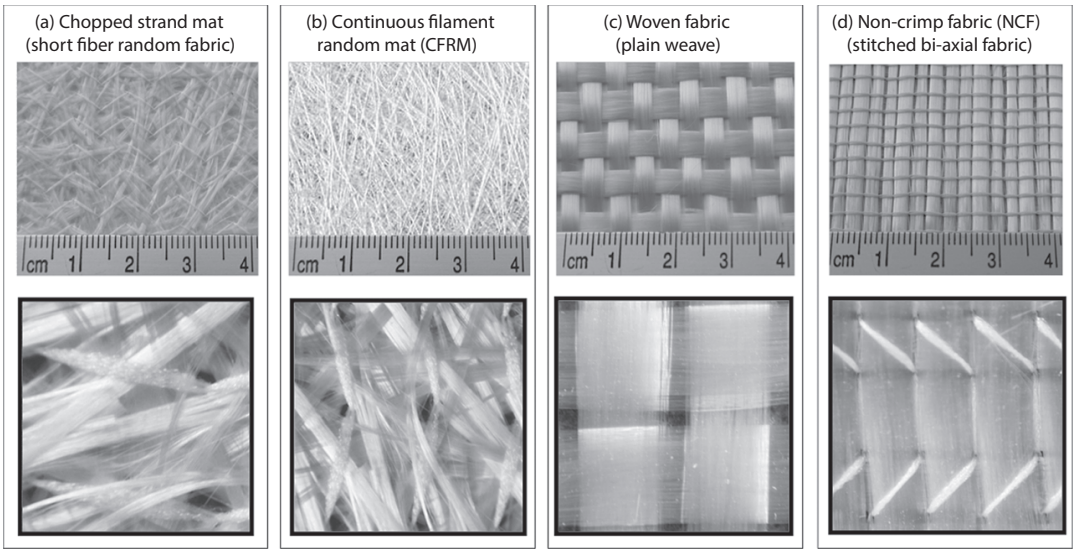

Figure 2.1: Common fibre mats and fabrics used in LCM. Obtained and modified from [3]

Structural parts with this type of reinforcement could not meet the aerospace performance and quality standards [3]. Therefore, continuous-fibre preforms were implemented as these effectively increase the load transfer through the fibres, and as result improve the overall strength and stiffness of the part along the required load transfer directions. These continuous reinforcements can be implemented using randomly orientated mats, illustrated by figure b in figure 2.1, or fabrics such as woven fabrics and Non-crimp fabrics (NCFs), depicted by figure c and d within figure 2.1, respectively. In general, using NCFs a higher Fibre Volume Fraction (FVF) and better in-plane mechanical properties can be obtained compared to woven fabrics [3].

The main steps of RTM can be described using figure 2.2. The first step is the fabrication of the dry-fibre preforms. Subsequently, these are placed according to the prescribed layup and draped on one or multiple mould parts. After fixation of this preform, mould closure is accomplished after which the liquid resin matrix material can be injected under pressure via one or multiple injection inlet ports to end up with a completely impregnated preform. Hereafter, the cure phase is initiated by activating the chemical reaction of the resin, better known as polymerisation or cross-linking, which results in curing of the resin matrix. This cure initiation is generally accomplished by the addition of heat to speed up the reaction and subsequently decrease cure- and process time. Lastly, after sufficient hardening or whenever the part is completely cured, demoulding and final processing can take place.

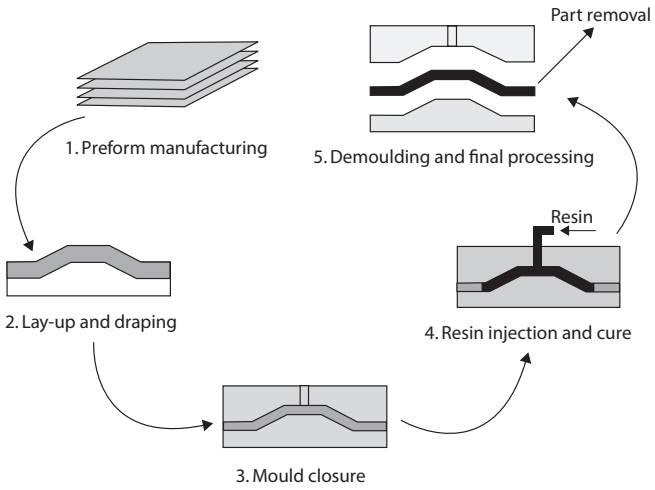

Figure 2.2: Schematic diagram of the process steps in RTM. Obtained and modified from [3]

2.1.1. Vacuum-Assisted RTM

Vacuum-Assisted RTM (VARTM) is a variation of RTM, for which the production steps are very similar to RTM. The main distinction is that the resin is drawn into the sealed cavity through the use of a vacuum instead of being injected under pressure. In addition, only a single-sided mould combined with either a flexible or rigid cover is used instead of two matching rigid moulds. This process can be explained using figure 2.3, which illustrates the 'vacuum bagged' type of VARTM. Within this schematic it can be observed that a single-sided mould is used where, after placement of the preforms, the cavity is sealed using a flexible bag [3, 5]. By drawing a vacuum to remove the air from this sealed cavity, compacting of the preform on the mould surface can be achieved [3, 5]. Subsequently, the resin matrix material is drawn via on or multiple inlet ports into the mould from a reservoir which is at atmospheric pressure [3]. Whenever the preform is completely impregnated by the resin material, the cure phase can be initiated and similar steps as for RTM can be followed.

One advantage of VARTM are the lower non-recurring costs compared to RTM, because only a single-sided mould is required which is generally cheaper as process loads are lower [6]. Another advantage is the capability to manufacture larger components, as the size of the metal RTM moulds is often limited by the span limitations of the milling machines [3, 6]. The major disadvantage of VARTM is the limited injection pressure of one atmosphere at maximum, which results in injection speeds being relatively slow [3, 5]. Secondly, the process can result in an increased non-uniformity of the FVF along the part

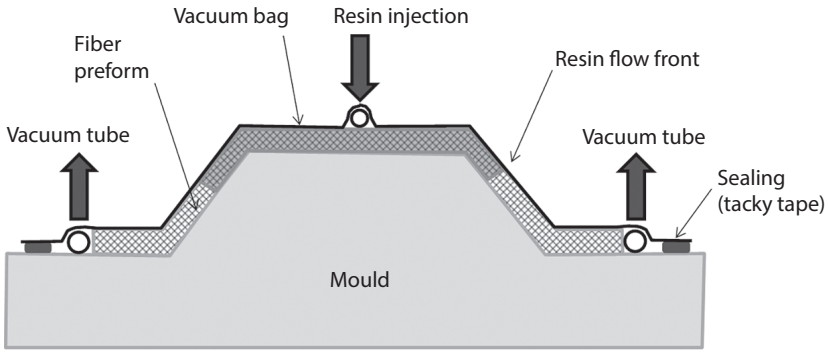

Figure 2.3: Schematic diagram of VARTM setup. Obtained and modified from [3]

as the resin flow can change the compaction along the part [3, 5]. As the FVF is a parameter on which almost all effective thermal- and mechanical properties of the laminate are dependent on, it is desired to maintain it as constant as possible to prevent substitutional differences in the part behaviour [6].

2.1.2. The Cure Phase

After the complete impregnation of the dry-fibre preform and filling of the mould cavity by the liquid matrix material, curing is required to end up with a solid composite part. The cure phase is the most critical process step in term of the development of residual stress within composite laminates [7]. For TS matrix materials, this cure phase implies the chemical polymerisation reaction by which the liquid matrix material transforms irreversibly into a solid. The different molecular stages of this polymerisation reaction are schematically illustrated by figure 2.4.

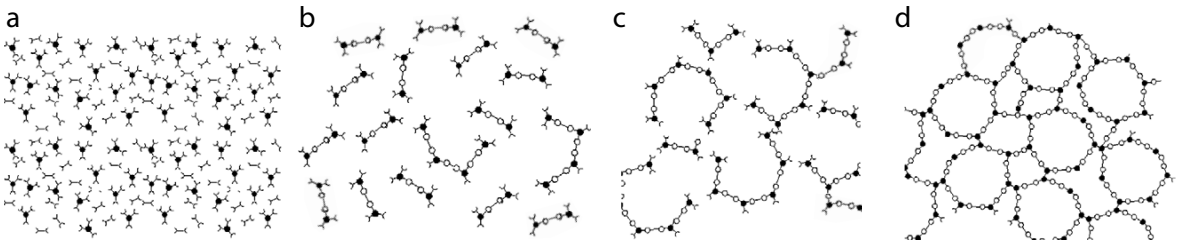

Figure 2.4: Schematic of cure progression due to polymerisation reaction: a) monomers and co-reactants prior to cure phase, b) cure phase started: molecular structure increases by linear growth and branching, c) gelation stage: continuous network but incompletely cross-linked structure, d) fully cured network structure. Obtained and modified from [8, 9]

The aforementioned low viscosity of TS materials is the result of the low molecular weight of the polymer molecules, known as monomers [10]. During a cure phase, the chemical polymerisation reaction between these monomers takes place, which is based on the chain lengthening of these monomers into a single cross-linked molecular structure [10]. The created cross-links are the chemical bonds between the monomers, which together form a network structure. Up to certain Degree of Cure (DOC), the individual monomers are bonded to form a continuous molecular network where limited molecular movement is still possible [8]. Around this point, which can be defined as the gelation point, the viscosity of the matrix material increases rapidly due to the reduced mobility of the polymer chains. This results in a transition of the material from viscous to rubbery where its response becomes highly viscoelastic [8, 10–12]. This transition from viscous to rubbery can be observed within figure 2.5. By continuing the polymerisation reaction, the DOC increases to its maximum, the material becomes fully cured and its response changes to elastic [8]. The cross-links which form the network structure cannot be removed unless the material is exposed to temperatures which result in total material degradation [10].

TS materials are based on two different components, in general classified as the resin and the co-reactant or hardener [13]. To initiate the chemical cross-linking reaction, the addition of external heat

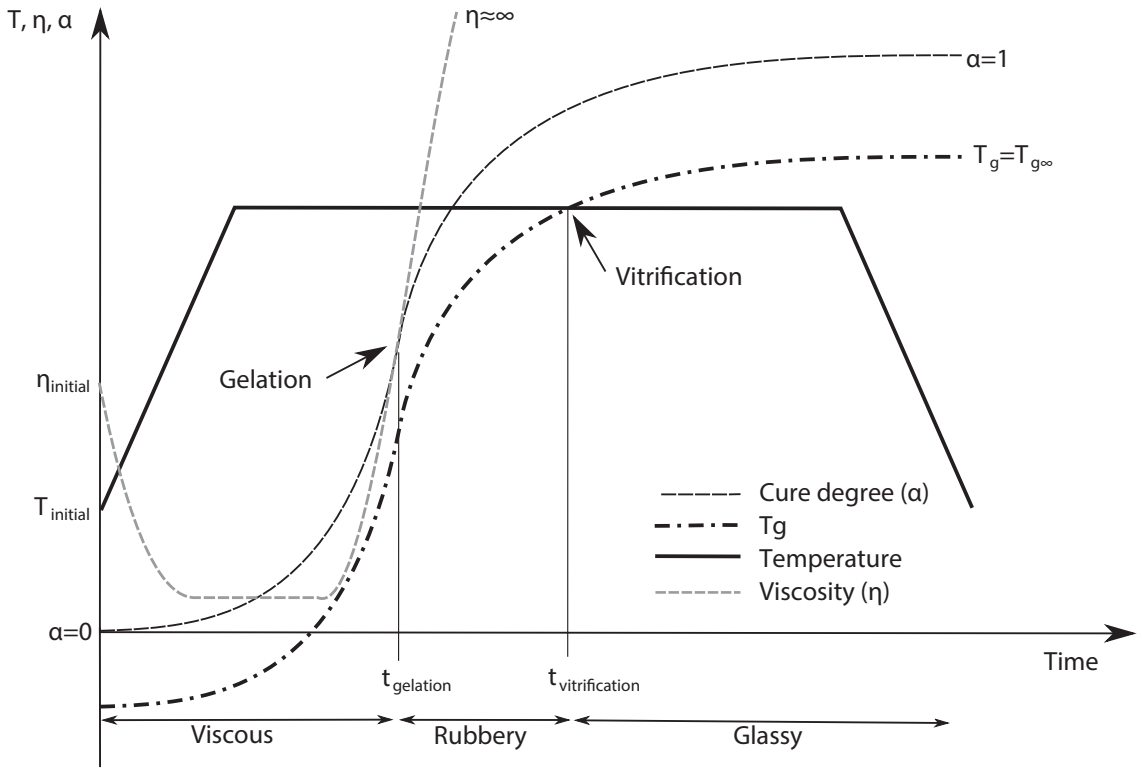

Figure 2.5: Schematic of cure cycle illustrating the evolution of DOC, Glass transition temperature and resin viscosity as function of temperature and time. Obtained from [6]

prescribed by a (temperature) cure cycle is implemented [5, 13]. A typical cure cycle consists in its most basic form out of a heating stage, dwell stage and cool down stage, as illustrated by figure 2.5 [3]. Whenever larger amounts of mass are being cured, care should be taken as this chemical reaction is exothermic for a variety of TS resins and can therefore result in significant heat development [14]. Whenever thick composite laminates are being cured without taking this into account, temperature overshoot can result in the decrease of laminate quality by material degradation or significant increase of cure-induced residual stress due to the larger temperature gradients resulting in an uneven cure [15].

2.2. Cure Phase Analysis

Within this section, each cure-related phenomena which is required for understanding the physics and to develop the thermal-chemical and thermal-mechanical part of the cure model is described. As predominantly TS epoxy resin is being used within RTM, the scope of this literature review focusses on these types of resin systems from upon this section [3, 5].

2.2.1. Heat Transfer Equation

Temperature evolutions during the cure phase can be described using heat transfer equations. Two different heat transfer models can be proposed, both using multiple thermophysical properties: the two-phase model and the local equilibrium model [16–18]. In the two-phase model both the resin, i.e. the fluid, and fibre reinforcement material, i.e. the solid, are described with different temperature-averaging energy equations for a flow through porous media by equation 2.1 and equation 2.2, respectively. This model is used whenever rapid changes in temperature and chemical reactions occur, e.g. non-isothermal resin injections [16, 18].

The local equilibrium model, denoted equation 2.3, describes slow or even stagnant resin flow and ignores heat transfer between the resin and fibre material, which justifies the assumption of local thermal equilibrium at the moment the fibres are covered with resin. This equation is based on the volume fraction and the average temperature of a control volume containing both the resin and fibres [3]. Both models can be described by the Fourier's law of heat conduction and convection:

Two-phase model:

Heat transfer equation for matrix material:

$$\phi\rho_r c_{p,r}\frac{\partial T_r}{\partial t} + \underline{\rho_r c_{p,r}(\vec{V}\cdot\nabla T_r)} = \phi\nabla\cdot K_r\nabla T_r + \phi h_{rf}(T_r - T_f) + \phi\dot{Q} \tag{2.1}$$

Heat transfer equation for fibre material:

$$(1-\phi)\rho_f c_{p,f}\frac{\partial T_f}{\partial t} = (1-\phi)\nabla\cdot K_f\nabla T_f + \phi h_{rf}(T_f - T_r) \tag{2.2}$$

Local equilibrium model:

$$\rho_c c_{p,c}\frac{\partial T}{\partial t} + \underline{\rho_r c_{p,r}(\vec{V}\cdot\nabla T)} = \phi\nabla\cdot K_c\nabla T_r + \phi\dot{Q} \tag{2.3}$$

where ρ, c_p and K are the density, specific heat capacity and thermal conductivity (tensor), respectively. The heat transfer coefficient, represented by h_{rf}, couples both equations of the two-phase model. ϕ, T and $\vec{V}$ are the porosity, the absolute temperature and velocity field , where subscripts r, f and c denote the resin, fibre and composite, respectively. The porosity can be defined as the free volume within the mould cavity between the fibrous preform, i.e. the porous media, that can be filled by the resin [19, 20]. The heat source $\dot{Q}$, which represents the instantaneous heat generated by the polymerization reaction of the resin, is proportional to the reaction rate and can be described by [20]:

$$\dot{Q} = \rho_r H_T\frac{d\alpha}{dt} \tag{2.4}$$

where H_T is the total reaction heat and $d\alpha/dt$ is the reaction rate, i.e. the cure rate, of the resin system [16, 18].

As mentioned, the porosity ϕ represents the free volume within the mould cavity. By this definition it implies an ideal void-free volume after resin injection, which in practice never occurs [18, 21]. Voids will always be initially present or can be formed during the injection and cure phase, resulting in lower resin volume fractions. This leads to the substitution of the porosity parameter by the resin volume fraction v_r within equation 2.4, where $v_r < \phi$ [18]. Both models are based on the assumptions of incompressible fluid, constant thermo-physical properties and Newtonian flow [16, 18]. In addition, whenever stagnant resin flow is assumed and heat transfer by convection is neglected, the underlined convection terms within equations 2.1 and 2.3 can be discarded [16, 18].

Based on above simplifications, the expression for the thermochemical energy equation for heat transfer described by the local equilibrium model can be rewritten to:

$$\rho_c c_{p,c}\frac{\partial T}{\partial t} = \nabla(K\nabla T) + \rho_r v_r H_T\frac{d\alpha}{dt} \tag{2.5}$$

2.2.2. Cure Kinetics

The cure kinetics of resin systems, i.e. the changes of chemical compositions over time by the influence of temperature, can be modelled by using mechanistic- or phenomenological (semi-empirical) models [22, 23]. Mechanistic models are based on the balance of the chemical species involved within the cure reaction, which is in many cases difficult to model without analysing the chemical reactions in detail [7, 11, 24]. Phenomenological models however, are used to fit experimental data with sufficient accuracy and are therefore preferred for predicting the cure kinetics within the cure phase [23, 24]. As result, in the following section the scope is limited to these phenomenological cure models only.

An overview of the most commonly used cure kinetic models that are proposed to date are presented within table 2.1. All models are based on the nth order kinetic model, the autocatalytic kinetic model, or a combination of both [25]. The nth order , defined by equation 2.6, uses a single reaction rate constant K_i to describe the cure reaction and assumes no autocatalytic phenomena [26]. Whenever autocatalytic effects are exhibited, i.e. the maximum reaction rate $(d\alpha/dt)$ is observed at t > 0, autocatalytic reaction models are required [26, 27]. These models describe the cure reaction by one or multiple reaction rate

Table 2.1: Cure Kinetic models

Kinetic model	Equation		
n[th] order equation reaction model [29]	$\frac{d\alpha}{dt} = K_1(1-\alpha)^n$		(2.6)
Lee, Loos, and Springer [30]	$\frac{d\alpha}{dt} = (K_1 + K_2\alpha)(1-\alpha)(B-\alpha)$	$\alpha \leq 0.3$	(2.7)
	$\frac{d\alpha}{dt} = K_3(1-\alpha)$	$\alpha > 0.3$	(2.8)
White and Hahn [22]	$\frac{d\alpha}{dt} = K_1\alpha^m(1-\alpha)^n$		(2.9)
Kamal-Sourour [31, 32]	$\frac{d\alpha}{dt} = (K_1 + K_2\alpha^m)(1-\alpha)^n$		(2.10)
Cole with Diffusion [32, 33]	$\frac{d\alpha}{dt} = \frac{1}{1+e^{C(\alpha-(\alpha_{c0}+\alpha_{CT}T)}}K_1\alpha^m(1-\alpha)^n$		(2.11)
Kamal-Sourour with Diffusion [31, 32]	$\frac{d\alpha}{dt} = \frac{1}{1+e^{C(\alpha-(\alpha_{c0}+\alpha_{CT}T)}}(K_1 + K_2\alpha^m)(1-\alpha)^n$		(2.12)
Arrhenius-dependent rate constant	$K_i = A_i e^{\frac{-\Delta E_i}{RT}}$		(2.13)

constants, as described by equation 2.9 and equations 2.7, 2.8 and 2.10, respectively, and results in an improved estimation accuracy for more complex resin systems [18, 27, 28].

Whenever the cure reaction cannot be described by the aforementioned kinetic models, the general complex model can be used, which is reported elsewhere [18]. For most TS epoxy resin systems, the cure reaction modelling is best approximated by the combined reaction model defined by equation 2.10 [26].

Within the cure kinetic models from table 2.1, the DOC is denoted by α, and n and m are the reaction orders [18, 24]. The reaction rate constant, denoted by K_i, is based on the Arrhenius-type rate constant which is described by equation 2.13, where A_i, E_i and R are the pre-exponential constant, the activation energy for the chemical reaction and the universal gas constant, respectively [34, 35].

Diffusion

An additional characteristic of the kinetic modelling of resin systems includes diffusion effects [23]. The chemical reaction of resin systems are based on combinations of both molecular collision and diffusion of chemical species. During the initial stage of the cure phase, the diffusion of the chemical species is fast which results in the reaction being chemically-controlled [23, 26]. Whenever the cure progresses, the cross-link network density increases which results in reduction of the resin free-volume and subsequently a rapidly decrease in mobility of the chemical species [8]. During this stage, which is known as vitrifying, the resin changes from rubbery to glassy state [11, 18]. From the start of this stage the reaction becomes diffusion-controlled, which must be incorporated within the aforementioned kinetic models [23, 36].

To include this diffusion process, a modification on the reaction rate constant can be proposed as follows [23, 26, 32]:

$$\frac{1}{K_e} = \frac{1}{K_c} + \frac{1}{K_d} \tag{2.14}$$

where K_e is the effective reaction rate constant and K_c is the aforementioned Arrhenius-dependent rate constant, defined using equation 2.13 [26]. The diffusion process is included via K_d, which can be defined by two different methods. The first method is based on expressing the diffusion-controlled

stage by a dependency on the Glass transition temperature (Tg). Whenever the Tg surpasses the temperature of the resin, it vitrifies and turns into a glassy state [10]. This point, known as the vitrification point, is illustrated within the previously reported schematic cure cycle within figure 2.5. As result of this vitrification, the mobility of the polymer chains reduces significantly, the reaction rate decreases and subsequently the final DOC cannot reach the theoretical unity value [10, 18]. The definition of this diffusion rate constant can be defined by [26, 37, 38]:

$$K_d = A_d e^{\left(-\frac{E_d}{RT}\right)} e^{\left(-\frac{b}{f}\right)} \tag{2.15}$$

where A_d and b are constants, and E_d represents the activation energy of the diffusion process. In addition, T is the cure temperature and f the equilibrium fractional free volume, which is defined by [26, 38]:

$$f = 0.00048(T - T_g) + 0.025 \tag{2.16}$$

The Tg within this definition, can be modelled using the DiBenedetto equation, which can be described as follows [26, 35, 38, 39]:

$$T_g = T_{g0} + \frac{(T_{g\infty} - T_g)\lambda\alpha}{1 - (1 - \lambda)\alpha} \tag{2.17}$$

where T_{g0} and $T_{g\infty}$ are the glass transition temperature of the initial solution of monomers (unreacted resin system) and fully cured resin system, respectively [38, 39]. The parameter λ is a material property between 0 and 1 which represents the ratio of heat capacities of the glassy and rubbery state of the initial and fully cured resin system [18, 26, 39]. With the DiBenedetto relation, the evolution of the glass transition temperature can be determined at any stage of the cure [11].

According to Cole and others [8, 28, 40], this first method requires complex constants which are often difficult to obtain. Therefore, a second method for the diffusion-controlled rate constant can be proposed, which is defined by [8, 40]:

$$K_d = K_c e^{-C(\alpha - \alpha_c)} \tag{2.18}$$

where K_c is the original Arrhenius-dependent rate constant and α_c is the critical DOC from which the cure reaction changes to diffusion-controlled [32, 40]. This α_c is dependent on the cure temperature via:

$$\alpha_c = \alpha_{c0} + \alpha_T T \tag{2.19}$$

where α_{c0} is the critical DOC at T = 0 kelvins and α_T is the parameter accounting for the dependency of this value to the cure temperature [8]. When combining equation 2.18 with equation 2.14 and implementing the effective reaction rate into the aforementioned cure kinetic models from table 2.1, the kinetic models including diffusion effects can be defined by equations 2.11 and 2.12.

2.2.3. Thermophysical Properties

As mentioned in section 2.2.1, additional thermophysical properties of the composite laminate are required for the heat transfer equation. These properties are the density ρ_c, specific heat capacity $c_{p,c}$ and thermal conductivity K_c of the composite laminate, and are dependent on the temperature and DOC [18]. In addition, the thermal expansion and chemical shrinkage are described within this section as well.

Specific Heat Capacity

The specific heat capacity can be defined as the amount of heat that is required to raise the temperature of 1 gram material by 1 kelvin. For the laminate, this property can be determined by using the heat capacity values of the resin system and fibre material and homogenizing it using the rule of mixture [18, 41]. This property can directly be implemented within the simplified local equilibrium model (equation 2.5) and is defined by:

$$c_{p,c} = w_f c_{p,f} + (1 - w_f) c_{p,r} \tag{2.20}$$

where w_f is the fractional weight of the fibre, and $c_{p,f}$ and $c_{p,r}$ are the specific heat capacity of the fibre material and resin system, respectively [41]. The specific heat capacity of the fibre material depends on the temperature, while for the resin system it depends on both the temperature and DOC. These heat capacities can be defined by:

$$c_{p,f} = A_{f_{c_p}} T + B_{f_{c_p}} \tag{2.21}$$

$$c_{p,r} = A_{r_{c_p}} T + B_{r_{c_p}} + \frac{\Delta_{rc_p}}{1 + e^{C_{rc_p}(T - T_g - \sigma)}} \tag{2.22}$$

where $A_{f_{c_p}}$, $B_{f_{c_p}}$, $A_{r_{c_p}}$ and $B_{r_{c_p}}$ are parameters for the linear dependency of the heat capacity with temperature, where subscripts f and r denote the fibre- and resin material, respectively. In addition, Δ_{rc_p}, C_{rc_p} and s are the strength, width and temperature shift of the specific heat capacity around the Tg [41, 42].

Thermal Conductivity

The thermal conductivity of composite laminates can be defined in multiple orthogonal directions. This is because the thermal conductivity is highly influenced by the fibre orientation as result of the significantly higher conductivity of fibre materials compared to resin material [23]. The thermal conductivity of a laminate can be determined by first defining it for a single ply, using the thermal conductivities of both the fibre and resin material. Different models have been proposed and are generally based on the anisotropic carbon fibre (or isotropic glass fibre), and isotropic resin properties together with the volume fractions of these constituents [18, 23, 43]. The scope of the following thermal conductivity equations is limited to NCF plies only as these are used as first approximation for cure modelling [23, 44].

The thermal conductivity in the direction along the fibre, i.e. the longitudinal thermal conductivity, denoted with K_l, can be defined by:

$$K_l = v_f K_{lf} + (1 - v_f) K_r \tag{2.23}$$

where v_f, K_{lf} and K_r are the FVF, and the thermal conductivities of the fibre material in longitudinal direction and the resin system, respectively [23, 41, 42, 45]. The thermal conductivity in the direction perpendicular to the fibre, i.e. the transverse thermal conductivity, denoted with K_t, can be defined by:

$$K_t = v_f K_r \left(\frac{K_{tf}}{K_r} - 1\right) + K_r \left(\frac{1}{2} - \frac{K_{tf}}{2K_r}\right) + K_r \left(\frac{K_{tf}}{2K_r} - 1\right) \sqrt{v_f^2 - v_f + \frac{\left(\frac{K_{tf}}{K_r} + 1\right)^2}{\left(\frac{2K_{tf}}{K_r} - 2\right)^2}} \tag{2.24}$$

where K_{tf} is the thermal conductivity of the fibre in transverse direction [23, 42]. The relation of K_{lf}, K_{tf} and K_r with the temperature and DOC can be defined by:

$$K_{lf} = A_{lf} T + B_{lf} \tag{2.25}$$

$$K_{tf} = B_{tf} \tag{2.26}$$

$$K_r = a_{Kr} T \alpha^2 - b_{Kr} T \alpha - c_{Kr} T - d_{Kr} \alpha^2 + e_{Kr} \alpha + f_{Kr} \tag{2.27}$$

where A_{lf} and B_{lf} are the longitudinal-, and B_{tf} the transverse temperature dependency parameter for the thermal conductivity of the fibre material [42]. The coefficients $a_{Kr} - f_{Kr}$ are used to include the relation between the thermal conductivity of the resin with the temperature and DOC [23, 42].

Thermal Expansion

The Coefficient of Thermal Expansion (CTE) of the composite can be expressed in the longitudinal and transverse direction as well. Using micromechanics laws, the following expressions for the longitudinal CTE, a_l, and transverse CTE, a_t, can be defined by [46, 47]:

$$a_l = \frac{\left(1 - v_f\right) E_r a_r + v_f E_{lf} a_{lf}}{\left(1 - v_f\right) E_r + v_f E_{lf}} \tag{2.28}$$

$$a_t = (1 - v_f)\, a_r + v_f a_{tf} + (1 - v_f)\, a_r \nu_r + \nu_{12f} a_{lf} v_f - \nu_{12} a_l \tag{2.29}$$

where a_r, a_{lf} and a_{tf} are the CTE of the resin, and fibre in longitudinal and transverse direction, respectively. E_r and E_{lf} are the resin modulus and fibre modulus in longitudinal direction, where the former is defined within section 2.2.4 and the latter is constant. In addition, ν_r, ν_{12f} and ν_{12} are the Poisson's ratio of the resin, the Poisson's ratio of the fibre in longitudinal direction and the in-plane Poisson's ratio of the composite [48]. The CTE of the resin can be expressed as follows [49]:

$$a_r = a_{rub} + \frac{(a_{glass} - a_{rub})}{1 + e^{C_m(T - T_g - \sigma_m)}} \tag{2.30}$$

where a_{rub} and a_{glass} are the CTE values of the linear regions in the rubbery and glassy state of the resin, respectively, and C_m and σ_m are constants describing the transition around the Tg [48].

Resin Shrinkage

As result of the polymerisation reaction of the resin, shrinkage effects can be observed during the curing phase. The volumetric shrinkage of the resin can be fitted using a linear or bilinear DOC dependent function, where for the latter the breakpoint of the curve is around the gel point [50, 51]. For a linear dependent function, the following equation can be proposed:

$$\gamma_r = \gamma_\alpha \alpha \tag{2.31}$$

where γ_r and γ_α represent the instantaneous and maximum linear shrinkage of the resin, respectively [48]. Subsequently, the resin shrinkage can be defined in longitudinal and transverse direction as follows:

$$\gamma_l = \frac{(1 - v_f) E_r \gamma_r}{(1 - v_f) E_r + v_f E_{lf}} \tag{2.32}$$

$$\gamma_t = (1 - v_f)\gamma_r + (1 - v_f)\gamma_r \nu_r - \nu_{12f} \gamma_l \tag{2.33}$$

2.2.4. Thermomechanical Properties

Similar to the thermophysical properties, the modulus and Poisson's ratio of the resin are influenced by the temperature and DOC, for which the latter is included via the Tg [48, 49]. Using the following two expressions, the modulus and Poisson's ratio of the resin can be defined by:

$$E_r = E_{rub} + \frac{(E_{glass} + E_{glassT} \times T - E_{rub})}{1 + e^{C_m(T - T_g - \sigma_m)}} \tag{2.34}$$

$$\nu_r = \nu_{rub} + \frac{(\nu_{glass} - \nu_{rub})}{1 + e^{C_m(T - T_g - \sigma_m)}} \tag{2.35}$$

where E_{glass} represent the modulus at glassy state, E_{glassT} includes the linear temperature dependence of the modulus at glassy state and E_{rub} represent the modulus in rubbery state [48]. ν_{rub} and ν_{glass} are the resin Poisson's ratios at rubbery and glassy state, respectively, while C_m and σ_m are equal as the aforementioned definitions from the resin CTE (equation 2.30).

2.3. Cure-Induced Residual Stress

Within this section, the mechanisms causing cure-induced residual stress within composite laminates are evaluated. Since most of these are present regardless the thickness of the laminate, these fundamental mechanisms are discussed first within section 2.3.1. Subsequently, the additional influences introduced by an increased laminate thickness are described within section 2.3.2.

2.3.1. Fundamental Mechanisms of Residual Stress

Residual stress and related distortions are caused by fundamental mechanisms originating from either the (changing) properties of the composite constituents, the interactions between the laminate and tooling or a combination of both. In general, the onset of residual stress development can be marked by the gelation of the resin material [7, 52]. Prior to this stage, the resin is able to relax all induced stresses,

resulting in a stress-free state. However, as result of gelation the resin modulus develops significantly and subsequently residual stress can be induced, regardless of the origin of this development [7]. Within the following sections, each origin and how these contribute to the residual stress development throughout the cure phase are discussed.

Thermal Expansion Differences

Significant differences in CTE are present between the fibre and matrix material. The residual stress development and interactions resulting from these differences can be identified on different scale levels within the composite laminate, with each having their own effect on the residual stress.

On micro-scale level, i.e. fibre-matrix interaction level, residual stress arises due to the difference in CTE between the fibre filament and surrounding matrix material. The fibre material can be either isotropic, for glass fibres, or anisotropic, for carbon fibres. For glass fibre material generally the CTE is positive, while for carbon fibre material this property is slightly negative in longitudinal direction, but positive and larger in magnitude in radial direction [48, 53, 54]. The resin material is isotropic with a significantly larger CTE compared to glass or carbon fibres, usually between one- and two order of magnitude larger for the resin in glassy or liquid stage, respectively [54].

From the elevated cure temperatures to the end of the cool down stage, and by assuming sufficient bonding between the resin and fibre filaments from the gelation point up to the maximum DOC, residual stress can arise because of the relatively higher thermal contraction of the resin compared to the fibre material. These residual stress interactions are visualized by figure 2.6, where the grey arrows visualising the shrinkage direction of the resin material. Although this type of residual stress at fibre-matrix interaction level is present within all cure-processed composite laminates, this stress alone is not significant enough to induce laminate distortions directly [55].

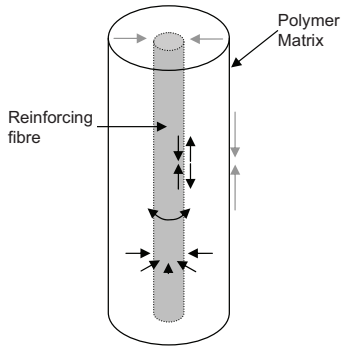

Figure 2.6: Micro-scale residual stress interaction caused by matrix shrinkage, with →← and ←→ indicating compressive and tensile residual stress, respectively. Obtained from [56]

On ply-scale level, residual stress arises due to CTE differences in multiple in-plane orientations and the difference between the in-plane and through-thickness direction. In-plane residual stress within plies develops by the anisotropic behaviour caused by the larger CTE in the transverse direction of the fibres, which is matrix dominated, compared to the direction along the fibres, which is fibre dominated [53]. Redistribution of these stresses upon demoulding can result in curvature and warpage within unsymmetrical and unbalanced laminates, which is illustrated by figure 2.7. And even if laminates are symmetric and balanced, geometrical curvature and residual stress redistribution can result in bending and subsequently a shift of the neutral axis [53, 55].

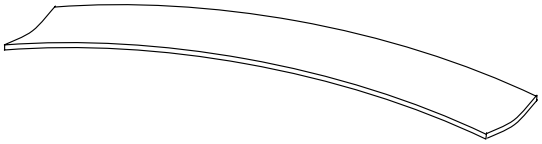

Figure 2.7: Curvature and warpage in unsymmetric cross-ply laminate. Obtained from [53]

Due to the difference in CTE between the in-plane and through-thickness direction, a change in curvature for curved laminates can be related to residual stress development and redistribution as well. This phenomena, known as the spring-in effect, is depicted by figure 2.8 [53, 55, 57].

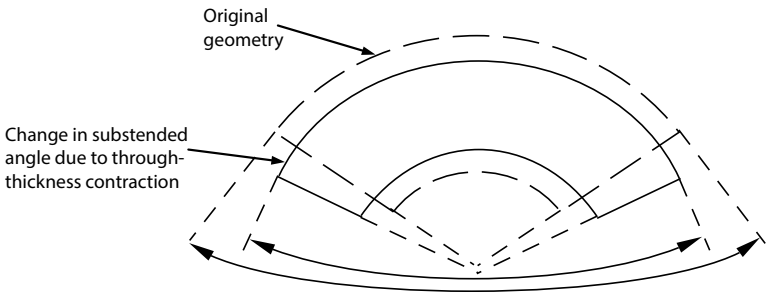

Figure 2.8: Laminate spring-in mechanism. Obtained and modified from [53]

Volumetric Chemical Shrinkage

The second origin of residual stress can be related to the chemical shrinkage of the resin material. This volumetric shrinkage, which is caused by the polymerisation reaction that reduces the resin free-volume, is generally difficult to quantify and predict because it develops simultaneously with the thermal expansion during heating stages [50]. This can be observed within figure 2.9, where both the temperature- and DOC evolution of a generic cure cycle is illustrated together with the stages of expansion, shrinkage and contraction. As can be seen within this graph, from upon the dwell stage the temperature remains constant and the volume reduction is therefore only dependent on chemical shrinkage. As generally the DOC reaches its maximum value at the end of the dwell stage, during cool down the volume reduction is only dependent on thermal contraction.

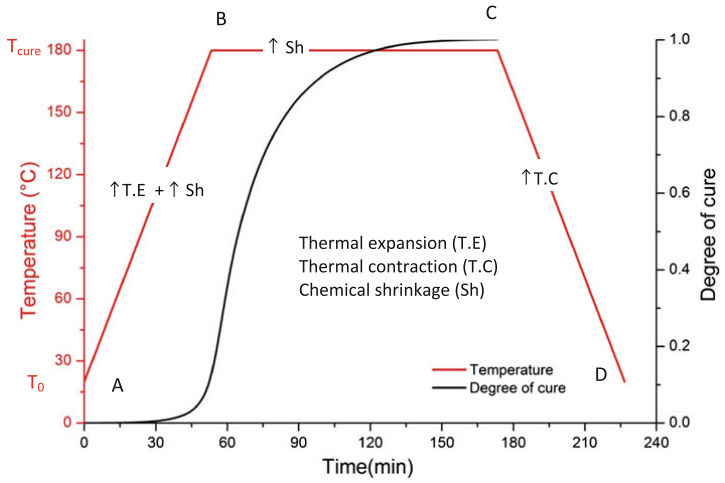

Figure 2.9: Cure cycle of an epoxy resin. Obtained and modified from [50]

The overall volume change throughout the cure phase can be illustrated by plotting it against the temperature evolution, depicted by figure 2.10. During the heating- and cool down stage, illustrated by a-b and c-d, respectively, the temperature changes between the ambient temperature T_0 to the curing temperature T_c and back, which results in the volume change mainly driven by thermal expansion and contraction [9]. Note that when chemical shrinkage becomes significant during the heating stage, it influences the linear volume increase by deflecting downwards prior to reaching point b. During the dwell stage, illustrated by b-c, the effective volume reduction resulting from the chemical shrinkage progresses linearly when assuming that no exothermic phenomena are present during the dwell stage. Note that the slope from stage c-d is less significant compared to the slope from stage a-b, which can be explained by the CTE of the resin material being lower in glassy state than in the liquid/rubbery state [9, 20, 58].

As explained by Kravchenko et al. [52] and Adli and Jansen [59], from the gelation point up to the maximum DOC, both the bonding between the fibres and matrix, and the resin modulus become significant [7]. This results in residual stress generation induced by the interaction between the volumetric shrinkage of the resin at fibre-matrix interaction level, and between the fibre- and matrix dominated directions at ply-level. Although the observed volume shrinkage between point a and d in figure 2.10 appears low, the effective volumetric chemical shrinkage during stage b-c can be up to 7% for an epoxy resin and can increase the effects introduced by residual stress generation caused by the CTE differences at ply-level significantly [51, 53]. Since gelation occurs somewhere between point b-c, the residual stress build-up induced by chemical shrinkage and thermal contraction can be increased to significant levels [52].

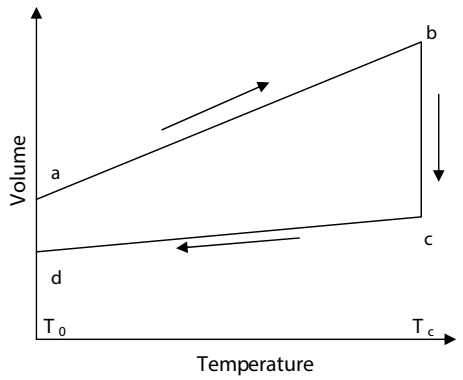

Figure 2.10: Schematic of volume change of epoxy resin during cure cycle. Obtained from [9]

Tooling Interaction

Residual stress development from tooling interaction is based on the mismatch of CTE between the composite part and the tooling material [53, 55]. The CTE of tooling material is often higher compared to the overall CTE of the composite. During the cure phase, both the part and tooling surfaces expand due to the elevated curing temperatures, which results in an additional elongation of the surface plies that are in contact with the tooling surface. Subsequently, gradients of in-plane shear stress through-thickness can be induced, which are being constrained within the laminate whenever the DOC passes the gelation point and vitrifies. Upon cooling, this results in the development of residual stress. This interaction effect is illustrated by figure 2.11 for a cure process with a single-sided mould configuration.

The surface plies of the part closed to the tooling surface are loaded with the highest amount of residual stress, which decays through-thickness. After removal of the tooling, redistribution of this residual stress results in bending curvature, warpage or even fibre waviness [57]. Parametric study from Twigg et al. [60] revealed that with increasing thickness the maximum curvature and warpage of the part decreases since it becomes more difficult to redistribute the residual stress by the increased stiffness of the laminate.

The CTE mismatch between the part and tooling can result in complications upon demoulding such as locking of the part within the mould [53, 55, 61]. With an outside mould, prior to the cool down stage of the cure, both the part and tooling are still expanded at the elevated cure temperature. Throughout the cool down stage, the thermal contraction of the tooling is higher compared to the composite. This phenomena can result in locking of the part and subsequently compressive stress build-up in the outer surface layers of the composite part which can result in laminate damage [57]. Whenever an inside mould is used, during the heating stage tensile stress within the laminate reinforcement can be developed due to the higher CTE and therefore larger expansion of the mould. From the gelation point up to maximum DOC, these tensile stresses remain present within laminate. Upon cooling of both the mould and composite part, these stresses can influence the overall residual stress development and can cause delamination and geometry distortions as well [62].

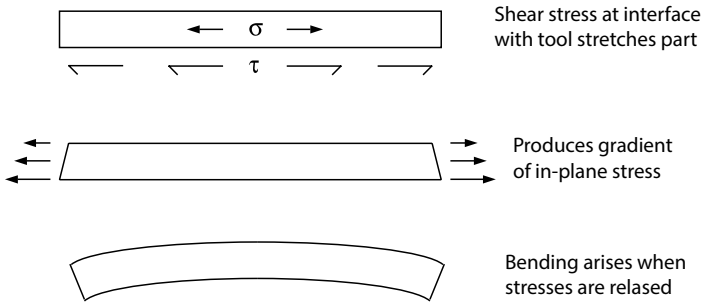

Figure 2.11: Laminate warpage due to interaction at tool interface. Obtained from [53]

2.3.2. Thick Composite Laminates

According to Struzziero and Skordos [63], in the aerospace industry distinction between thin- and thick composite laminates can be defined whenever the thickness exceeds 10 mm [63]. When curing thick composite laminates, additional challenges regarding residual stress can be identified. The first challenge is the aforementioned increased stiffness of thick laminates. During the cure phase and after demoulding, the residual stress within thin laminates can be redistributed and averaged out over the laminate by deformations. This effect is more difficult within thick laminates, since the increased stiffness makes this stress redistribution more difficult. As result, matrix cracking and ply delamination can occur whenever the residual stress levels within the laminate increase [64].

Another challenge introduced by the large thickness is the possibility of thermal gradients through-thickness during the cure phase. As generally the polymerisation reaction is exothermic, through-thickness temperature gradients can occur when curing thick TS composites. These can influence the reaction rate at different locations through-thickness. As result, uncured or partly cured regions can be constrained by fully cured regions, which results in additional residual stress build-up through-thickness [9, 58, 62]. An example is depicted by figure 2.12, where the outer-plies are cured prior to the plies at the centre region of the laminate. This phenomena, known as outside-in curing, results in a parabolic through-thickness stress distribution [57].

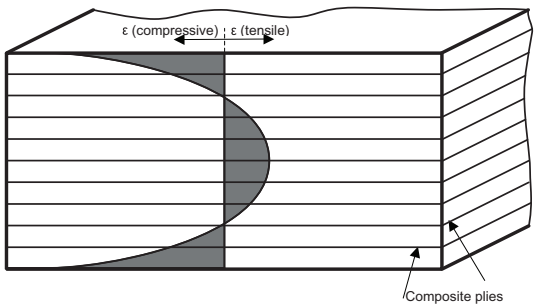

Figure 2.12: Through-thickness residual stress distribution [57]

2.3.3. Implementation of Fundamental Mechanisms

The fundamental mechanisms of residual stress described within section 2.3.1 can be determined using the strains induced by these mechanisms. In total three strain types can be identified; mechanical strains, thermal strains and chemical strains. These strains are included in the following total strain definition [65]:

$$\varepsilon_{ij} = \varepsilon_{ij}^{M} + \varepsilon_{ij}^{T} + \varepsilon_{ij}^{Sh} \tag{2.36}$$

where ε is used to define the strain with subscripts i,j = 1, 2, 3 for the orthogonal directions and superscripts M, T and Sh denote the mechanical-, thermal- and chemical origin of the strain, respectively. The relation between the thermal strain and chemical strain with the CTE and linear shrinkage of the resin can be defined using:

$$\varepsilon_{ij}^{T} = \Delta T \{a_{ij}\} \tag{2.37}$$

$$\varepsilon_{ij}^{Sh} = \Delta \alpha \{\gamma_{ij}\} \tag{2.38}$$

in which ΔT and $\Delta \alpha$ are the change in temperature and DOC, respectively. The vector notations $\{a_{ij}\}$ and $\{\gamma_{ij}\}$ include the CTE and linear shrinkage coefficients of the transversely isotropic ply and isotropic resin regions.

By redefining the mechanical strain from equation 2.36 to stress, the following equation can be defined:

$$\varepsilon_{ij} = [S]\,\sigma_{ij} + \varepsilon_{ij}^{T} + \varepsilon_{ij}^{Sh} \tag{2.39}$$

which subsequently can be rewritten as:

$$\sigma_{ij} = [C]\left[\varepsilon_{ij} - \left(\varepsilon_{ij}^{T} + \varepsilon_{ij}^{Sh}\right)\right] \tag{2.40}$$

in which $[S]$ and $[C]$ are the compliance and stiffness matrix, respectively, and σ_{ij} is the vector notation of the final resulting stress components.

2.4. Cure Simulations

Prior to the use of cure simulations, research regarding the cure process was only possible using empirical methods [19]. These were costly, time consuming and were only limited to small specimens. As result, the obtained data was generally not representative for entire laminates which made it difficult to determine the appropriate cure cycle and its influence on the residual stress development [19]. To overcome these challenges, cure simulation models based on the cure kinetics from section 2.2 were developed, which numerically could predict the temperature and DOC evolution for laminates with different geometries and material properties [19]. From upon this section, distinction is made between thermal-chemical models and thermal-mechanical models. The first only predicts the influence of thermochemical material properties and its relation with the evolution of temperature and DOC. The latter includes this as well but in addition the development of mechanical properties, e.g. the resin modulus, and its relation with temperature and DOC [66].

2.4.1. Thermal-Chemical Modelling

Loos and Springer [19] investigated continuous fibre-reinforced TS materials using a model which included thermal-, chemical- and physical processes and their response on the cure phase [19]. The results obtained using this numerical model were verified by experimental data from which it was concluded that these type of models can adequately predict both temperature and DOC distribution during the cure phase [19]. In addition, a parametric study revealed that using this model, the most suitable cure cycle could be determined in terms of an uniformly cured composite within the shortest amount of time. Similar research was conducted by Bogetti and Gillespie [67] and Teplinsky and Gutman [68], where the cure phase of thick TS composites was investigated using a two-dimensional anisotropic cure model [67]. Different arbitrary cross-sections, such as angle bend and ply drop-off laminates, were analysed to investigate the influence of the cure phase and tooling on the gradients in temperature and DOC. It was found that these gradients are not only strongly dependent on the cure kinetics, thermal anisotropy and temperature cycle, but these can be influenced by thickness variations as well [67, 68]. An example is depicted by figure 2.13, where a ”hot” region can be observed in which the temperature rises significantly above the laminate surroundings as result of the exotherm [67]. In addition, as effect of larger temperature gradients, the thick section is only cured to a DOC of 0.12 while the thin section is already fully cured at this stage of the cure phase [67]. This outside-in curing, discussed within section 2.3.2, can potentially induce severe stress levels and deformations during the cure phase [67].

Park and Lee [69] developed a Finite Element Analysis (FEA) model for two-dimensional CFRP cure simulations in which the thermal conductivity of the mould was taken into account [69]. According to the results, including the mould within the simulation is worth the additional computational effort as the influence of the variation in thermal conduction of tooling cannot be underestimated [69]. Whenever these moulds are relatively thick, these must be added to the simulation to include heat sink effects due

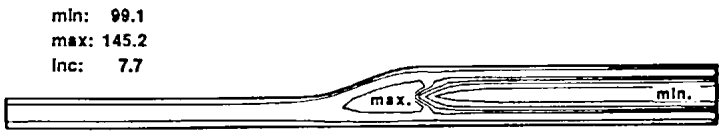

(a) Temperature Contour at Exotherm

(b) Degree of Cure Contour at Exotherm

Figure 2.13: Two-dimensional anisotropic cure simulation, contour plots with a) temperature gradients trough-thickness and b) DOC evolution. Obtained and modified from [67]

to the thermal conductivity between the laminate and the mould. Using modern FEA software, these mould interactions can be included by different thermal properties at the boundary of the laminate, which can reduce the computational work to simulate an entire moulding geometry. Overall, the model from Park and Lee [69] successfully simulated both temperature and DOC gradients within thick composite structures which can lead to residual stress development [69]. As result of the translation from the 3D problem to the two-dimensional model, recommendations were made that a three-dimensional model is required to diminish additional errors introduced by the 2D simplifications.

Epoxy resin samples were analysed by Zhang et al. [70] to assess the influence of heating rates on the temperature DOC and gradients of thick epoxy resin samples using the commercial FEA software ABAQUS combined with multiple FORTRAN subroutines. Results obtained using a three-dimensional simulation model, which were validated by literature and experiments, revealed that not only cure cycle temperatures but heating rates can affect the non-uniform curing and temperature distribution of the resin as well. By emphasizing non-uniform curing inside the part, an increase in warpage and residual stress development was observed [70].

2.4.2. Thermal-Mechanical Modelling

Next to cure phase studies using thermal-chemical models, the prediction of mechanical property evolutions as function of temperature and DOC, and the influence of these on the residual stress development became more accurate as these models further improved. Bogetti and Gillespie [58] implemented a kinetic-viscoelastic model of the resin using an α-mixing rule, which explicitly expresses the instantaneous resin modulus in terms of the DOC [22, 58]. By including thermal expansion and chemical shrinkage as main contributors of stress development throughout the cure phase, it was found that transverse stress distributions changed as result of the increased laminate thickness. This effect is depicted by figures 2.14 and 2.15, where it can be observed that for an increasing thickness, the transverse stress distribution changes from an internal compressive stress- to an internal tensile stress region. This change is the effect of the transition from inside-out curing to outside-in curing, which is caused by the delay in heating and the exothermic reaction of the internal region within thick laminates [58].

Instead of defining the development of the resin modulus by a relation with the DOC only, Khoun and Hubert [54] used an elastic modulus model as function of the difference between the Tg and the cure temperature [54]. By coupling a heat transfer- and stress analysis using a three-dimensional FEA model based on ABAQUS/COMPRO, the dimensional stability and tool-part interactions of composite structures as result of the RTM process were investigated [54, 64]. Bellini and Sorrentino [66] used an equal material model for the resin modulus evolution as reported by Ersoy et al. [71], and implemented this using the PAM-RTM and PAM-Distortion software for the thermal-chemical and thermal-mechanical part of the FEA model, respectively [66]. This research focussed on spring-in effects caused by cure-induced residual stress as result of the RTM process. According to simulation results, it was concluded that the stacking sequence of laminates is the most influencing parameter regarding spring-in defor-

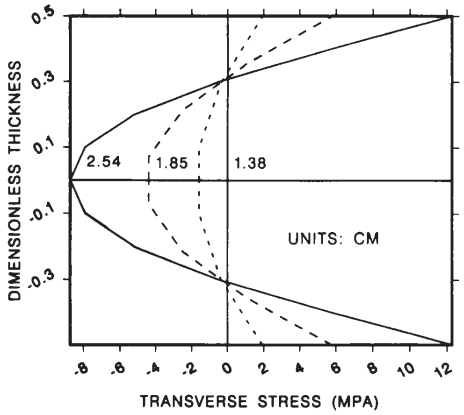

Figure 2.14: Transverse residual stress distribution (thickness ≤ 2.54 cm). Obtained from [58]

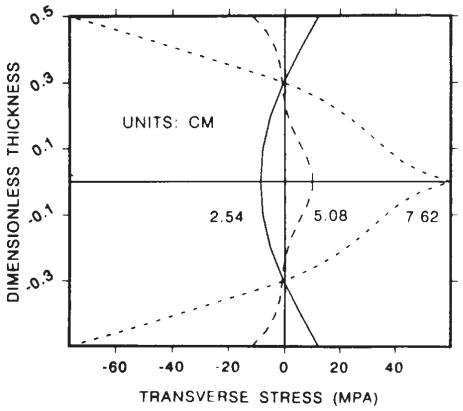

Figure 2.15: Transverse residual stress distribution (thickness ≥ 2.54 cm). Obatined from [58]

mation while both the effect of the laminate thickness and mould radius was minimal [66].

Research conducted by Struzziero and Teuwen [46] investigated the residual stress generation within ultra-thick curved laminates [46]. For the cure phase simulation, the resin modulus was implemented using a relation with a step transition around the Tg with an additional exponential dependency on the DOC after transition [46, 49]. As result of the cure phase of VARTM, residual stress develops and subsequently results in the spring-in effect after demoulding. Using a coupled thermal-mechanical analysis model and by initially applying the Manufacturer Recommended Cure Cycle (MRCC), the resulting spring-in displacement, cure-induced residual stress and the exothermic temperature profile were obtained. It was found that the MRCC led to spring-in effects together with significant residual levels [46]. Both the displacement and residual stress contour plots are illustrated in figure 2.16 and figure 2.17, respectively.

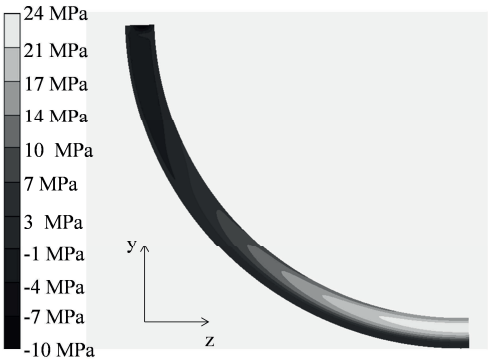

Figure 2.16: Contour plot of spring-in displacement in z-direction, wind turbine blade root insert. Obtained from [46]

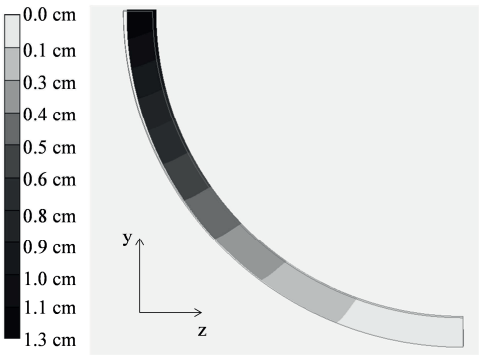

Figure 2.17: Contour plot of residual stress distribution, wind turbine blade root insert (σ_{zz}). Obtained from [46]

2.5. Ply Drop-off Regions

As described in section 1.1, the necessity of ply drop-off regions originates from the required thickness transition between sections of composite laminates. Since this tapering in thickness can result in both material- and weight reductions, this laminate feature is implemented in many different structural components [72]. An example of a laminate in which multiple ply drop-off regions are implemented is illustrated by figure 2.18. As shown, by terminating multiple plies the laminate thickness is reduced between the thick- and thin section.

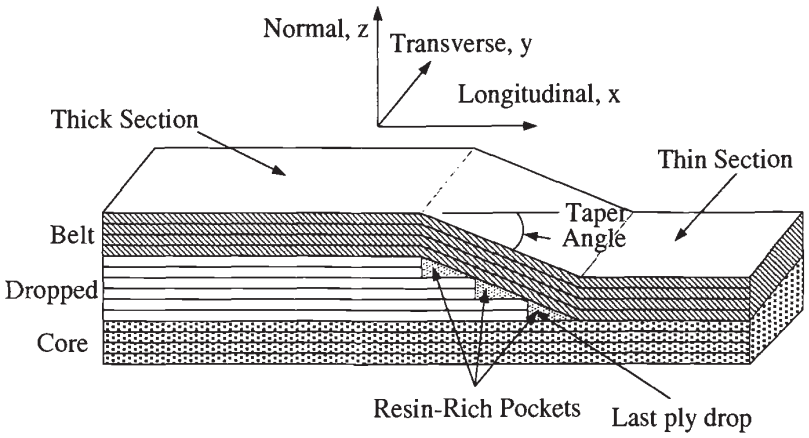

Figure 2.18: Schematic of ply drop-off regions. Obtained and modified from [73]

Multiple characteristics of ply drop-off regions can be identified using figure 2.18. Each ply termination results in a resin pocket, which are generally simplified by a right-angled triangle. The geometry of this resin pocket can be described by the aspect ratio a/b, which is the ratio between the height and length of the resin pocket resulting from the ply termination [74]. The plies below and above the ply drop-off region can be identified as the core plies and belt plies, respectively [72, 73]. Whenever multiple ply drop-offs are implemented to achieve a specific thickness reduction, the stagger distance is introduced as parameter which defines the distance between two successive ply drop-offs [75].

2.5.1. Design Guidelines

For the implementation of ply drop-off regions within laminates, multiple design guidelines can be followed. These guidelines are generally deduced from studies involving experimental testing, strength and buckling optimizations, and fracture mechanics [76, 77]. Overall, these guidelines are based on the following rules of thumb [76]:

- The number of terminated plies, i.e. dropped thickness, at any given drop-off region should be kept to a minimum.
- Termination of plies should be achieved in decreasing order of stiffness in longitudinal direction. This involves that the stiffest plies (0° orientation) should be terminated at the thick section and least stiffest plies (90° orientation) should be terminated at the thin section. This ensures the most gradual transition of load transfer and reduction in stress concentrations.
- The stagger distance between multiple drop-off regions should be at least three times the ply drop-off thickness. Whenever 45° plies are being dropped, this distance should be eight times the thickness.
- While plies are being terminated, the laminate should be kept both symmetric and balanced in order to prevent coupling effects.

Despite that these guidelines can potentially reduce stress concentrations introduced by ply drop-off regions, some of these can be conflicting in practice. For example, maintaining both a symmetric and balanced laminate layup can be challenging whenever drop-offs are arranged according to their stiffness [76]. In addition, the guideline regarding the minimal stagger distance may not be feasible whenever the available length of the required thickness reduction is limited [77].

2.5.2. Ply Drop-off Research To Date

Ply drop-off regions within composites can be identified as discontinuities within laminates and therefore stress risers [72, 77]. The effects of ply drop-offs on the stress-strain behaviour and different fracture modes within carbon/epoxy laminates were investigated by Cannon [74]. Drop-off laminates were tested under uniaxial tensile loading, where it was observed that predominately the order in which different drop-offs are implemented only has influence on the deviation in results between drop-off laminates and uniform-thickness laminates [74]. The failure stress and failure mode of the ply drop-

off laminate were equal and similar to the uniform-thickness laminate having the same layup as the dropped section within the drop-off laminate [74].

Mangalgiri and Vijayaraju [78] investigated the stress levels near ply drop-off regions to determine the potential delamination locations and energy release rates based on fracture mechanics [78]. By implementing a prescribed strain at one end of the laminate using FEA modelling, the influence of the stagger distance between two successive drop-offs and the effect of the layup sequence were investigated [78]. Results showed that strain-energy release rates increased significantly whenever two plies were dropped together compared to implementing significant stagger distance between these. An additional result, which conflicted with the current design rules from section 2.5.1, showed that dropping a 90° ply between two 0° plies results in higher possibility of delamination arresting at this dropped ply [78].

In contrast to most studies, Vizzini [73] included realistic ply drop-off geometries such as ill-formed resin pockets, unsymmetric and misplaced drop-off locations, varying ply thickness and voids to investigate the influence of these on the interlaminar stress levels [73]. Using FEA modelling and by implementing an uniaxial displacement to induce in-plane stress, it was found that ill-formed resin pockets increase the effective aspect ratio and subsequently increase interlaminar stress levels which can initiate delamination [73]. An example of an ill-formed resin pocket is illustrated by figure 2.19. Also, the presence of voids increases these stress levels at the ply drop-off significantly. Because delamination was assumed to occur as result of failure of the resin (layer), the Von Mises failure criterion was analysed [73]. Vizzini [73] concluded that although neglecting realistic drop-off geometries for strength predictions may introduce additional errors, qualitative results from idealized geometries can still be valid provided that these geometries are uniform and the overall relations between the observed trends are unaffected by geometry differences [73].

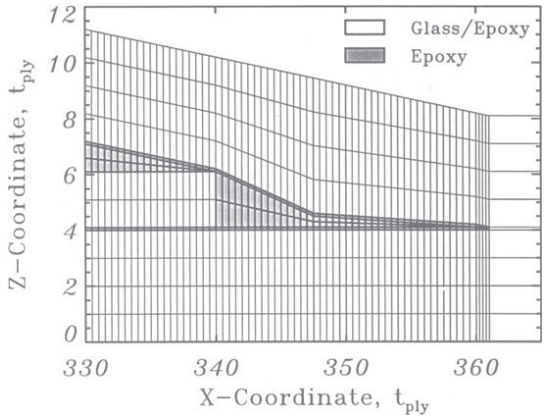

Figure 2.19: Mesh structure for an ill-formed resin pocket. Obtained from [73]

A new type of ply drop-off element has been developed by Varughese and Mukherjee [72] and implemented within a FEA model based on the global-local approach [72, 75]. Using this model, the magnitude and distribution of major interlaminar stress levels at ply drop-off regions of both symmetric and unsymmetric laminates were investigated [75]. These stresses, i.e. out-of-plane stresses, are predominant in the vicinity of the drop-off and may cause ply delamination upon loading [72, 75]. From the analysis in which laminates were loaded in longitudinal direction at the thin section, results showed that highly uniform out-of-plane stress levels are observable near the drop-off while at locations away from the drop-off these become negligible [75]. The same model was later used to analyse parameters such as the number of dropped plies, stagger distance and ply orientation, and the influence on the maximum out-of-plane stress levels [77]. The aforementioned drop-off design guidelines were mainly based on the observations resulting from this research study [77]. Similar global-local approach was used by Gan et al. [76], who investigated the prediction of the delamination onset from individual ply drop-offs using a FEA model in which the laminate was submitted to uniaxial tensile loading [76].

One of the few research studies involving cure-induced stress instead of implementing (uniaxial) loadings was conducted by Mulle et al. [79]. This research focussed on the through-thickness gradients

of autoclave cure-induced in-plane residual stress within carbon/epoxy beam specimens containing design singularities such as ply drop-offs [79]. Strain values obtained by experimental testing using fibre Bragg gratings, which were compared with 3D FEA simulation results, suggested that the possible influence of different through-thickness thermal properties and tooling-laminate interactions on the behaviour of the material are significant and cannot be ignored [79].

Despite that these research studies provide useful knowledge regarding implementing ply drop-off regions within composite laminates, almost all studies are based on (uniaxial) tensile loadings. Research concerning the influence of ply drop-off regions on cure-induced residual stress is practically absent, which leads the following: Concluding from the discussed studies above, it can be stated that the available data regarding ply drop-off regions within (thick) composite laminates and their influence on cure-induced residual stress and related distortions is limited. Based on this research gap, the proposed research questions from section 1.2 were formulated.

3

Coupled Thermal-Mechanical Model

This chapter is dedicated to the modelling and verification of the thermal-mechanical cure model which is required to analyse the cure-induced residual stress around ply drop-off regions. Within section 3.1, a brief introduction of the cure model is given. In section 3.2 the method by which the cure model is implemented in the Abaqus software and the required assumptions, elements and user subroutines are given. The coupling of these subroutines is described in section 3.3. Within section 3.4, all material models required for the cure model are described with corresponding parameters. In section 3.5 the sensitivity analysis concerning the numerical parameters controlling the time incrementation of the cure simulation is presented, followed by the verification of the thermal-mechanical model in section 3.6. This chapter ends with the conclusions in section 3.7.

3.1. Motivation

To understand the influence of ply drop-off regions on the cure-induced residual stress, a comprehensive method is required to analyse the residual stress evolution as result of the cure phase of the RTM process. Using a coupled thermal-mechanical analysis model within the FEA software Abaqus, cure simulations can be conducted to analyse these stress evolutions. Multiple material properties describing the thermal-, chemical- and mechanical behaviour of the laminate are implemented within the model to predict the residual stress. The following phenomena and properties are included: cure kinetics, orthotropic thermal expansion and chemical shrinkage, and orthotropic thermal- and mechanical material properties. The thermal- and mechanical material properties are changing continuously during the cure phase. By predicting these changing properties throughout the cure phase, their influence together with laminate- and cure cycle parameters on the residual stress evolution around ply drop-off regions can be investigated.

The fundamentals of the thermal-mechanical model are based on studies investigating the generation of residual stress during the cure phase of the VARTM process [48, 80]. These studies focused on accurately characterizing the viscous-elastic material properties of the resin system and implemented these in a coupled thermal-mechanical model within the FEA software Marc.Mentat to predict the final residual stress and warpage of asymmetric laminates [48]. Using multi-objective optimization methods, both the final warpage and process time were reduced by means of intensionally generating cure-induced residual stress [48].

The materials used within this study are based on a non-crimp E-glass fibre fabric, and the two component Airstone™ 780E epoxy resin and 785H hardener system that is often used in the wind turbine blade manufacturing industry [48]. As the material characterization data regarding the thermal-chemical and thermal-mechanical properties is available in an extensive range, which is required for accurate cure-induced residual stress predictions, these are being used for the current study [46]. Although these material properties differ from the materials used by FLG, it is expected that the influence of ply drop-off regions on the cure-induced residual stress can be observed nevertheless and therefore common effects and conclusions can be deduced. Details of the material characterization data and its validation are out of the scope of this research study and are described in [48, 80].

For each cure simulation within this research study, the MRCC is implemented unless specified otherwise. This cure cycle is selected as baseline because even though it is the standard cure cycle provided by the manufacturer, it is often not optimal in terms of cure-induced residual stress [63]. By using this cure cycle as base line, the evolution of cure-induced residual stress around the drop-off regions can be assessed.

Regarding the output of the thermal-mechanical model, different data can be extracted such as the changing material properties, the cure-induced displacements or the residual stress. Literature review showed that the residual stress generated during the cure cycle can have considerable effects, especially for thick composite parts which are often too rigid to redistribute these stresses by distortions, resulting in possible delamination and matrix failure [81]. Since a ply drop-off can be identified as discontinuity within laminates, this introduces additional stress concentrations around the drop-off region. These can lead to process-failures through delamination or failure of the resin pocket [72]. The main contributing stress component of these composite failures around the pocket is the out-of-plane direct tensile stress, which is acting normal the plane of the plies (through-thickness direction), in the direction outwards from the resin pocket [72]. Using the ply drop-off model created for this research study, this out-of-plane tensile stress is selected as main output quantity to analyse the influence of residual stress around drop-off regions. Since the resin pocket can be the origin of process-failure as well, the Von Mises equivalent stress within this pocket region is included as output quantity from the upon the sections that thick laminates are considered.

3.2. FEA Model

The thermal-mechanical model is built using different Abaqus utilities, by which the thermal-mechanical coupling, material property models and manufacturing process conditions are all implemented. In the following sections the model implementation and assumptions, type of elements and required user subroutines are described.

3.2.1. Model Implementation in Abaqus

For predicting the residual stress evolution, it is important to build the model as such that the material properties are dependent on both the temperature and the DOC evolution. Within Abaqus, this can be achieved using a transient coupled temperature-displacement analysis, in which the thermal- and mechanical solution parts can be coupled either in a sequential order or simultaneously [82]. For the former type, first a heat transfer analysis is executed whereafter a stress analysis is performed. By mapping the thermal loadings from the thermal analysis into the stress analysis, an one-way coupling is achieved in which the stress evolution depends on the temperature fields but not vice versa.

Different from the sequential type of analysis, is the fully coupled type in which both the thermal and mechanical solutions are obtained simultaneously throughout the analysis [82]. This type is often used for processes where both the thermal and mechanical effects strongly influence each other. In essence, this two-way coupling is not required for the current model, but because the DOC data resulting from the thermal solution part is directly required by the mechanical solution part, the fully coupled option will be used for the current model. By this, a single complementary analysis model can be used which is more convenient compared to running two sequential analysis models. Although a fully coupled analysis model can potentially increase computational effort, for the current thermal-mechanical model it is expected this will have no significant influence.

3.2.2. Model Definition and Assumptions

The verification model and ply drop-off model are both built up as three-dimensional models, where fixed-displacement boundary conditions in the in-plane directions are applied to simulate an internal strip of the laminate. As result, the problem reduces to 2.5D in which laminate edge effects at the drop-off regions can be ignored while out-of-plane and internal in-plane effects can still be considered. The implemented boundary conditions for each model are described in the corresponding sections.

As result of the boundary conditions, initial conditions and simplifications that are introduced by using the FEA software, multiple assumptions arise which can be described as follows:

- It is assumed that within the model, all elements have an equal ambient temperature and stress-free state as initial condition.

- It is assumed that compaction of the laminate has reached its maximum prior to the start of the cure simulation. The effects of compaction can result in additional stress built-up which may influence the final residual stress [83]. Because of the assumed initial stress-free condition at the start of the cure simulation, the influence of compaction is ignored which can result in the final residual stress levels being underestimated.
- Since the cure simulation initiates at the start of the cure phase, resin flow as result of the injection phase is neglected and assumed to be stagnated.
- The laminate is assumed to be a non-porous medium without voids.
- Because the aforementioned VARTM process includes one mould side and one vacuum film side that follows equal temperature profiles, time dependent temperature boundary conditions are implemented. It is assumed that the input of the reference temperature of both surfaces is uniform over the entire surface. Note that this assumption only applies for the model input as exothermic reactions can still increase temperatures locally.

3.2.3. Elements

Both the verification model and ply drop-off model are built using three-dimensional 8-node brick elements (Abaqus element type: C3D8T) where both thermal and displacement degree of freedoms are included at each node [82].

3.2.4. User Subroutines

Implementation of the material models is carried out using multiple user subroutines that are provided within Abaqus. All subroutines required are included together in a single separated file and written in FORTRAN. During the analysis, the solver uses this subroutine file to calculate the evolving material properties for each increment and step, dependent on time, temperature and other variables. Since only minor changes are implemented between the subroutine files of the verification model and ply drop-off model, only the ply drop-off model file is included in appendix A. Together with this code, the Solution Dependent State Variables (SDVs) that are shared between the subroutines and can be used for post-processing purposes are included in appendix B. The following subroutines are included in each model [84]:

- **SDVINI** is used for implementing initial values for SDVs which cannot be set within the Abaqus initial conditions module.
- **UMAT**[1] is used to implement material models that are not available within the Abaqus material library when when specific behaviour of material properties dependent on changing SDVs are required. In this subroutine, the cure kinetics, evolution of mechanical properties and the governing equations for the thermal-mechanical analysis are implemented.
- **UMATHT**[1] describes the evolving thermal properties and thermal analysis of the model.
- **DISP** is used to define the time dependent temperature boundary condition of the mould surface during the cure cycle of the process. Within this subroutine the heating rate, dwell temperature, dwell time and cooling rate all can be specified individually.
- **FILM** can be compared with the DISP subroutine and is used to describe both the sink temperature and convection coefficient of the natural air boundary condition of the vacuum film surface. The sink temperature of this subroutine follows the same cure cycle as implemented in the FILM subroutine.

3.3. Thermal-Mechanical Coupling

The thermal-mechanical coupling of the model describes which phenomena and material properties are related to each other and in which sequence these are calculated. This sequence is essential because thermal effects at a particular time increment can have significant influence on the mechanical behaviour of the material for the next time increment. For instance with increasing cure rate, the heat of reaction increases proportionally as well (equation 2.4). As result, thermal energy and temperature

[1] For the ply drop-off model, distinction is made between the composite ply and neat resin material regions (i.e. resin pocket) by using two sub-models within one subroutine

increases which can cause additional strain by thermal expansion. It is therefore important to take into account these temperature changes before continuing with the next increment where these temperatures are used for the calculation of the effective strains on which the stress components are based. Because the mechanical properties depend on both the DOC and temperature, these must be updated for each time increment to end up with accurate residual stress predictions. Using figure 3.1, the required sub-parts and subroutines within the coupled thermal-mechanical analysis can be defined as follows;

At the start of each time increment, the values of the temperature, DOC, and stress and strain components are called for each element. These values are obtained either from the previous time increment or from the predefined initial values of the analysis step described in the Abaqus initial conditions module or SDVINI subroutine. The temperature and the DOC values are used by the cure kinetics module within the UMAT subroutine to determine the cure rate, the instantaneous Tg and to predict the DOC value at the end of the current time increment.

The DOC value from the start of the time increment is used within the same UMAT subroutine to define mechanical properties such as the elastic modulus, shear modulus and Poisson's ratio. These are determined to set up the Jacobian matrix of the constitutive material models [84]. This matrix, known as the stiffness matrix, is used for calculating the incremental stress using the incremental strains. These strains can have one of the following three origins; mechanical strain, thermal strain and chemical strain, which were described in section 2.3.3.

After completion of the UMAT subroutine, the UMATHT subroutine is called within the same time increment for each element. Within this subroutine the Tg and DOC values at the start of the current time increment are both used within the thermal properties module for determining changes in the thermal conductivity and specific heat of the materials. The cure rate from the UMAT subroutine is used for determining the exothermic heat generation within the thermal analysis module in which, together with the updated thermal conductivity and specific heat value, the thermal energy is updated for the next time increment.

At the end of each time increment, the updated strain, stress, DOC and thermal energy values are stored and transferred to the next time increment, where the complete sequence is repeated again up to the point where the maximum step time is reached. Note that the updated thermal energy is only required for Abaqus to determine the change in temperature for each element and not used for any material property calculations.

3.3.1. Automatic Time Incrementation

As can be seen in figure 3.1, at the end of every time increment two different options are possible for the FEA solver. If a solution for that increment cannot be found, the solver abandons the time increment and another attempt is executed with a smaller time increment size. This decrease in increment size is known as a cutback [85]. These cutbacks are repeated until a converged solution for that time increment is found or the minimum allowable time increment size is subceeded, whereafter the analysis is aborted.

If the solution of a single time increment converges, the output data of that time increment is stored in the database. Whenever for a predetermined number of consecutive time increments the solution is found easily, i.e. 3 times in a row without any cutbacks (by Abaqus default), the size of subsequent time increments can be increased up to a preset maximum allowed increment size [85].

3.4. Definition of Material Models

During the cure phase, multiple material properties change as result of the evolution in temperature and DOC. For the implementation of the materials within the model, the following material models are required.

3.4.1. Cure Kinetics

The cure kinetics model determines the cure rate, $d\alpha/dt$. For the materials used within this study, this model is based on an autocatalytic cure model with diffusion factor, developed by Hubert et al. [36],

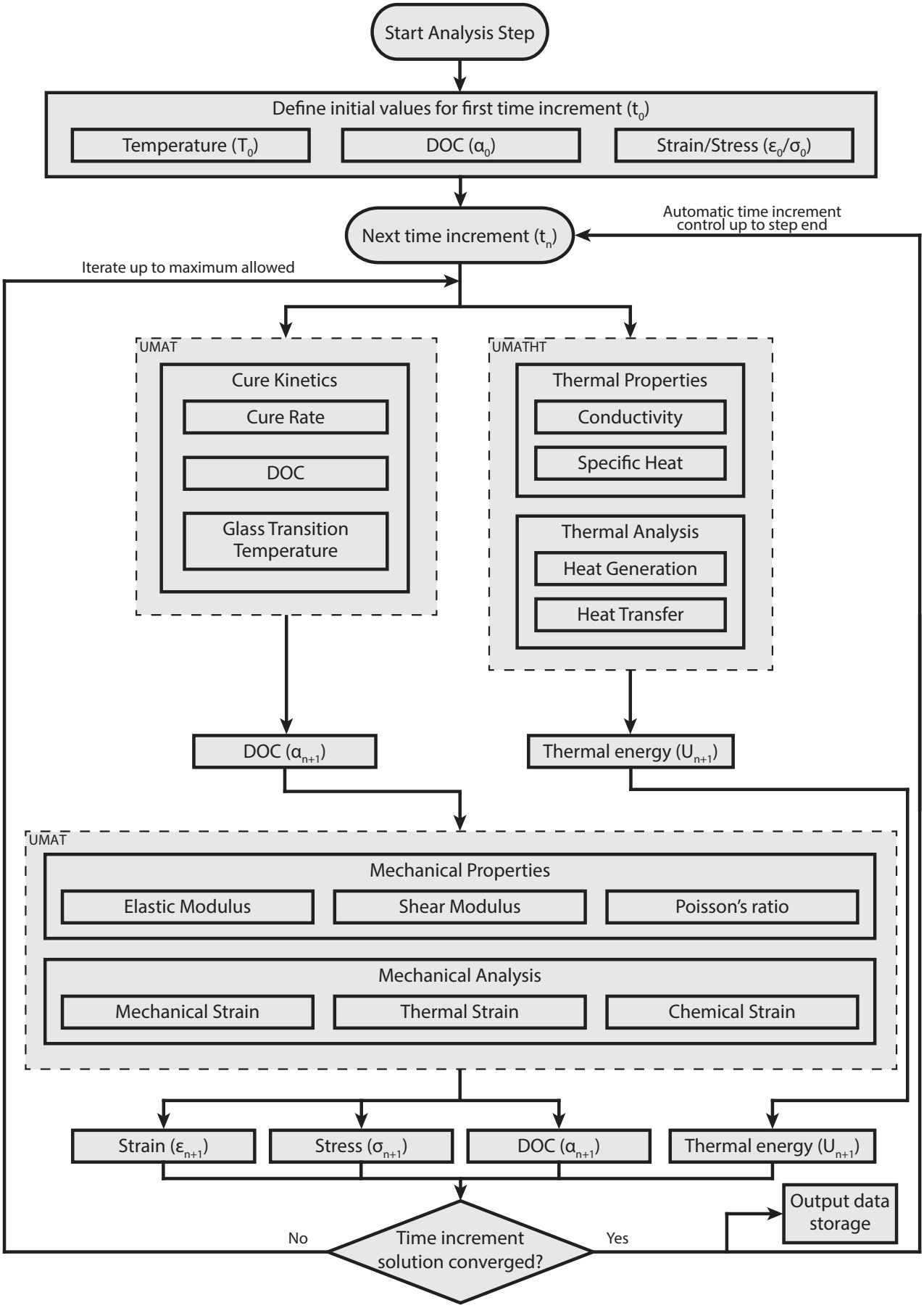

Figure 3.1: Visualization of thermal-mechanical coupled model

and is a combination of equation 2.11 and equation 2.13:

$$\frac{d\alpha}{dt} = \frac{Ae^{\left(\frac{-E}{RT}\right)}}{1 + e^{C(\alpha - \alpha_c - \alpha_T T)}}(1-\alpha)^n \alpha^m \tag{3.1}$$

Using the cure rate, the exothermic heat of reaction of the resin can be calculated. This heat of reaction, denoted by the heat source term $\dot{Q}$ within the heat transfer equation defined in section 2.2.1, can be rewritten from equation 2.4 [80]:

$$\dot{Q} = (1 - v_f)\rho_r H_T \frac{d\alpha}{dt} \tag{3.2}$$

For the prediction of the DOC, the following Finite Difference Method (FDM) is used to estimate the new DOC for the next time increment:

$$\alpha_{n+1} = \alpha_n + \Delta t \cdot \left.\frac{d\alpha}{dt}\right|_n \tag{3.3}$$

where the subscripts n and $n+1$ represent the current and next increment, respectively, and Δt is the time increment size. This FDM is generally used in FEA software via an one-step finite difference scheme [86]. Alternatively this FDM can be implemented by the use of a multi-step difference scheme. This multi-step type requires multiple DOC values from previous time increments combined with coefficients to get better approximations of the true solution for the next time increment. In general the multi-step scheme can result in more accurate predictions, but when the time increment size is kept relatively small (in the order of hundreds of seconds), differences in DOC prediction between the two schemes are insignificant [86]. In addition, for the multi-step difference scheme the subroutines become more complex due to the multiple required DOC values from the previous time increments that must be stored for each increment. Considering this, for the current model the one-step difference scheme is implemented, for which the maximum time increment size will be determined based on its influence on the convergence and error of the model output.

The evolution of the instantaneous Tg and its relationship with the DOC is implemented using the DiBenedetto equation defined by equation 2.17 [35, 39]. The fitting parameters for equations 2.17 and 3.1 to 3.3 are given in table 3.1.

Table 3.1: Parameters for the cure kinetics and glass transition temperature of Airstone™ 780E/785H epoxy resin [80]

Parameters	Values	Units
A	681,085	s^{-1}
E	59,291	$J\,mol^{-1}$
n	1.67	
m	0.12	
C	47.7	
α_c	0.77	
α_T	0.0016	$°C^{-1}$
H_T	434,000	$J\,kg^{-1}$
T_{g0}	-55	°C
$T_{g\infty}$	89	°C
λ	0.476	

3.4.2. Thermal Properties

Different thermal properties are included within the model. For the epoxy resin, these properties are changing during the cure phase with dependence on temperature, Tg and DOC, while the properties of the glass fibre material can be either temperature dependent or constant.

Specific Heat Capacity

The specific heat capacity of the composite, fibre material and resin follows from equations 2.20 to 2.22 respectively [41, 48]. The corresponding constants, which can be determined by experimental fitting using data obtained by Differential Scanning Calorimetry (DSC), are given in table 3.2 [80].

Thermal Conductivity
The thermal conductivity of the composite laminate is orthotropic and can be calculated using the contributions from both the glass fibre and epoxy resin. Since the material orientation of the laminate is based on NCF plies, the material orientation of a single ply can be simplified to transversely isotropic, which results in only two directional components that can be calculated; the longitudinal component K_l and the transverse component K_t [80]. These components can be defined by equations 2.23 and 2.24, respectively [87]. In addition, K_r represents the isotropic thermal conductivity of the resin, which is described by the polynomial function from equation 2.27 and for which the coefficients are obtained from literature [41, 42, 80]. All parameters required for the thermal conductivity models aforementioned are included in table 3.2 [42].

Table 3.2: Parameters for the thermal properties of E-glass fibres and Airstone™ 780E/785H epoxy resin [80]

Parameters	Values	Units
$A_{f_{c_p}}$	0.0014	$J\,g^{-1}\,°C^{-2}$
$B_{f_{c_p}}$	0.841	$J\,g^{-1}\,°C^{-1}$
$A_{r_{c_p}}$	0.0025	$J\,g^{-1}\,°C^{-2}$
$B_{r_{c_p}}$	1.80	$J\,g^{-1}\,°C^{-1}$
Δ_{rc_p}	-0.25	$J\,g^{-1}\,°C^{-1}$
C_{rc_p}	1.10	$°C^{-1}$
σ	16.5	°C
K_{lf}	1.03	$W\,m^{-1}\,°C^{-1}$
K_{tf}	1.03	$W\,m^{-1}\,°C^{-1}$
a_{Kr}	0.0008	$W\,m^{-1}\,°C^{-2}$
b_{Kr}	-0.0011	$W\,m^{-1}\,°C^{-2}$
c_{Kr}	-0.0002	$W\,m^{-1}\,°C^{-2}$
d_{Kr}	-0.0937	$W\,m^{-1}\,°C^{-1}$
e_{Kr}	0.22	$W\,m^{-1}\,°C^{-1}$
f_{Kr}	0.12	$W\,m^{-1}\,°C^{-1}$
ρ_f	2580	$kg\,m^{-3}$
ρ_r	1105	$kg\,m^{-3}$

Thermal Expansion
The CTE of the composite is implemented in both the longitudinal and transverse direction. Using equations 2.28 and 2.29, respectively the longitudinal- and transverse CTE are implemented, for which all corresponding parameters are included in tables 3.3 and 3.4 [46, 47]. The CTE of the resin can be implemented using equation 2.30, for which the required parameters are given in table 3.3.

Resin Shrinkage
For the epoxy resin used within the model, the total volumetric shrinkage is determined at 5.6%, which corresponds to a linear shrinkage of 1.9% [48]. As only two experimental data points are available for this epoxy resin, a linear dependence of the shrinkage on the DOC is implemented using equation 2.31. To include the shrinkage effects in longitudinal and transverse direction within the FEA model, equations 2.32 and 2.33 are used, respectively.

3.4.3. Mechanical Properties

For the mechanical behaviour of the composite, only four different mechanical components can be defined to implement the transversely isotropic material within the FEA model. An overview of the stiffness matrix definition and the relation between these components are reported in [65]. The first two components are the modulus in longitudinal and transverse direction, which can be defined by:

$$E_l = v_f E_{lf} + (1 - v_f) E_r \tag{3.4}$$

Table 3.3: Parameters for expansion and shrinkage properties of Airstone™ 780E/785H epoxy resin [80]

Parameters	Values	Units
a_{lf}	5.0×10^{-6}	°C^{-1}
a_{tf}	5.0×10^{-6}	°C^{-1}
a_{glass}	6.0×10^{-5}	°C^{-1}
a_{rub}	1.7×10^{-4}	°C^{-1}
C_m	0.4	°C^{-1}
σ_m	10.2	°C
γ_α	1.9×10^{-2}	

$$E_t = \frac{E_r}{1 - \sqrt{v_f}\left(1 - \frac{E_r}{E_{tf}}\right)} \tag{3.5}$$

where E_{tf} is the modulus of the glass fibre in transverse direction. The shear moduli of the composite ply can be defined by the following expressions:

$$G_{12} = \frac{G_r}{1 - \sqrt{v_f}\left(1 - \frac{G_r}{G_{12f}}\right)} = G_{13} \tag{3.6}$$

$$G_{23} = \frac{G_r}{1 - \sqrt{v_f}\left(1 - \frac{G_r}{G_{23f}}\right)} \tag{3.7}$$

where G_r, G_{12f} and G_{23f} are the resin shear modulus and the two fibre shear moduli, respectively. Note that both shear moduli are equal within this study, since the two shear moduli of the glass fibre are equivalent. The last component is the in-plane Poisson's ratio of the composite, which follows from [46]:

$$\nu_{12} = v_f \nu_{12f} + (1 - v_f)\nu_r \tag{3.8}$$

Resin Modulus and Poisson's Ratio

The resin modulus and Poisson's ratio are implemented using the Tg dependent expressions defined by equations 2.34 and 2.35, respectively. For these equations, the applicable parameters for implementing the glass fibre and epoxy resin in the model are given in table 3.4 [48, 88, 89].

Table 3.4: Parameters for mechanical properties of E-glass fibres and Airstone™ 780E/785H epoxy resin [48]

Parameters	Values	Units
E_{lf}	73.1	GPa
E_{tf}	73.1	GPa
G_{12f}	30	GPa
G_{23f}	30	GPa
ν_{12f}	0.22	
E_{glass}	4.61	GPa
E_{glassT}	-0.012	GPa °C^{-1}
E_{rub}	0.04	GPa
ν_{glass}	0.35	
ν_{rub}	0.5	
C_m	0.4	°C^{-1}
σ_m	10.2	°C

3.5. Sensitivity Analysis

The numerical parameters that determine the size of the time increment of the cure simulation influences the prediction accuracy of the output data, such as the resin modulus and the residual stress development. Since multiple output variables depend on the prediction of the DOC evolution, this resin property is selected as main objective for this sensitivity study. By analysing the convergence rate, and by comparing the output of the cure simulation with available experimental DSC data, the influence of the numerical parameters are analysed and the most suitable preset values for the cure simulation are determined.

3.5.1. Numerical Input Parameters

As explained within section 3.3.1, the size of time increments of the cure simulation is determined by automatic time incrementation. In general smaller increment sizes result in more accurate predictions but at the expense of computational effort and therefore simulation time. Because the calculations for the FEA solver are relatively easy to solve, cutbacks almost never occur which results in the minimum allowed time incrementation size never being required to obtain the solution for the current increment. On the contrary, the maximum time incrementation size is reached after only a couple of increments, which is why the variations of the following numerical parameters only focuses on the maximum time increment size settings, since only this one is expected to be bounding.

Two numerical parameters are selected for which either one is always bounding the maximum time increment size. These parameters are the maximum allowable increment time, t_{max} [s], and the maximum allowable temperature change per increment, ΔT_{max} [°C/inc.]. The latter parameter ensures that whenever the temperature change within a time increment exceeds the prescribed value, a cutback is initiated after which calculation of a smaller time increment is repeated until the temperature change within this increment is below the prescribed limit. The variations for both numerical parameters are given in table 3.5. By definition, the maximum allowable temperature change in an increment can be redefined into a maximum allowable increment time for heating- and cool down stages, since the heating- and cool down rates are known. However, both numerical parameters are required for the thermal-mechanical analysis within this study and because all cure cycles include heating-, isothermal and cool down stages, one of two parameters is always bounding the maximum increment size and is therefore investigated for different type of cure cycles.

Table 3.5: Numerical parameter variation of cure model - Sensitivity analysis

Numerical parameter	Unit	Variation	Applicable cycle
t_{max}	[s]	[10, 100, 500, 2000, 4000]	Isothermal
ΔT_{max}	[°C/inc]	[1, 3, 5, 10, 20]	Dynamic

3.5.2. Methodology of Analysis

A cubical unit cell model is created in which all FEA model characteristics from sections 3.2 and 3.3, and all thermal-mechanical resin properties are included. By dimensioning the unit cell with 1.75 mm edges, the model sample weight is about 6 mg which is similar to the DSC data obtained by Struzziero and Teuwen [80], and in agreement with the 2-10 mg weight range for DSC experiments [26, 90, 91]. Using a mesh convergence study, the mesh structure is determined and based on eight equal-sized elements.

In total five cure cycles are being used; four isothermal cycles with dwell temperatures of 50, 70, 90 and 110 °C and one dynamic cycle with 1 °C/min [80]. These cycles are implemented on the bottom surface as heating mould using the DISP subroutine, while on the remaining side- and top surface a convection boundary condition is implemented using the FILM subroutine. Despite that these may not be directly representative for the heat application used by DSC, it is expected that due to the low sample weight and therefore absence of large temperature gradients the analysis can still give understanding of the model convergence rate and error with respect to the experimental data. As presented in the last column of table 3.5, the influence of the numerical parameter t_{max} is analysed using the four isothermal cure cycles, as only this parameter can limit the time increment size whenever temperature is stable.

The influence of the numerical parameter ΔT_{max} is analysed using the dynamic cure cycle. For all variations and cycles the initial time increment size is set on 10s, which can be increased up to the maximum increment size allowed for that analysis.

For all isothermal cycles, an initial ambient temperature equal to the isothermal cure temperature is implemented. For the dynamic cure cycle, an initial temperature equivalent to the experimental data temperature of -1 °C is used. Although in practice the resin sample is heated rapidly from ambient- to experiment temperature before being subjected to DSC measurements, for the isothermal cure cycles the isothermal value is directly implemented as initial temperature. The impact of this instantaneous initial temperature implementation must be considered during interpretation of the results since this can have effect on the initial cure rate by overestimating it. Regarding the initial DOC, an equal value as from the experimental data has been implemented for each model.

Interpolation of the simulation output data is performed to end up with an equal amount of data points as for the experimental data. These interpolated data sets with the DOC evolution graphs are included in appendix C. Using the interpolated data, the influence of the time increment size can be analysed via both the convergence rate and error of the DOC evolution data.

3.5.3. Results and Discussion

The difference in DOC evolution between the model and experimental data is plotted against the DOC values by means of the relative error using figures 3.2 and 3.3, for the isothermal cycles and dynamic cycle, respectively. The true error graphs of both cycles on which these relative error graphs are based, are included in appendix C.

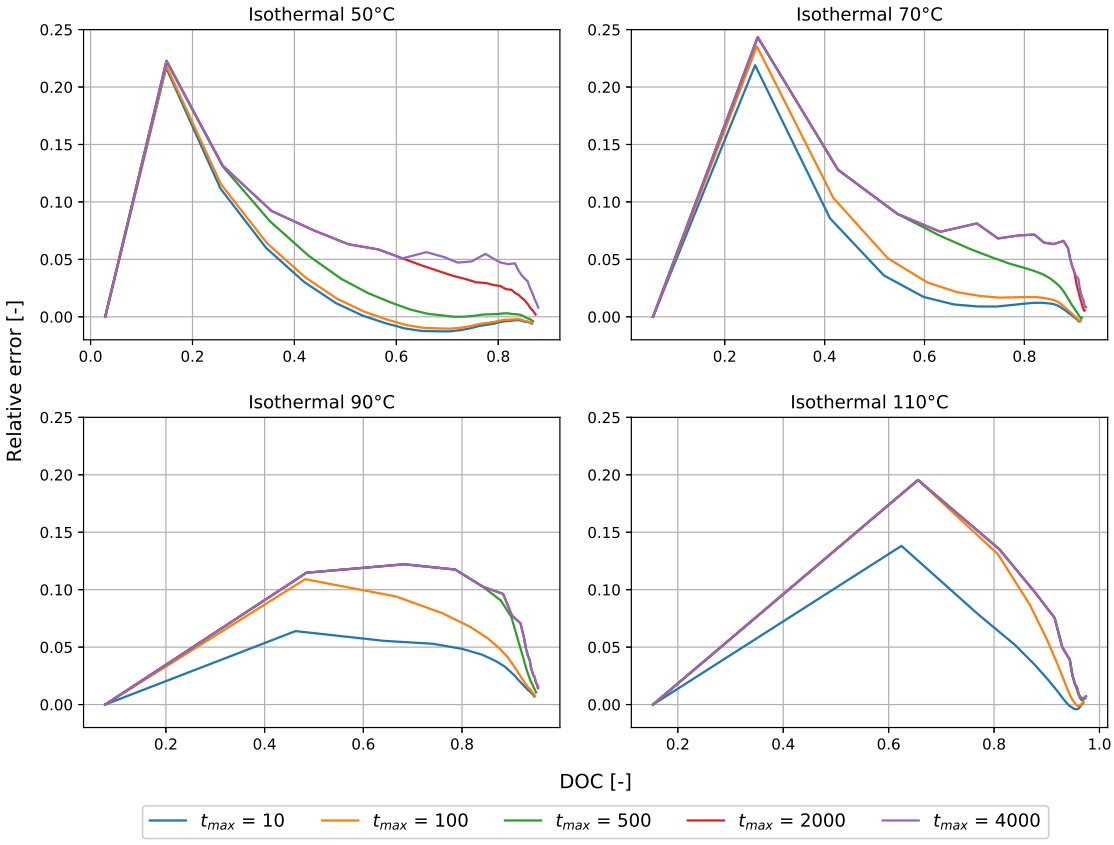

Figure 3.2: Relative error - DOC development, Numerical vs. Experimental - Isothermal cycles with 50, 70, 90 and 110 °C

Regardless which cure temperature and time increment size is used, for the isothermal cycles all graphs show an initial peak of the relative error, which shifts to higher DOC values whenever the isothermal

temperature is increased. For the 50 and 70 °C cycles, the error curves for $t_{max} \leq 500$s quickly converges to the curve for t_{max}= 10s, while this effect is less observable for the 90 and 110 °C cycles. The shift of the initial error peak to higher DOC values is caused by the increased cycle temperatures, which results in a more rapid initial DOC evolution. As consequence, DOC predictions become less accurate and therefore a lower convergence rate of the error for smaller increment sizes can be observed. When comparing the 50 and 70 °C cycles with the 90 and 110 °C cycles, it is clearly visible that for the former cycles the error drops more rapidly below 5% after the initial peak, while for the latter two cycles this point is only reached at around 0.8 or higher. It is preferable that this peak occurs at the beginning of the DOC evolution and away from the gelation point, which is set on 0.6 for this resin system, because from upon this point large errors in DOC values directly result in large deviations in resin modulus predictions. This can affect the prediction of residual stress levels by becoming less accurate [48].

For the dynamic cycle the relative error of the DOC evolution only shows a large relative error peak at the start of the cycle. This peak can be ignored since the absolute DOC value is insignificantly low at this stage of the cycle. Note that the graph in figure 3.3 is magnified for a more detailed overview of the error progression where the error maximum is outside the range of the graph limits. As can be seen in the graph, directly after the peak the relative error of ΔT_{max}= 1 and 3 °C/inc. rapidly converges without exceeding the 10% margin before the gelation point is reached. The complete graph is included within figure C.4.

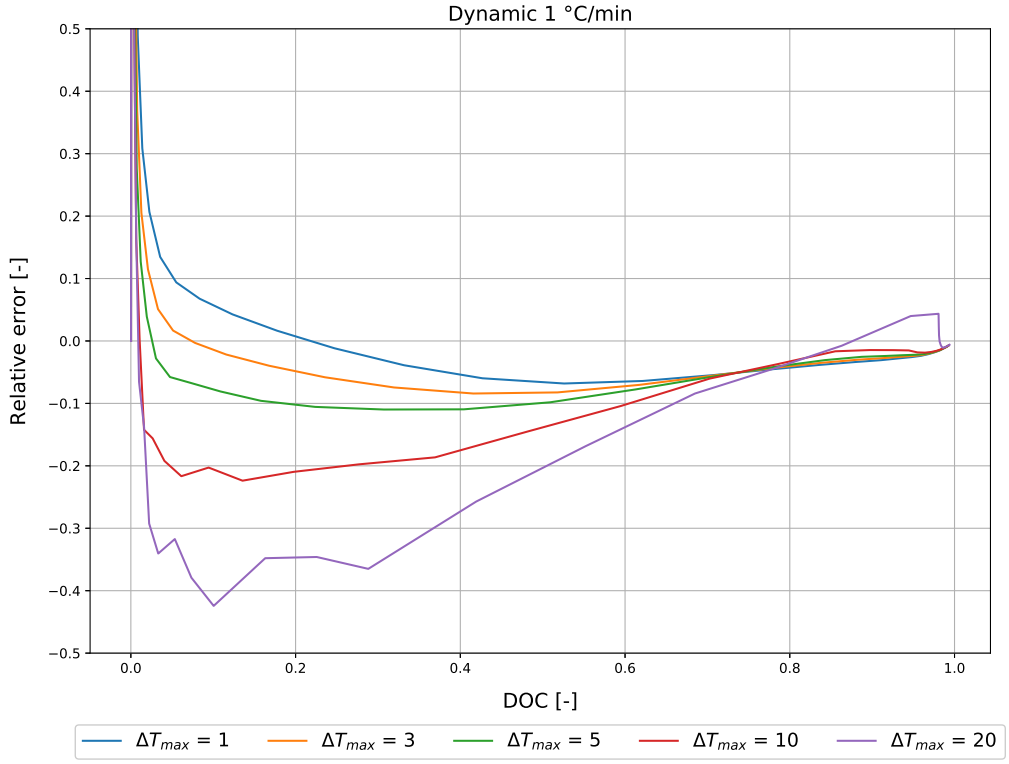

Figure 3.3: Relative error - DOC development, Numerical vs. Experimental - Dynamic cycle with 1 °C/min

3.5.4. Numerical Parameter Selection

Maximum Allowable Increment Time

As described above, the cure models of the isothermal cure cycles with a maximum allowable increment time of 10s and 100s end up with sufficient accuracy in terms of convergence rate and DOC predictions. For the first three isothermal cycles it can be observed that the relative error decreases to less then 5-10% before the gelation point of the resin is reached. Because only small differences can be observed between 10s and 100s for the 50 and 70 °C isothermal cycles, it is concluded that 100s as limit for

the maximum allowable increment time is sufficient for cure simulations within this research project. Whenever a more detailed simulation is required because it is suspected that accuracy is lost due to the maximum time increment size at higher cure temperatures, an additional analysis with smaller maximum allowable increment time of 10s can be considered.

Maximum Allowable Temperature Change per Increment
The maximum allowable increment time is determined on a limit of 100s for the cure model, which can be translated to a maximum allowable temperature change per increment of 1.67 °C/inc. whenever the dynamic cure cycle is considered. From figure 3.3, it can be observed that for a maximum allowable temperature change per increment of 1 °C/inc., the DOC evolution model output is the most accurate without exceeding the 10% error after the initial peak. This value is therefore selected for the maximum allowable temperature change per increment. With this value, the maximum temperature change per increment parameter is dominant during heating- and cool down stages whenever the rates are larger than 0.6 °C/min. Whenever during heating- and cool down stages this rate does not exceed this 0.6 °C/min or during isothermal stages, the maximum allowable increment time of 100s is limiting the time increment size.

3.6. Model Verification

Before the cure model can be used as basis for the ply drop-off models, verification of the model is required. This is achieved by comparing the output results of the cure model with the aforementioned research study conducted by Struzziero et al. [48], whose model has been validated by experimental warpage measurements in thermoset laminates. The main output result that is used for verification of the cure model is the generation of the residual stress throughout the cure phase. By this output, the coupling of the thermal-chemical and thermal-mechanical properties of the model can be verified. Since the residual stress results in warpage of the thermoset laminates upon demoulding, the maximum curvature of the warpage is used for verification as well to verify the mechanical response of the model [48].

3.6.1. Methodology of Analysis

The model used for verification represents a laminate with an asymmetric layup of $[0/90]_4$ which is built using the previously described thermal-mechanical FEA model [48]. Equal dimensions and FVF as described in [48] are being used. The mesh structure of the verification model followed from a convergence study and is based on 3600 elements, with a single element per ply in through-thickness direction (z-direction) and two elements in width direction (y-direction). As for the boundary conditions, equal initial-, symmetry-, thermal-, mould surface and vacuum film surface boundary conditions as reported in [48] are being used. Regarding the symmetry boundary conditions, a quarter model of the laminate is created which represents an internal strip of the laminate close to the y-symmetry plane [48]. For the mould heating and vacuum film convection surfaces, respectively the Abaqus subroutines DISP and FILM are implemented, for which the reference temperatures follow three different cure cycle profiles. These represent cure cycle 1 (MRCC), cure cycle 2 and the optimal cure cycle, as reported in [48].

Numerical Parameters - Verification Model
The sensitivity analysis showed that the influence of the numerical time incrementation parameters can influence the DOC predictions significantly. To ensure that the correlation of both the verification model output and research data can be conducted as objectively as possible, equal numerical time incrementation parameters as the research data are implemented within the verification model. These numerical parameters are based on an unlimited allowable maximum time incrementation size with an initial time incrementation size of about 500s, and with a maximum allowable temperature change per time increment of 3 °C/inc.

3.6.2. Results and Discussion

In the following sections, the correlation of the final residual stress levels and maximum laminate warpage after demoulding are elaborated. From the cure simulations it became clear that minor differences in DOC evolution can result in deviations in the development of the resin modulus which in turn

affects the residual stress. Within appendix D, the DOC, Tg and stress evolutions graphs for cure cycle 1 and the optimal cure cycle are included. Within this appendix, the graphs for cure cycle 2 have been left out since these were similar in terms of modulus and residual stress deviations to cure cycle 1. By comparing the resin modulus development in addition to residual stress and final laminate warpage between the verification model and the research data, a well-argued conclusion can be drawn if the current thermal-mechanical cure model is suitable to be used as basis for the ply drop-off model. The research data obtained by Struzziero et al. [48] is hereinafter referred as the research model.

Final Residual Stress
For the residual stress correlation between the research- and verification model, final stress values are obtained within the 0° plies at three different locations through thickness, namely bottom, centre and top [48]. As for the verification model, the development of the resin modulus and residual stress at these locations throughout the cure phase show similar trends as the research model (see appendix D). The final residual stress values at the end of the cure phase are presented within table 3.6. Despite the small absolute differences in stress values between the two models, the final stress decreases within each ply with the implementation of the optimal cure cycle. When comparing the stress values of cure cycle 1 and 2 for the verification model, a similar decrease in stress as for the research model is observable as well. The final stress values and decreasing trends within the graphs included within appendix D are satisfactory, which implies the current model is suitable for residual stress predictions.

Table 3.6: Final residual stress of verification model. Data for correlation obtained from [48]

	Residual stress σ_{11} [MPa]					
	Struzziero et al. [48]			Verification model		
Cure cycle	Bottom	Center	Top	Bottom	Center	Top
1 (MRCC)	12	17	22	11	16	20
2	12	16	21	11	15	19
Optimal	12	16	20	10	14	18

Maximum Warpage
The maximum laminate warpage as result of the residual stress redistribution after demoulding is compared as well. At the end of the cool down stage, the vacuum film pressure is disabled by which a demoulding effect is simulated, resulting in warpage of the laminate with a maximum predicted deflection in z-direction. The measured and predicted warpage obtained by Struzziero et al. [48] and the predicted warpage resulted from the current verification model are presented in table 3.7. The predicted warpage values from the models are in the same order of magnitude, with the same decrease of 10% warpage with the implementation of the optimal cure cycle compared to the MRCC. The difference in absolute values of the maximum deflection between both can be explained by the stress differences as presented in the previous section.

Table 3.7: Laminate warpage results of verification model. Data for correlation obtained from [48]

		Predicted warpage [cm]	
Cure cycle	Measured warpage [cm] Struzziero et al. [48]	Struzziero et al. [48]	Verification model
1 (MRCC)	1.8$\pm$0.5	2.0	1.6
2	1.6$\pm$0.5	1.9	1.5
Optimal	N.A.	1.8	1.4

3.7. Conclusions
Verification of the model showed that the coupled thermal-mechanical model is capable of predicting the residual stress accurately. Both the final residual stress values and maximum warpage predictions

after demoulding are in close agreement with the model used by Struzziero et al. [48]. Despite small deviations in residual stress development throughout the cure cycle between the model and the research data, similar trends and directions of the stress development are observed as result of heating-, dwell- and cool down stages. Therefore, it is concluded that the thermal-mechanical cure model built within Abaqus is suitable and can therefore be used for the prediction of cure-induced residual stress around ply drop-off regions and the investigation regarding influencing parameters.

4

Ply Drop-off Model

Section 4.1 describes the single ply drop-off model within a thin laminate. This model is used to investigate the fundamentals influence of the ply drop-off and influencing parameters on residual stress around these regions. Section 4.2 describes the transition to a thick laminate in which the ply drop-off is implemented. Using this model, the influence of the increased thickness and process influences are investigated. The last iteration involves modelling multiple ply drop-off regions within a thick laminate, which is described in section 4.3. This model is used to investigate the influence of the multiple ply drop-off configurations on the residual stress.

4.1. Ply Drop-off Model - Thin Laminate

For the implementation of the ply drop-off region within a laminate, the model from chapter 3 is extended by including the ply drop-off geometry. Because differences between ply drop-off regions within thin- and thick laminates are expected due to temperature gradients through-thickness, first a thin laminate model is established. As shown in figure 4.1, this model is built using nine horizontal NCF plies, defined as the thick section, in which the fifth ply is terminated at about half the length of the model. As result of this terminated ply, the drop-off section and resin pocket are introduced. Followed by this drop-off section is the thin section which consists of eight plies. The ply thickness is equal throughout the complete laminate. The mesh of the model, for which the mesh structure is described in section 4.1.2, is based on the same brick elements as the verification model. To each ply within the model, an unique orientation can be assigned, resulting in each ply having orthotropic material properties. Furthermore, within the resin pocket region only the isotropic resin material is implemented.

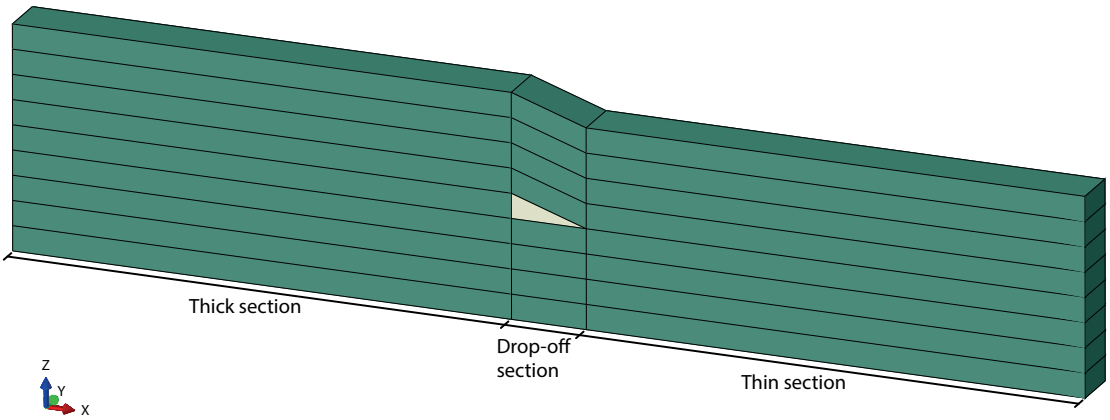

Figure 4.1: Schematic example of thin laminate ply drop-off model (without mesh structure) with ply- and resin pocket sections

4.1.1. Geometry and Boundary Conditions

The geometry of a ply drop-off can be described by the aspect ratio a/b, which is visualized by the enlarged schematic A within figure 4.2. This study only includes ply drop-off regions resulting from a single terminated ply, which implies that the height a of the pocket is per definition equal to the ply thickness of 0.25mm, while the length b is variable and can be used to analyse different ratios. The length of the thick- and thin section is determined as such that no influences can be observed at the drop-off region originating from the edges of the model. Only considering a single terminated ply is justified by the assumptions reported in the next section, which imply excluding inter-ply failures from the analysis. As result, no distinctive differences are expected whenever multiple plies are terminated at once. In addition, terminating a single ply corresponds to the current design guidelines reported in section 2.5.

In practice the ply drop-off region is located within a laminate and enclosed by one or multiple plies, and therefore not located at any laminate edges. As can be seen in figure 4.2, by implementing fixed displacement boundary conditions in one x-direction and both y-directions of the model, an internal cross sectional strip of the laminate is considered. With these, the internal effect of ply drop-off regions on the residual stress can be investigated without taking into account the influence of edge effects. Regarding the process boundary conditions, a fixed displacement moulding surface and vacuum film convection surface boundary condition is implemented, for which the reference temperatures of both follow prescribed temperature profiles based on the cure cycle. For each of these surface conditions, the required subroutine is given in figure 4.2.

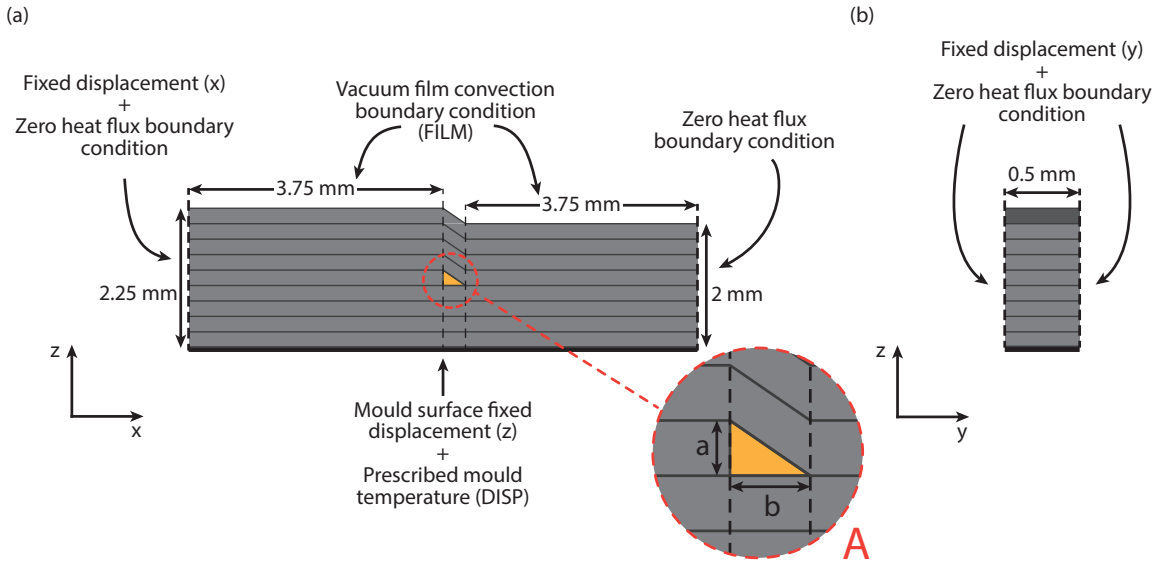

Figure 4.2: Schematic of thin laminate ply drop-off model geometry and boundary conditions: (a) xz-view and (b) yz-view

Ply Drop-off Model Assumptions

As an extension to the model assumptions described in section 3.2.2, additional assumptions can be defined for the ply drop-off model as follows:

- The resin pocket is to be assumed an idealized right-angled triangle. By this assumption, over-estimation of stress concentrations at the sharp geometry corners as result of the cure-induced stress is expected, which must be considered when interpreting the results by means of stress contour plots.
- Although in practice deformations as result of the vacuum pressure of the VARTM process are expected, it is assumed that the geometry of the resin pocket, the terminated ply-end shape, and the oblique plies of the laminate remains undistorted prior to the cure phase. Note that deformations of these regions can still occur during the cure phase itself as result of the evolutions of material properties, and expansion and shrinkage effects.

- Since the effects of intra-ply and inter-ply failures are outside the scope of this study because no cohesive elements are included within the analysis, the laminate plies are assumed to be perfectly bonded and no separation can occur throughout the cure simulation.
- It is assumed no voids are present within the resin pocket or surrounding laminate, and no voids can arise as result of the cure effects.
- Since no voids can be present in and around the resin pocket, it is assumed no separation between the neat resin within the pocket and surrounding plies can occur.

4.1.2. Mesh Convergence

A mesh convergence study is conducted to determine the most efficient mesh structure in terms of computational cost and convergence rate. For this convergence study, six different structures with varying element sizes are created, with mesh 1 having the largest element size and mesh 6 the smallest. Because the region of interest is only around the ply drop-off, the mesh structure is based on biased horizontal and constant vertical mesh seed edges. For the y-direction of the model, a single element is used for each mesh structure. Within appendix E, a more detailed elaboration is given regarding the mesh seed edge layout. Within table 4.1 the successive mesh structure refinements with corresponding seed edge sizes is given for the ply drop-off model with aspect ratio 1/1.5.

For this convergence study the maximum out-of-plane stress within the belt ply is analysed, as shown in figure 4.3. For each successive mesh refinement, the stress output is compared with the previous courser mesh structure. Whenever the relative change between the output values of two successive mesh structures is below the 5% margin, the solution is assumed to be converged. As can be seen within the table, the solution for mesh 4 is already below this margin with aspect ratio 1/1.5, and therefore convergence has been reached. This converging trend can also be observed within figure 4.4, in which both the stress output and linear increasing solver time with respect to the increasing number of elements is illustrated. This mesh convergence study is performed for all ply drop-off models with different aspect ratios that are used for the analysis dedicated to the influence of the drop-off geometry. For all models the same mesh structure is used for the sake of model replication and adaptability, for which all mesh structures are based on mesh 5. Using this mesh, the largest relative difference below the 5% margin resulted in 2.5% for the model with an aspect ratio of 1/24.

Table 4.1: Mesh convergence study - Thin ply drop-off model (a/b = 1/1.5)

Approx. seed edge size [mm]	Mesh 1	Mesh 2	Mesh 3	Mesh 4	Mesh 5	Mesh 6
H1 (maximum)[1]	1.0	0.5	0.25	0.25	0.25	0.25
H1 (minimum)[1]	0.1	0.05	0.025	0.02	0.015	0.0125
H2	0.1	0.05	0.025	0.02	0.015	0.0125
V1/V2	0.125	0.1	0.05	0.03	0.025	0.02
Number of elements	388	1180	3966	7050	9894	14125
Relative change with respect to previous mesh [%]	-	3.7	5.2	2.9	0.7	0.6

[1] Biased mesh seed edges require a maximum and minimum size value. For each mesh the element size decreases from the coarsest element at the laminate edge (maximum size), to the finest element at the drop-off section (minimum size).

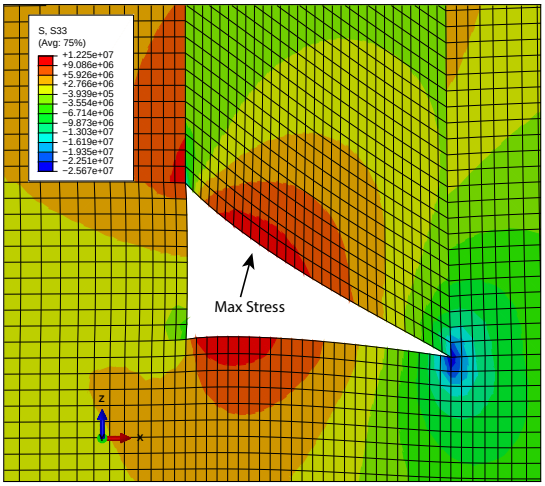

Figure 4.3: Location of maximum out-of-plane tensile stress within belt ply for thin laminate ply drop-off model (a/b = 1/1.5). Resin pocket is hidden for clarification

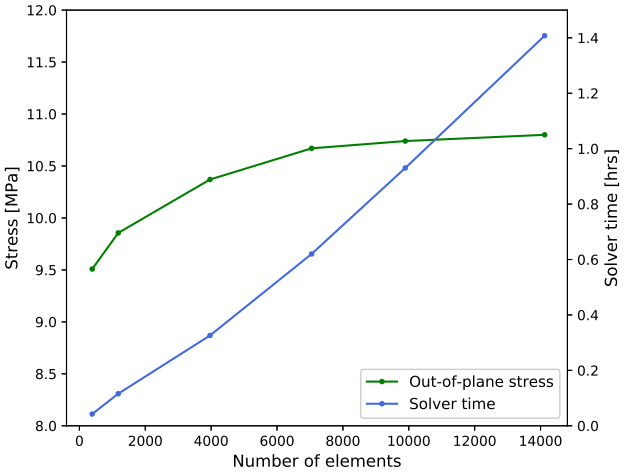

Figure 4.4: Mesh convergence study - Thin laminate ply drop-off model: Converging trend of stress output and analysis solver time versus number of elements

4.1.3. Oblique Belt Ply Implementation within Abaqus

Followed from the assumptions described in section 4.1.1, due to the resin pocket geometry the ply drop-off region is idealized by an oblique-shaped belt ply. As a consequence, the transition from the thick section to the drop-off section results in an abrupt change of the local material orientation. This effect, which was already visible within the contour plot of the previous mesh convergence study, can be observed more clearly for both the core- and belt ply contour plots illustrated within figure 4.5. In this figure, for each section the local material orientation is visualized by the x-z datum axis. As can be seen in figure 4.5a, a gradual and continuous change of the different stress contour levels can be observed within the core ply at the transition from the thick section to the drop-off section. This continuous region is the result of the material orientation, which remains unchanged between both sections. Differently is this transition within the belt ply, depicted by figure 4.5b, where a discontinuous change of contour levels can be observed due to the abrupt change of the local material orientation. It is important to take the influence of these discontinuous transition regions into account when interpreting contour plot results, because the stress values at these locations can be under- or overestimated by the FEA solver. Therefore, exact stress values are only obtained at the core- and belt ply regions away from the pocket corners to minimize the influence of this effect.

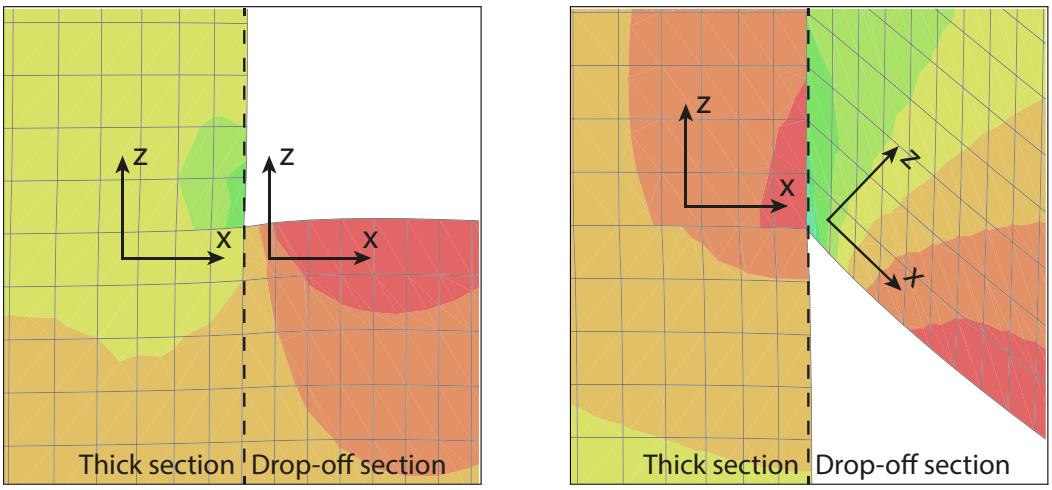

(a) Core ply

(b) Belt ply

Figure 4.5: Transitions of material orientation from thick section to drop-off section

4.2. Ply Drop-off Model - Thick Laminate

It is expected that for the process influence analysis the thickness of the laminate may affect the results, since an increased thickness of the laminate introduces the possibility of exothermic reactions and temperature gradients through-thickness.

4.2.1. Geometry and Boundary Conditions

As result of the thickness increase, the geometry of the ply drop-off model is slightly modified. As can be seen within the schematic illustrated by figure 4.6, the thick laminate model is defined by a thick section and a thin section, which consist out of 73 and 72 plies, respectively. Identical ply thickness, boundary conditions and model assumptions as for the thin laminate model are implemented with an aspect ratio of 1/1.5. For the ply orientations, an arbitrary and symmetric layup is defined to be more realistic. By using symmetry, influences of cure-induced laminate warpage or other in-plane and out-of-plane coupling effects are excluded from the analysis. For the following model, the thick section is based on a $[(\pm 45/0_3/90)_{3s}/0_{1D}/(\pm 45/0_3/90)_{3s}]$ symmetric layup and the thin section is based on a $[\pm 45/0_3/90]_{6s}$ symmetric layup. The ply orientations for both layups with the internal resin pocket are depicted by figure 4.6 as well.

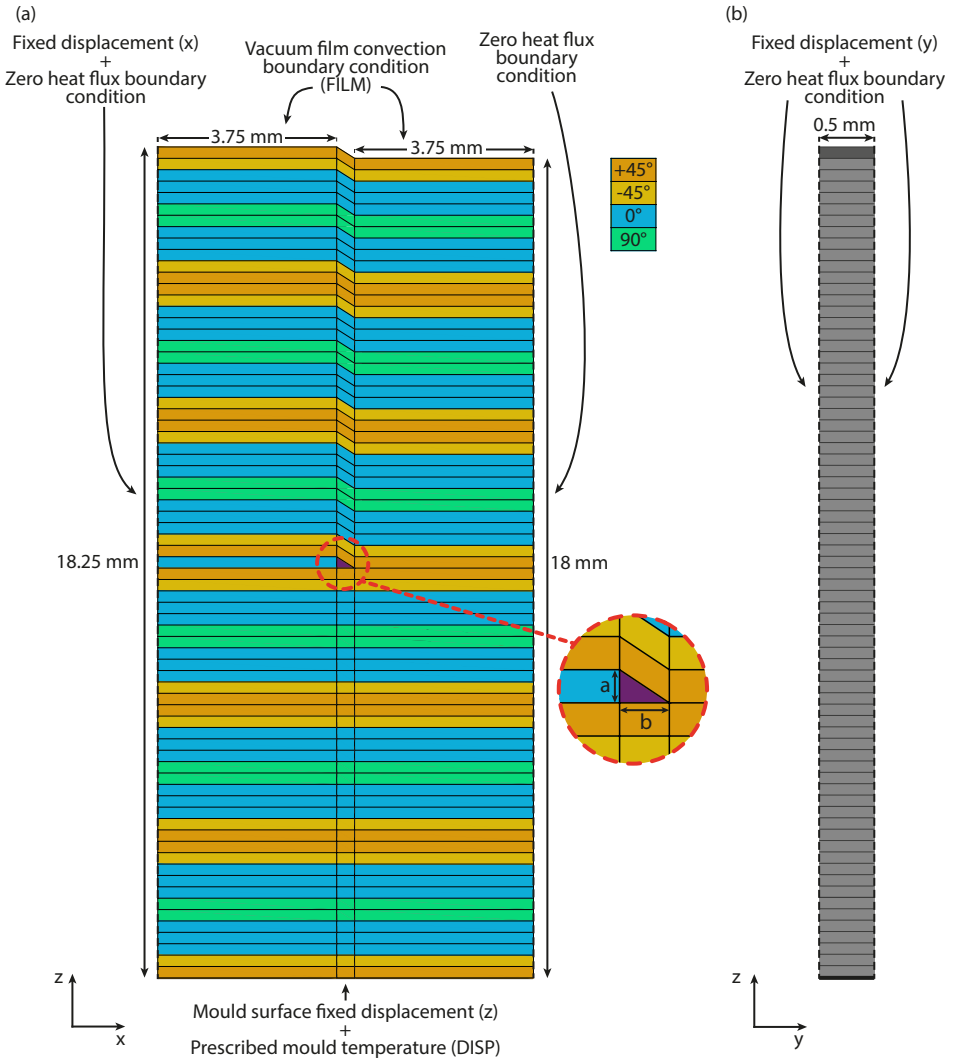

Figure 4.6: Schematic of thick laminate ply drop-off model geometry and boundary conditions: (a) xz-view with laminate ply orientations and (b) yz-view

4.2.2. Mesh Convergence

A mesh convergence study is executed with an equal approach as described for the thin laminate model. Using a modified mesh seed edge layout, included within appendix E, four different mesh structures are defined. As output for this convergence study the maximum out-of-plane stress is selected, which is located within the core ply. As can be seen in table 4.2, mesh structure 4 resulted in 2.0% relative difference with respect to the courser mesh structure. Since this value is below the aforementioned 5% error margin, it is assumed convergence has been reached and therefore this mesh structure can be used.

Table 4.2: Mesh convergence study - Thick laminate, single ply drop-off model (a/b = 1/1.5)

Approx. seed edge size [mm]	Mesh 1	Mesh 2	Mesh 3	Mesh 4
H1 (maximum)	0.25	0.25	0.25	0.25
H1 (minimum)	0.015	0.015	0.015	0.015
H2	0.015	0.015	0.015	0.015
V1	0.125	0.0625	0.03	0.025
V2	0.25	0.125	0.1	0.0625
V3	0.25	0.25	0.25	0.25
Number of elements	9502	15138	22497	28373
Relative change with respect to previous mesh [%]	-	11.3	7.5	2.0

4.3. Multiple Ply Drop-off Model

Within composite laminates, generally more than one ply drop-off is implemented to achieve the required thickness variation along the composite part. By implementing more than one ply drop-off region within these laminates, additional parameters and interactions are introduced, which are expected to influence the cure-induced residual stress at these regions. To investigate these parameters and interactions, the thick laminate drop-off model from section 4.2 is modified by implementing multiple drop-off regions.

4.3.1. Ply Drop-off Topologies

The arrangement of multiple ply drop-off regions within laminates can be implemented using different topologies. For this research study, two different topologies in the most basic arrangement are proposed for terminating a single ply within each drop-off region, where both include three successive ply drop-offs. The proposed topologies are schematically illustrated by figure 4.7. As can be seen in figure 4.7a, the three drop-offs share the same core ply, while the belt ply of the first drop-off is the terminated ply within the second drop-off, and so on. This is different for topology 2, depicted by figure 4.7b, where the belt ply is equal for all drop-offs while the core ply of each previous drop-off is the terminated ply within the next drop-off.

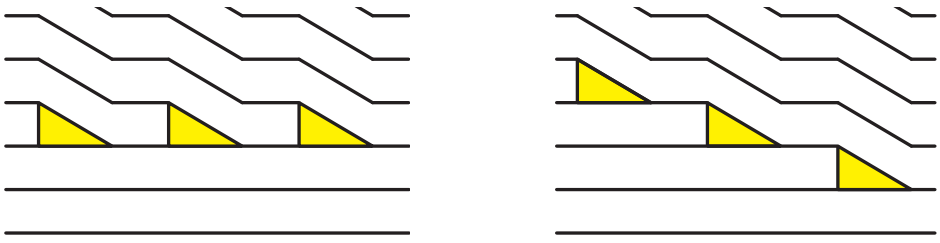

(a) Topology 1: Shared core ply

(b) Topology 2: Shared belt ply

Figure 4.7: Schematic topologies of multiple ply drop-off models

4.3.2. Geometry and Boundary Conditions

Since the thick laminate model with single drop-off is modified for the multiple drop-off model, only the changes applicable for this new model are described. As can be seen in figure 4.8, the length of both the thinnest and thickest part of the model is increased, while the thickness of the thinnest part is decreased due to the multiple drop-offs. The through-thickness position of the second drop-off remains equal for both topologies and there are different ply orientations along the three drop-offs. The variable stagger distance S, described within section 2.5, is introduced to investigate its influence on the residual stress. Regarding the aspect ratio of the drop-offs within this model, a constant value for a/b of 1/1.5 is used since this ratio resulted in the most severe residual stress development.

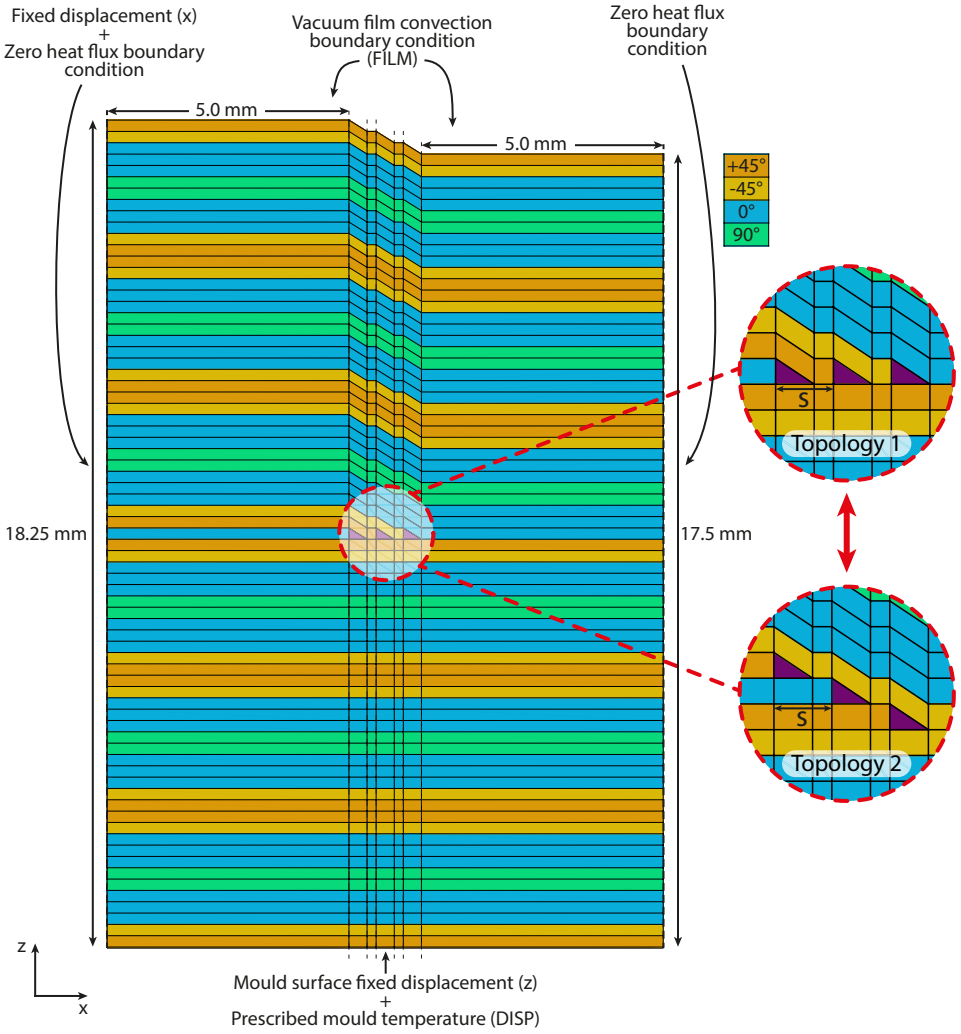

Figure 4.8: Schematic of thick laminate, multiple ply drop-off model geometry and boundary conditions: xz-view with laminate ply orientations and topologies

4.3.3. Mesh Convergence

For both topology models a mesh convergence study is conducted where the smallest stagger distance of 1.5B is implemented due to the highest expected residual stress and stress concentrations. Note that within this notation B represents the length of the resin pocket, where this length is relative to the ply thickness via the aspect ratio a/b.

The maximum out-of-plane stress within the core ply of the first ply drop-off is evaluated for each topology model. The mesh seed strategy from previous models is modified for this model and included

within appendix E. As can be seen in table 4.3, equal sizes for all seed edges are implemented for each topology. Resulting from this convergence study, mesh 4 is selected for both models for further analysis since the relative changes with respect to the previous mesh size are below the 5% margin.

Table 4.3: Mesh convergence study - Thick laminate, multiple ply drop-off models (a/b = 1/1.5 and S = 1.5B)

Approx. seed edge size [mm]	Mesh 1	Mesh 2	Mesh 3	Mesh 4
H1 (maximum)	0.25	0.25	0.25	0.25
H1 (minimum)	0.015	0.015	0.015	0.015
H2	0.015	0.015	0.015	0.015
V1	0.125	0.0625	0.03	0.025
V2	0.25	0.125	0.1	0.0625
V3	0.25	0.25	0.25	0.25
Number of elements - Topology 1	18501	29072	42516	53459
Number of elements - Topology 2	18489	29043	42911	53443
Relative change with respect to previous mesh - Topology 1 [%]	-	11.0	7.0	1.4
Relative change with respect to previous mesh - Topology 2 [%]	-	11.4	9.1	3.0

5

Cure-Induced Residual Stress around Single Ply Drop-Off Regions

Section 5.1 describes the investigation on which material properties of the resin pocket have influence on the residual stress evolution within single drop-off regions. Hereafter, focus is shifted to the pocket surroundings, where the influence of the pocket geometry and ply orientations on the residual stress are evaluated within section 5.2. Prior to investigating process influences, the transition from thin- to thick laminates and its influence is discussed within section 5.3. Using the thick laminate model, the influence of process parameters are analysed, for which the results are presented in section 5.4. This chapter ends with the conclusions presented in section 5.5.

5.1. Influence of Resin Pocket Material Properties

It is expected that multiple material property evolutions contribute to the residual stress generation throughout the cure phase. The out-of-plane stress, which is critical concerning delamination and composite failure, can result in significant concentrations within the core- and belt ply (figure 4.3). By evaluating this stress component, the influence of the resin pocket material properties can be analysed.

5.1.1. Methodology of Analysis

To analyse the influence of the resin pocket material properties, five cure simulations with different pocket material implementations are conducted. The thin laminate ply drop-off model with an aspect ratio of 1/1.5 is used, since with this ratio the most significant residual stress development and therefore distinctive material property influences can be observed. The layup is based on $[0_4/0_{1D}/0_4]$ to exclude the influence of interactions between different ply orientations on the residual stress. Within this layup notation, the subscript D indicates the terminated ply.

The five material variations are based on including thermal strain, chemical strain and the presence of the resin modulus within the resin pocket. An overview of these variations is summarized in table 5.1. For all variations, the mechanical strain is kept implemented, which can be justified knowing that this strain originates from the surroundings of an element and not from the material properties of the element itself. Note that for the fifth variation no differences can be observed whether or not any type of strain is involved. Within the pocket region, the resin modulus is the only modulus included within the stiffness matrix from equation 2.40. By neglecting this modulus, the fifth variation results in a zero-stiffness material which per definition excludes all strain types.

For each of the five variations, three different moments throughout the cure cycle are analysed for the residual stress built-up. These observation points are at the start of the dwell stage, at the end of the dwell stage and at the end of the cycle, as depicted by figure 5.1. At each observation point, the most distinctive out-of-plane stress contour plots are evaluated together with the most important observations.

Table 5.1: Variations of material properties within resin pocket

No.	Description	Thermal strain	Chemical strain	Resin modulus
1	Normal strain development	☒	☒	☒
2	Only thermal strain	☒	☐	☒
3	Only chemical strain	☐	☒	☒
4	Constant volume	☐	☐	☒
5	No resin modulus	☒	☒	☐

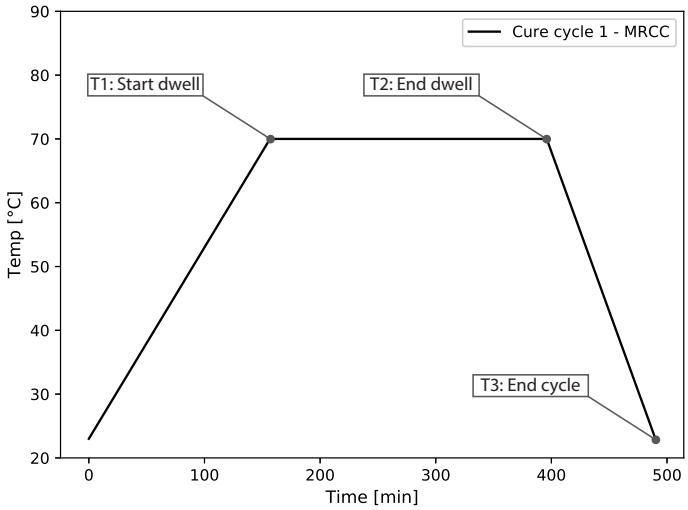

Figure 5.1: Cure cycle observation points - Influence of resin pocket material properties

5.1.2. Results and Discussion

In the following sections each observation point is elaborated separately. For all contour plots corresponding to an equal observation point, equal contour limits are used for the ease of comparison. An extensive overview of the contour plots for all variations at each observation point is included within appendix F.

T1: Start Dwell

At this point only the heating stage is completed. Since the laminate is relatively thin and no exothermic reaction takes place that can cause large temperature gradients, an evenly distributed and gradual temperature increase throughout the laminate can be observed. As result of this increase, the DOC developed to a value of 0.7 for both the ply and resin pocket regions, which subsequently results in an already significant chemical shrinkage of the resin. The Tg is around 20°C at this point, resulting in a resin modulus that is still insignificant in magnitude.

Within figure 5.2 it can directly be observed that up to this point in the cure cycle, the thermal expansion of the resin pocket is counteracted by the chemical shrinkage of the pocket. This is substantiated by the absence of any stress regions visible in figure 5.2a, while compressive- and tensile stress regions are present for the only thermal strain and only chemical strain variation, depicted by figures 5.2b and 5.2c, respectively. Whenever constant volume is implemented in the resin pocket, or whenever no modulus development for the pocket is implemented representing a void (variation 4 & 5, respectively), the induced stress within the drop-off region is insignificant and similar to the normal strain variation.

For the only thermal strain variation, depicted by figure 5.2b, the compressive stress regions in the core- and belt ply originate from the thermal expansion and simultaneous chemical shrinkage in through-thickness direction of the surrounding plies while the pocket is only thermally expanded. This results in compression of the pocket, compressive stress regions in core- and belt ply, and tensile stress concentrations at the end of the terminated ply. The opposite effect is observable for the only chemical

strain variation, depicted by figure 5.2c, where tensile stress regions are induced within the core- and belt ply originating from the larger effective shrinkage of the pocket compared to its surroundings.

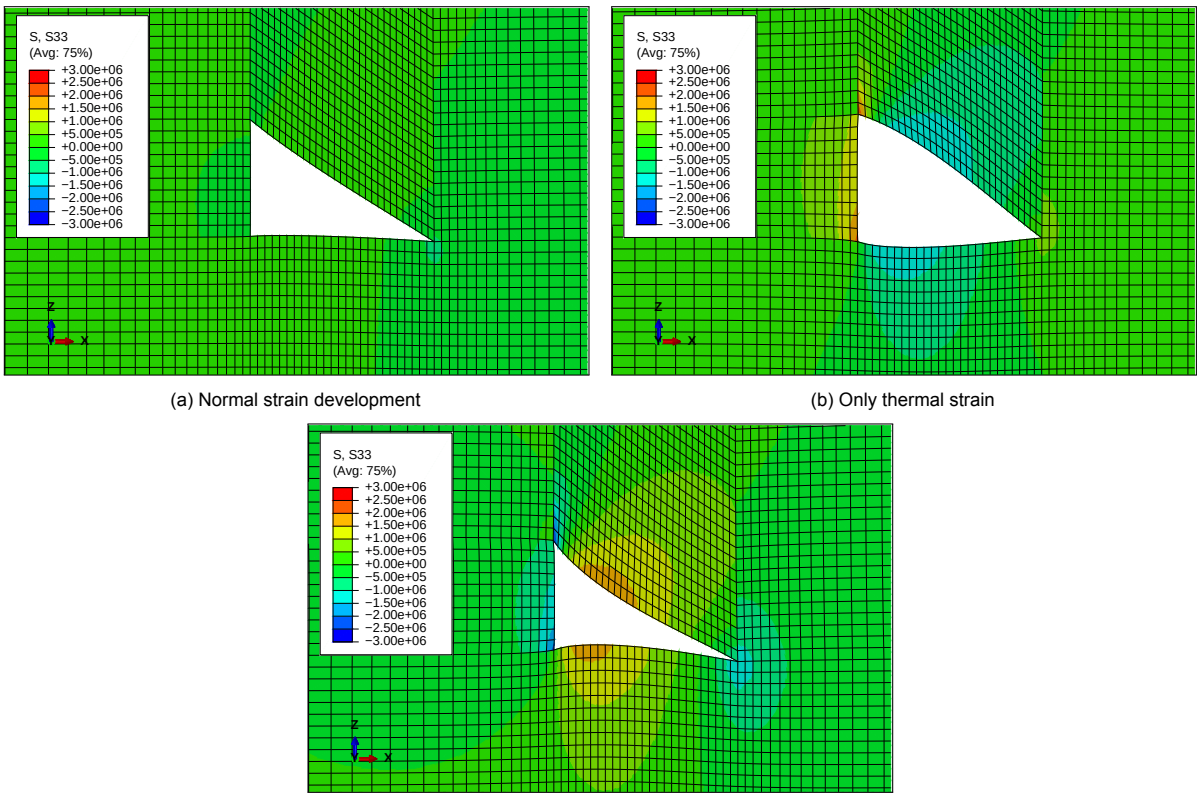

(a) Normal strain development

(b) Only thermal strain

(c) Only chemical strain

Figure 5.2: Out-of-plane stress contour plot as result of material property evolutions within resin pocket. Thin laminate ply drop-off model (a/b = 1/1.5). Time = 156 min (Start dwell), DOC = 0.7. For clarification a deformation scale factor of 10 is used and the resin pocket is hidden. Unit of contour limit values in Pascal

T2: End Dwell

As result of the dwell stage, the DOC developed to a value of 0.92. At this point, the Tg is around 66 °C with a resin modulus of 3.4 GPa. No through-thickness temperature gradients by exothermic reactions have occurred, therefore only an increase in chemical shrinkage of the resin has taken place. Combined with the increased resin modulus, both the tensile- and compressive stress regions in the core- and belt ply observed at the start of the dwell stage increased for all variations.

Since the stress regions for the only chemical strain variation, depicted by figure 5.3b, are more pronounced compared to the normal strain variation within figure 5.3a, it can be concluded that the stress increase during the dwell stage is a direct result of the increased chemical shrinkage of the resin pocket. For the only thermal strain variation, the dwell stage results in minimal stress increase within the core-/belt ply and terminated ply-end, which is caused by the increase in through-thickness chemical strain of the surrounding plies. Regarding the fourth and fifth material variation, no inexplicable effects can be observed other than already discussed.

T3: End Cycle

During the cool down stage, no further development in DOC can be observed, meaning no increase in resin shrinkage has taken place. However, as result of this cool down, thermal contraction and an increase of the modulus to 4.3 GPa results in changes of stress levels for all material variations. From previous section the Tg was determined at 66°C at the end of the dwell, meaning vitrification has taken place at the beginning of the cool down stage.

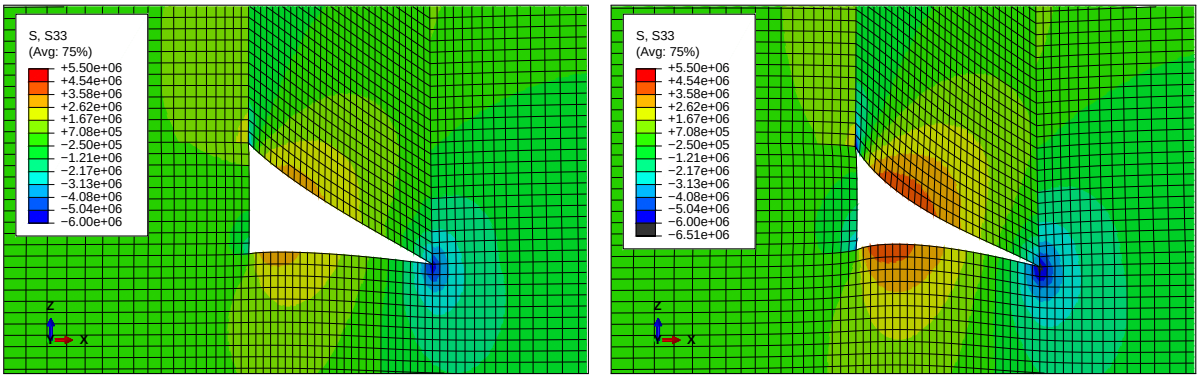

(a) Normal strain development

(b) Only chemical strain

Figure 5.3: Out-of-plane stress contour plot as result of material property evolutions within resin pocket. Thin laminate ply drop-off model (a/b = 1/1.5). Time = 396 min (End dwell), DOC = 0.92. For clarification a deformation scale factor of 10 is used and the resin pocket is hidden. Unit of contour limit values in Pascal

For the normal strain variation, depicted by figure 5.4a, the relatively higher thermal contraction of the pocket compared to its surroundings only results in an increase of the previously described stress regions. For the only chemical strain variation, depicted by figure 5.4b, the compressive regions within core-/belt ply changed into tensile regions, as the deformed surroundings of the thermally expanded pocket vitrified at the beginning of the cool down stage after which the pocket thermally contracted to a greater extend compared to the surroundings. The opposite occurred for the only chemical strain variation, depicted by figure 5.4c, where due to the thermal contraction of the surrounding plies the tensile regions within the core- and belt ply almost completely disappeared. Whenever only the surrounding plies have influence on the stress generation, which is applicable for variation 4 depicted by figure 5.4d, it can be concluded that due to the effective chemical shrinkage and thermal contraction through-thickness, still significant tensile stress regions are generated at the terminated ply-end.

5.1.3. Concluding Remarks

From the results above, multiple important phenomena can be identified. At the end of the heating stage, the thermal expansion and chemical shrinkage of the resin pocket developed in a counteracting manner. This combined with a relatively low resin modulus results in an almost stress-free drop-off region, up to the point where the expansion stabilizes due to the dwell while the resin shrinkage continues.

During this dwell stage, tensile stress regions within the core- and belt ply starts to develop as result of this increase in resin shrinkage. Due to the surrounding plies that predominantly shrink in through-thickness direction during this stage, a compressive stress concentration starts to develop within the plies at the lower-right corner of the pocket, while a tensile stress region can be observed within the plies at the top-left corner of the pocket. Both these stress regions and concentrations increase in magnitude as result of the cool down stage, for which the thermal contraction of the resin is the main contributor.

It can be concluded that due to the material evolution of the resin, predominantly within the resin pocket, both the chemical shrinkage and thermal contraction during the dwell- and cool down stage, respectively, have the most significant contribution to the stress generation within ply drop-off regions.

5.2. Influence of Resin Pocket Geometry and Ply Orientation

The aspect ratio, illustrated within figure 4.2, is an important geometry parameter which is generally described by laminate design guidelines and influenced by the flexibility of the covering belt ply in the drop-off direction and thus its in-plane stiffness. Due to the absence of many research studies regarding this parameter and its influence on the residual stress around drop-offs, these guidelines have remained conservative and can constrain composite designs [77]. In addition, it is expected that the orientation of surrounding core- and belt plies have an influence as well. Therefore, the influence of the aspect ratio and ply orientation on the cure-induced residual stress are investigated together.

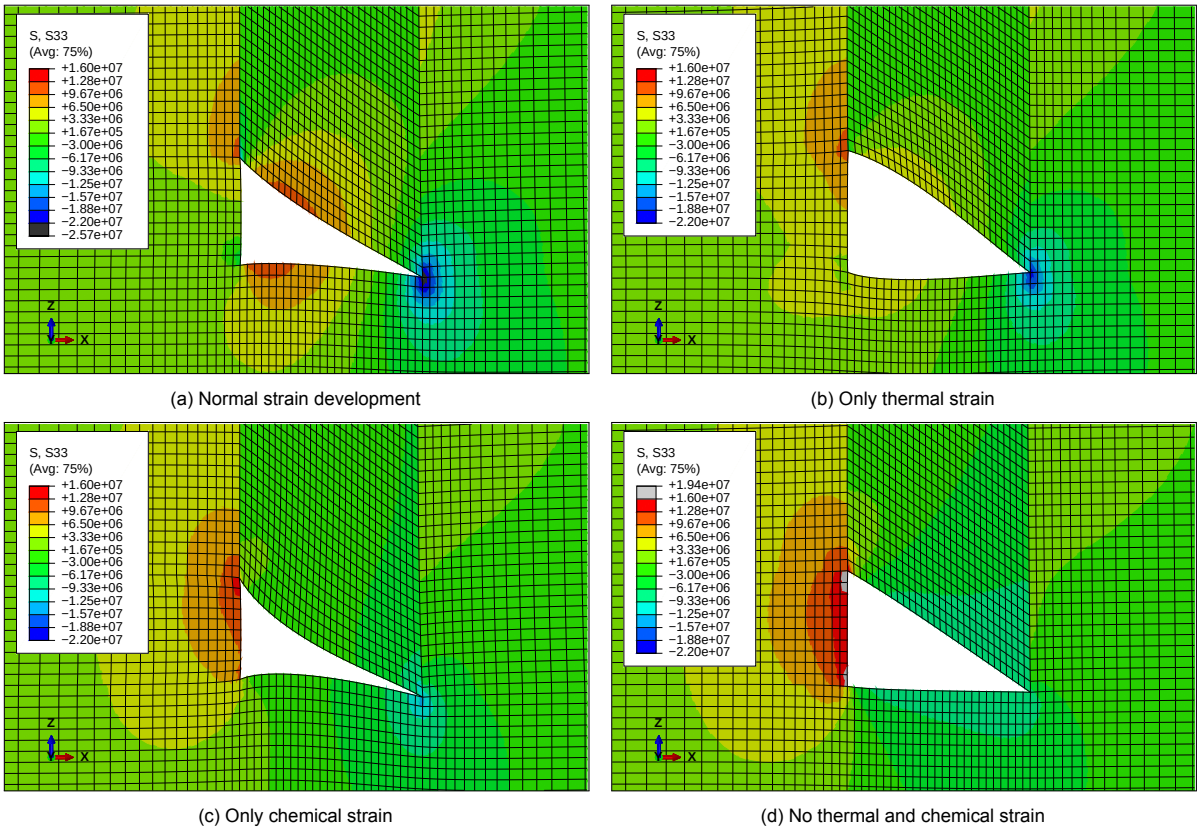

(a) Normal strain development

(b) Only thermal strain

(c) Only chemical strain

(d) No thermal and chemical strain

Figure 5.4: Out-of-plane stress contour plot as result of material property evolutions within resin pocket. Thin laminate ply drop-off model (a/b = 1/1.5). Time = 490 min (End cycle), DOC = 0.92. For clarification a deformation scale factor of 10 is used and the resin pocket is hidden. Unit of contour limit values in Pascal

5.2.1. Methodology of Analysis

For this analysis the thin laminate ply drop-off model is used, in which variations of the aspect ratio and ply orientation are implemented to asses their individual influence and their combined influence on the residual stress. The proposed variations of both parameters are given in table 5.2. Regarding the output result, the maximum out-of-plane direct tensile stress component located within either the core- or belt ply is analysed.

Table 5.2: Variation range of aspect ratio and ply layup orientation - Influence of resin pocket geometry and ply orientation

Parameter	Variation
Aspect ratio	$\left[\frac{1}{1.5}, \frac{1}{3}, \frac{1}{6}, \frac{1}{12}, \frac{1}{24}\right]$
Laminate layup	$[0_4/0_{1D}/0_4]$, $[\pm 30_2/0_{1D}/\mp 30_2]$, $[\pm 45_2/0_{1D}/\mp 45_2]$, $[90_4/0_{1D}/90_4]$ $[0_4/90_{1D}/0_4]$, $[\pm 30_2/90_{1D}/\mp 30_2]$, $[\pm 45_2/90_{1D}/\mp 45_2]$, $[90_4/90_{1D}/90_4]$

5.2.2. Results and Discussion

Using the five different aspect ratio values and the eight laminate layups, multiple maximum out-of-plane stress values can be extracted. Only the layups based on combinations of 0° and 90° plies are used for the influence of the aspect ratio as these result in the least- and most severe stress levels. The corresponding graph is shown in figure 5.5. Since the maximum stress can occur within the core- or belt ply, the location of the stress concentration is visualized using different data point markers. Note that in the graph on the x-axis the inverse of the aspect ratio is plotted (1/aspect ratio). The results regarding the eight different layups for each aspect ratio are divided over two graphs depicted by figure 5.6 and figure 5.7, which represent the layups with 0° and 90° orientation for the terminated ply, respectively.

When observing the graphs for each layup within figure 5.5, it can directly be concluded that for larger aspect ratios the out-of-plane stress increases. In addition, by analysing the declining curvature for all graphs, which becomes almost horizontal between lower aspect ratio values of 1/12 and 1/24 for layups $[90_4/90_{1D}/90_4]$ and $[90_4/0_{1D}/90_4]$, it suggests that with aspect ratios being below 1/12 the difference in residual stress becomes almost negligible.

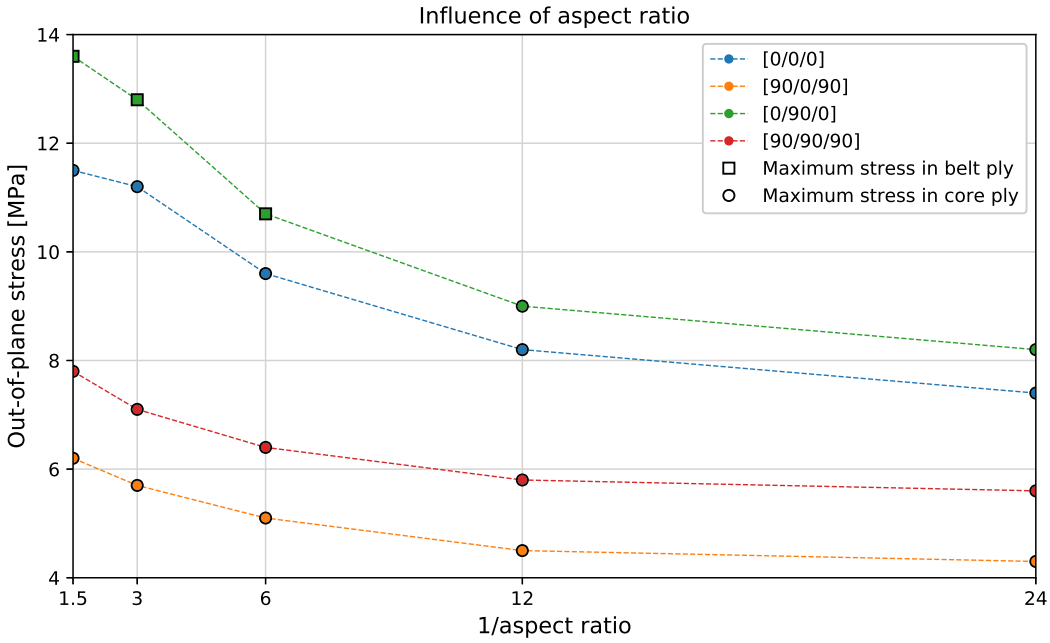

Figure 5.5: Influence of aspect ratio on the maximum out-of-plane tensile stress within core- and belt ply

Another important observation is the shift to higher stress values for the layups in which the 0° ply orientation is used for the core- and belt ply. This increase in stress can be explained by the higher in-plane stiffness of these plies in the global x-direction, which is the direction along the plies that span over the resin pocket region. Higher in-plane stiffness increases the resistance in deformation in out-of-plane direction of the surrounding plies against the resin pocket shrinkage. This results in an increase of the residual stress within the 0° plies. This effect can be substantiated by analysing both figures 5.6 and 5.7. Within these graphs, the decreasing maximum out-of-plane stress for decreasing in-plane stiffness (from 0° to 90°) of the core- and belt ply is confirmed by the decreasing linear trend for all aspect ratio curves.

Another influencing effect that can be identified is the orientation of the terminated ply. Due to the differences in in-plane chemical shrinkage and thermal contraction between the terminated ply and surrounding plies, internal stress builds up within the terminated ply. This effect can be observed within figure 5.8a, where the relatively higher in-plane shrinkage and thermal contraction of the 90° terminated ply results in tensile stress along the global x-direction.

As result of this tensile stress in the 90° ply, counteracting compressive stress regions above and below the terminated ply and around the resin pocket arise while a tensile stress region is induced at the oblique belt ply region. This tensile stress region within the belt ply influences the maximum out-of-plane stress at this location by increasing it. This effect can be observed whenever the terminated ply exhibits relatively larger in-plane chemical shrinkage and thermal contraction compared to its surrounding, where as result tensile stress is induced. This effect is the most significant for the $[0_4/90_{1D}/0_4]$ layup. The opposite effect occurs for the $[90_4/0_{1D}/90_4]$ layup, where significant compressive stress levels are induced within the terminated ply resulting in a decrease of maximum out-of-plane stress at the oblique belt ply region. Overall, this effect weakens for lower aspect ratios, which justifies the shift of location of the maximum out-of-plane stress from the belt ply to the core ply, as indicated by the markers within figure 5.5. In addition, this effect is more detrimental whenever a 90° terminated ply is used,

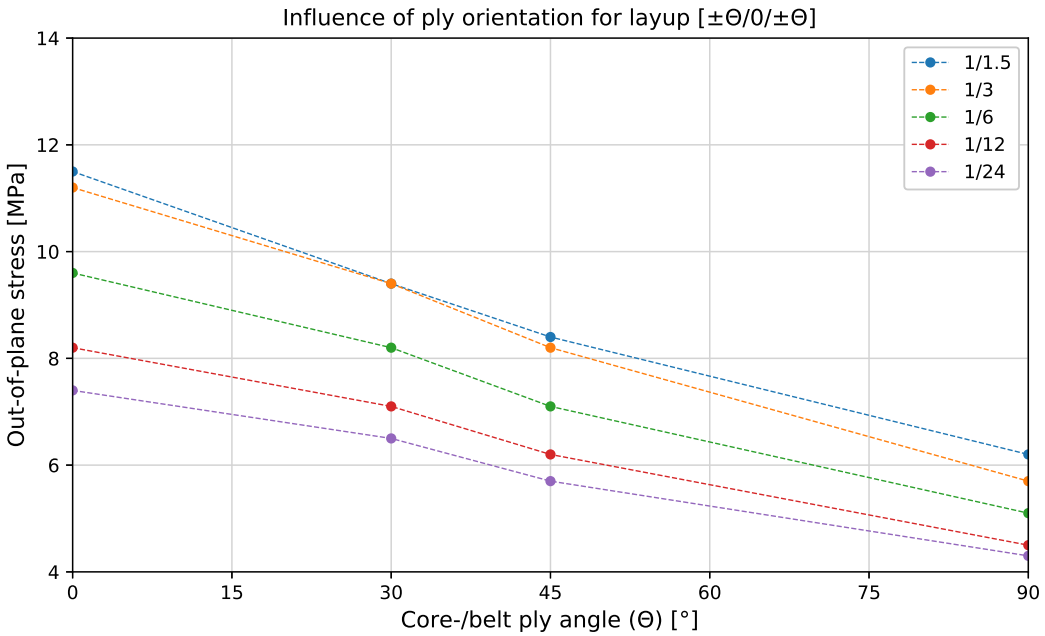

Figure 5.6: Influence of ply orientation on the maximum out-of-plane tensile stress within core- and belt ply. Layups with 0° terminated ply orientation

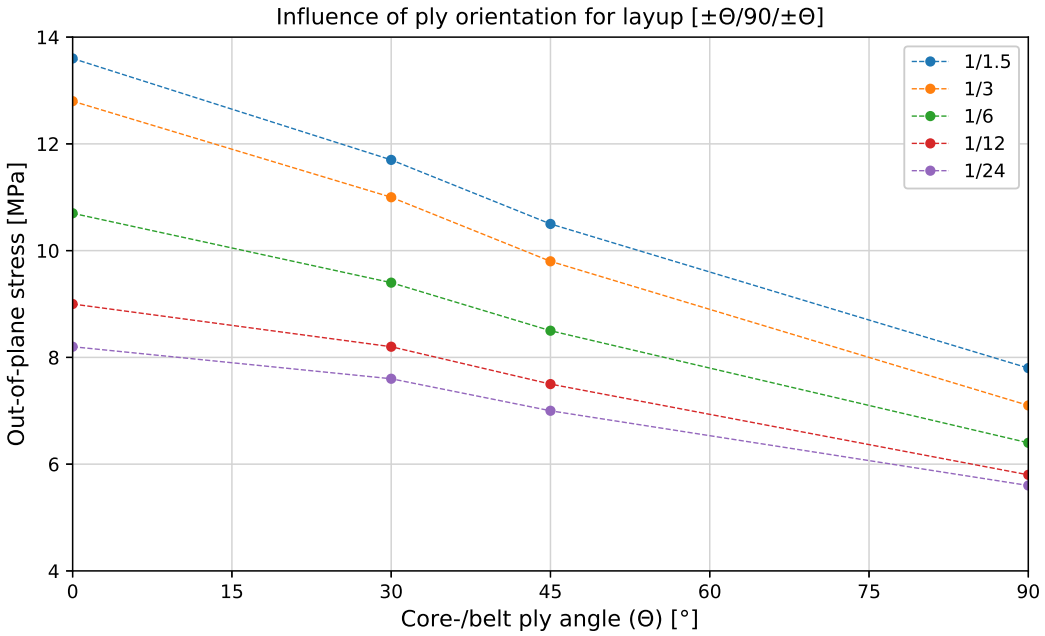

Figure 5.7: Influence of ply orientation on the maximum out-of-plane tensile stress within core- and belt ply. Layups with 90° terminated ply orientation

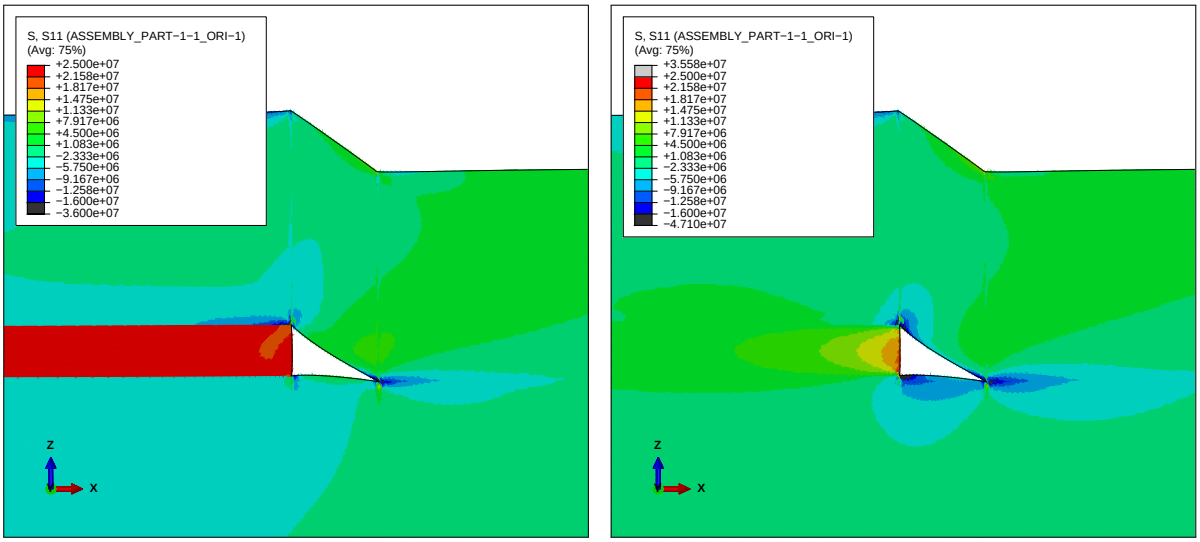

(a) Layup $[0_4/90_{1D}/0_4]$ (b) Layup $[0_4/0_{1D}/0_4]$

Figure 5.8: Contour plots of final in-plane stress in global x-direction. Thin laminate ply drop-off model with aspect ratio of 1/1.5. Resin pocket is hidden for clarification. Unit of contour limit values in Pascal

which is substantiated by the difference in absolute value in out-of-plane stress whenever a 0° instead of a 90° terminated ply is used, when comparing figures 5.6 and 5.7, respectively. This conclusion holds up for $\pm$30° and $\pm$45° ply orientations for the core- and belt ply as well

The influencing effect of local compressive stress regions for equally oriented terminated ply and core-/belt ply can be observed within figure 5.8b. For this layup, the significant difference in in-plane stress between terminated ply and its surroundings is absent because all plies have equal response in shrinkage and thermal contraction. This results in a different stress distribution within the terminated ply and an increase in compressive stress regions around the resin pocket within the core- and belt ply. As result of these compressive stress regions, the maximum out-of-plane tensile stress at these locations, which is induced by the shrinkage and thermal contraction of the pocket, is decreased by lowering the resistance to deform towards the pocket.

The final observation is the converging trend off all five aspect ratio curves within figures 5.6 and 5.7 when changing the core- and belt ply orientation from 0° to 90°. This converging trend implies that the effect of an increased out-of-plane stress within the core- and belt ply for larger aspect ratios is less significant whenever the stiffness of these plies in the direction of the drop-off is decreased.

Note that within the contour plots in figure 5.8 all stress values are transformed to the global coordinate system. This results in the contour stress values within the oblique part of the drop-off section being underestimated, as the real in-plane direction is along the oblique fibre direction.

5.2.3. Concluding Remarks

The influence of the aspect ratio can be described by the increase in out-of-plane stress with increasing aspect ratios in a non-linear manner: the decrease in stress levels flattens out at lower aspect ratios. Significantly higher stress values can occur when the orientation of the core- and belt ply is 0° due to an increase of in-plane stiffness in the direction of the drop-off. In addition, the in-plane stress within the terminated ply can influence the maximum out-of-plane stress at the core- and belt ply as well by increasing or decreasing it, dependent on whether the terminated ply is loaded in tensile- or compressive stress, respectively.

5.3. Influence of Thickness Increase

As result of the increase of the laminate thickness, multiple changes are observed regarding the internal effect on the laminate and the residual stress evolution around the drop-off region. Within this section, the most important effects due to these changes are discussed.

The temperature history data of the thick laminate model showed a maximum temperature gradient between the bottom and top surface of about 8 °C. An overshoot in temperature at the top surface as result of the exothermic reaction of about 5 °C at most occurred at the start of the dwell. As can be seen in figure 5.9, the most significant temperature gradients are present between the bottom surface and centre region of the laminate. The influence of the through-thickness cure evolution on the residual stress around the drop-off region resulting from these temperature gradients is expected to be minimal.

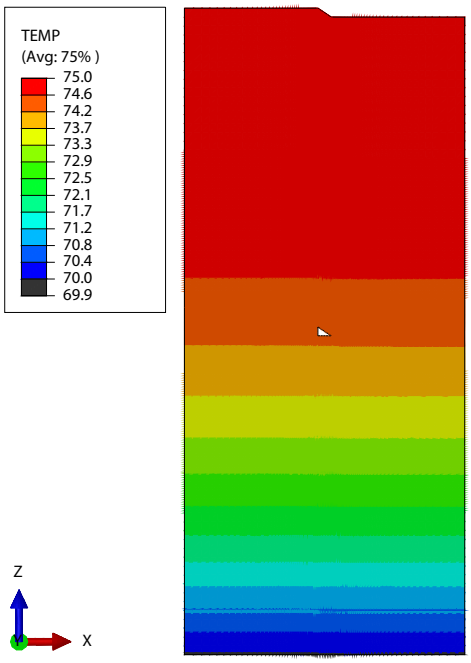

Figure 5.9: Temperature gradient at start of the dwell - Thick laminate model. Unit of contour limit values in degrees Celsius

An increase in the residual stress levels can be observed as well. Within table 5.3, both the maximum out-of-plane tensile stress within the core ply and Von Mises stress within the resin pocket are presented. As can be seen, both stress levels increase about 10% with the implementation of the thick laminate. This is caused by the aforementioned influence of the induced in-plane stress levels within the terminated ply, as relatively higher compressive stress levels within this ply can be observed for the thin laminate compared to the thick laminate. This difference originates from the layup variety through-thickness, where for the thin laminate this is based on a single 0° ply enclosed by eight 45° plies, where for the thick laminate it is more evenly distributed. For the latter, this results in lower compressive stress levels within the terminated ply as the surrounding 0° plies above and below the 45° plies provide additional in-plane resistance against the higher shrinkage and thermal contraction of the 45° plies. As effect, lower compressive stress levels are induced within the terminated ply for the thick laminate. Since section 5.2 concluded that compressive stress regions within the terminated ply decrease the maximum out-of-plane stress within core- and belt ply, this explains the higher out-of-plane tensile stress and Von Mises stress within the core ply and resin pocket for the thick laminate, respectively.

Table 5.3: Change in final maximum out-of-plane tensile and Von Mises stress [MPa] - Influence of thickness increase

Model	σ_{33} (Core ply)	σ_v (Right corner pocket)	Layup
Thin laminate	8.4	23.9[1]	$[\pm 45_2/0_{1D}/\mp 45_2]$
Thick laminate	9.3	26.3	$[(\pm 45/0_3/90)_{3s}/0_{1D}/(\pm 45/0_3/90)_{3s}]$

[1]The maximum Von Mises stress for the thin laminate, which is 25.6 MPa, is in fact located at the rear top-left corner of the pocket as result of the -45° orientation for the core-/belt plies and the overall layup as described above. To achieve the most

5.3.1. Concluding Remarks

By increasing the laminate thickness, temperature gradients through thickness can be observed with a maximum overshoot of 5 °C relative the mould surface. The cure-induced residual stress within the ply drop-off region increased by 10% for the thick laminate, which is caused by the lower in-plane compressive stress within the terminated ply compared to the thin laminate, resulting from the more evenly distributed layup around the drop-off.

5.4. Influence of Process Parameters

Within this section multiple process parameters are analysed regarding the influence on the residual stress around ply drop-off regions.

5.4.1. Methodology of Analysis

Since the results of section 5.3 showed that significant temperature gradients through-thickness can occur as result of the cure phase, for this analysis the thick laminate ply drop-off model is used. Section 5.1 showed that cure-induced stress mainly arises during the dwell- and cool down stage, which is caused by the combination of the resin modulus development, and the chemical shrinkage and thermal contraction of predominantly the pocket and surrounding plies. Therefore, the dwell temperature and cool down rate are selected as target parameters for this process parameter analysis.

Different values for each process parameter are selected, which are presented in table 5.4. The variation of the dwell temperature is selected as such that the first and second value are respectively lower and higher than the MRCC of 70 °C. The third and highest dwell temperature variation of 100 °C is selected deliberately as it is higher than the theoretical maximum Tg of the resin material. This may have influence on the residual stress generation throughout the cure cycle as vitrification effects do not occur during the dwell stage. The lowest cool down rate is selected lower than the recommended cool down rate in the MRCC but not too low that process times become too long. The second rate is selected to be higher than the MRCC but still in the same order of magnitude, whilst the highest rate is significantly higher compared to the MRCC. For each cure cycle a heating rate of 0.3 °C/min is implemented combined with maximum dwell time of 4h, which are both according to the MRCC.

Table 5.4: Process parameter variation - Influence of process parameters

Process parameter	Variation	Unit
Dwell temperature	[60, 80, 100]	[°C]
Cool down rate	[0.1, 0.5, 1.5]	[°C/min]

As described within sections 2.3 and 3.4, the residual stress is influenced by the DOC evolution via the resin modulus development. To conduct the most legitimate comparison regarding the influencing process parameters between each cycle, an about equal final DOC value at the end of each cycle is considered. Therefore, a maximum allowed DOC check is implemented within the UMAT subroutine of the neat resin material, which is only assigned to the resin pocket region. This restriction implies that the dwell stage ends whenever either the maximum dwell time or DOC threshold within the pocket is reached, after which the cool down stage initiates. Note that this restriction only ensures a maximum DOC value at the end of the dwell stage, while lower DOC values can still occur whenever the maximum dwell time is reached first. For the maximum DOC, a value of 0.92 is selected as minimum threshold at which sufficient quality of the laminate has been reached.

The maximum out-of-plane direct tensile stress located within the core ply is used to analyse the influence of the process parameters. In addition, the Von Mises stress within the resin pocket is analysed, which is observed to be the most critical at the rear right corner where both the core- and belt ply come together, as depicted by figure 5.10. This location results from both the +45° core- and belt ply below and above the resin pocket. Because this corner is aligned with the fibre direction of these plies, resistance against the chemical shrinkage and thermal contraction of the resin pocket is the most significant at this location.

objective comparison, the maximum Von Mises stress for the thin laminate is obtained at the same location as within the thick laminate, i.e. the rear right corner of the resin pocket, as shown in figure 5.10

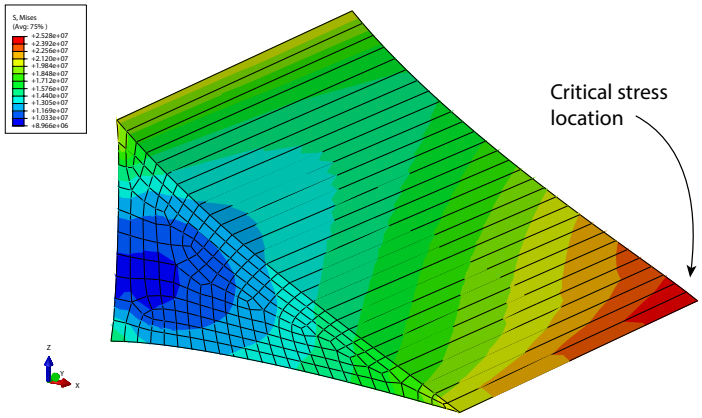

Figure 5.10: Maximum Von Mises stress location within resin pocket. Cure cycle with dwell temperature of 60 °C and 0.1 °C/min cool down rate. For clarification a deformation scale factor of 10 is used. Unit of contour limit values in Pascal

5.4.2. Results and Discussion

Due to the DOC threshold check, different dwell times resulted for each dwell temperature. For the 60 °C cycles, only a maximum DOC value of 0.90 is achieved within the available dwell time. The dwell stage for the 80 °C cycles aborted after only 67 min whereafter the cool down stage initiates. For the 100 °C cycles, the dwell temperature is not reached due to the exceeding of the DOC threshold at a temperature of 92 °C during the heating stage. In table 5.5, the final DOC values, maximum out-of-plane stress within the core ply and maximum Von Mises stress within the resin pocket are given. Within appendix G, for each dwell temperature the output graphs for a single different cool down rate are given. In the following sections, the most important findings from this process influence analysis are discussed.

Table 5.5: Final DOC of pocket, and maximum out-of-plane and Von Mises stress values - Process influence analysis

	60 °C dwell			80 °C dwell			100 °C dwell		
Cool down rate	α [-]	σ_{33} [MPa]	σ_v [MPa]	α [-]	σ_{33} [MPa]	σ_v [MPa]	α [-]	σ_{33} [MPa]	σ_v [MPa]
0.1 °C/min	0.90	8.3	22.7	0.93	9.1	25.5	0.95	9.6	27.2
0.5 °C/min	0.89	8.0	21.7	0.93	8.8	24.4	0.93	9.2	25.6
1.5 °C/min	0.89	7.7	20.8	0.92	8.5	23.5	0.93	8.9	24.7

Influence of Dwell Temperature

The moment at which stress starts to develop is different for lower dwell temperatures. In figure 5.11, the out-of-plane stress evolution within the core ply for all cure cycles is illustrated. Equal trends but different absolute values for the Von Mises stress evolution within the resin pocket can be observed, for which the graph is included in appendix G. Within the graph for the out-of-plane stress evolution, for each of the three dwell temperatures the start of the cool down stage is marked by red circles. As can be seen for the 60 °C cycles, prior to the cool down stage an already significant stress evolution has taken place during the dwell. For both the 80 °C and 100 °C cycles, this stress evolution during the dwell cannot be observed and only becomes significant from upon the cool down stage. Because stress development is already significant earlier in the cure phase, the final residual stress values are lower compared to the 80 °C and 100 °C cycles.

Using the temperature and Tg evolution graph for the 60 °C cycle with the 1.5 °C/min cool down rate, depicted by figure 5.12, multiple observations can be done. As result of heating of the laminate, a temperature overshoot caused by the exothermic reaction of the polymerisation of the resin can be observed. Only minor differences in temperature between the centre region (resin pocket) and top surface region are present. The laminate cure evolves from top to bottom and the largest temperature gradients are mainly present within the lower half of the laminate. This temperature overshoot can be

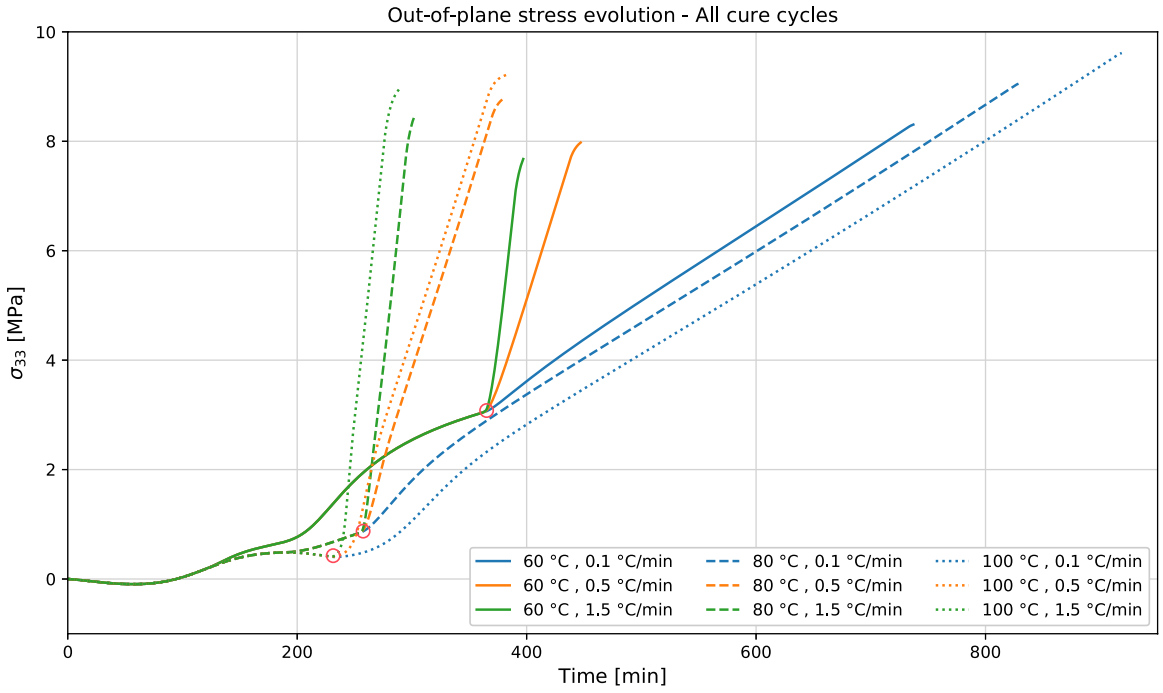

Figure 5.11: Overall out-of-plane stress evolution within core-/belt ply. All dwell temperatures and cool down rates

observed for the cure cycles with dwell temperatures of 80 and 100 °C as well. However, for these cycles the overshoot only occurs during the heating stage and flattens out before the start of the dwell stage.

Within the same graph, the vitrification point of the resin pocket can be identified directly at the start of the cool down stage while significant modulus development already occurs from halfway through the dwell stage (225 min). This development can be observed within figure 5.13 and is caused by the Tg which approaches the dwell temperature within about 10 °C difference. According to Struzziero et al. [48], within this range the resin starts vitrifying and residual stress can develop. This increase of residual stress in both the core ply and resin pocket during the dwell are a direct result of the chemical shrinkage of the resin and the modulus development, as temperature remains stable during this stage. After the vitrification point and during the cool down stage, stress continues to increase linearly which is caused by the thermal contraction due to temperature decrease.

When comparing the DOC- and stress results in table 5.5 for different dwell temperatures, it can be suggested that the stress values are mainly affected by the final DOC values and that a direct influence of the dwell temperature is absent. Using figure 5.14, the influence of the DOC can be analysed to examine whether a combined effect of the final DOC and dwell temperature is present. When comparing the stress development for the 80 °C, 0.1 °C/min cycle and 100 °C, 0.5 °C/min cycle, it can be concluded that although different stress evolution trends at the initial development stage can be identified, both stress levels stabilise at almost identical final values. This implies that the stress development is mainly influenced by the final DOC value and that a direct influence of the dwell temperature, or a combined effect of both, cannot be identified. Similar trends for the Von Mises stress evolution within the resin pocket can be observed, for which the graph is included in appendix G.

Influence of Cool Down Rate

The stress values within table 5.5 indicate that an increase in cool down rate decreases residual stress development. This effect can be observed by comparing the stress evolutions for different cool down rates per dwell temperature within figure 5.11. From upon the red markers where the cool down stage initiates, the residual stress increases more rapidly but the final stress levels are lower. This effect can be related to the vitrification point of the resin pocket, which is different for each cool down rate. As can be seen in figure 5.15a, the vitrification point resulting from each dwell temperature is postponed

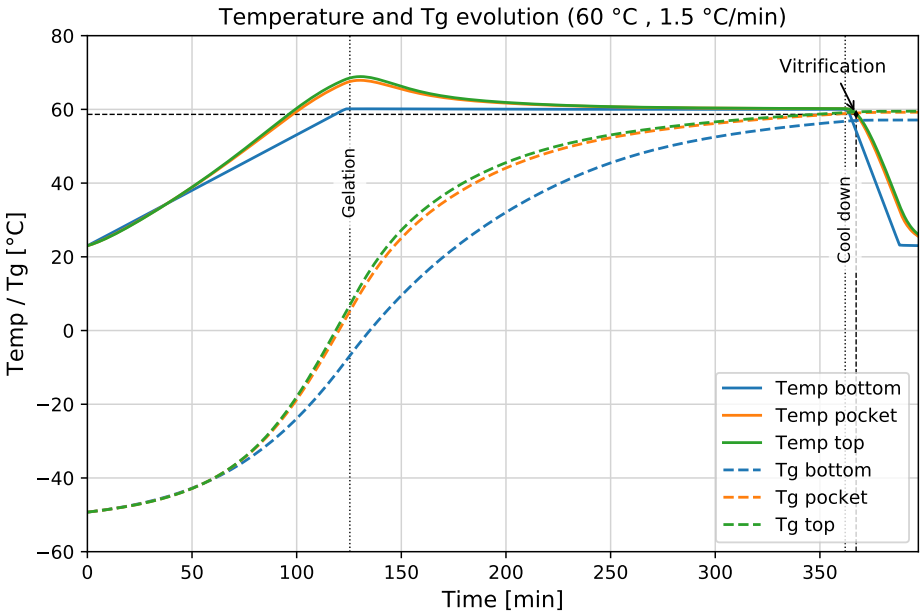

Figure 5.12: Temperature and Tg evolution graph. Dwell temp: 60 °C, cool down rate: 1.5 °C/min

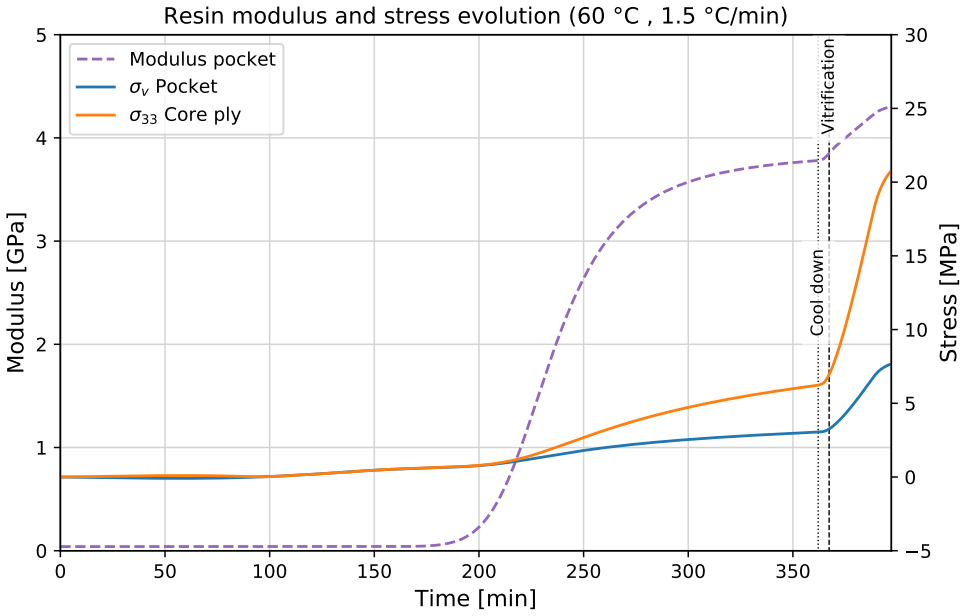

Figure 5.13: Modulus and stress evolution graph. Dwell temp: 60 °C, cool down rate: 1.5 °C/min

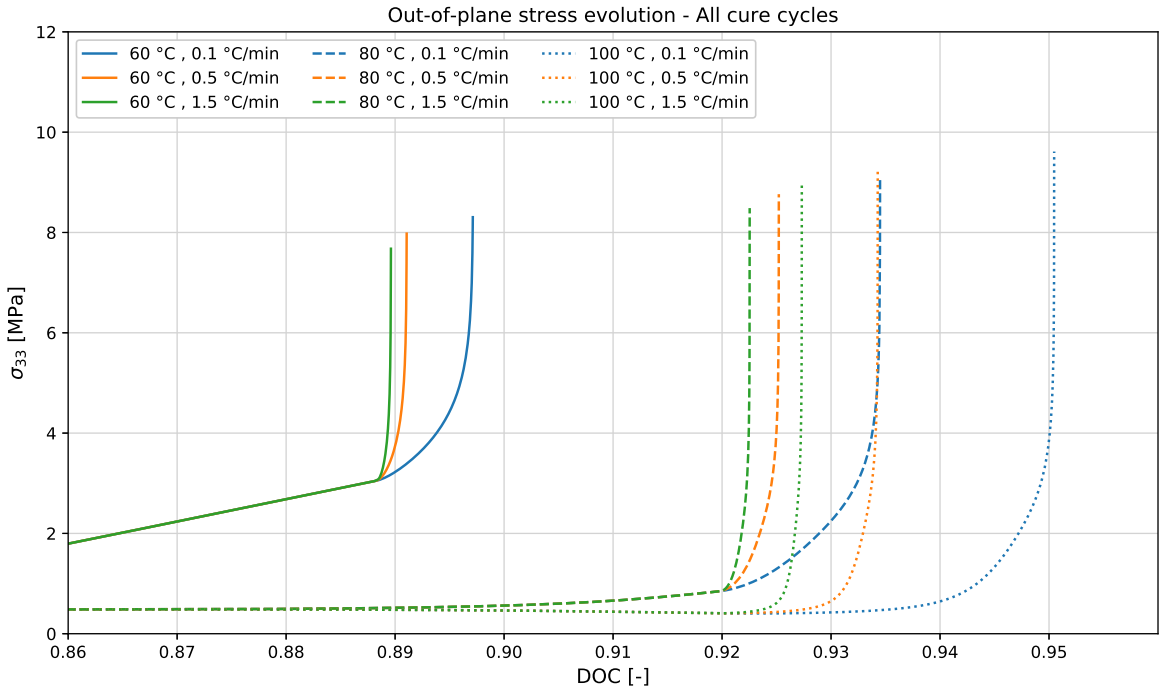

Figure 5.14: Overall out-of-plane stress evolution within core-belt ply vs. DOC. All dwell temperatures and cool down rates

to lower values with increased cool down rates. Since stress levels at this point per dwell temperature are about equal for all cool down rates, this lower vitrification temperature results in a decrease of the effective thermal contraction in glassy state throughout the cool down stage. This effect is visualized by figure 5.15b, where lower vitrification points result in a decrease in final stress values.

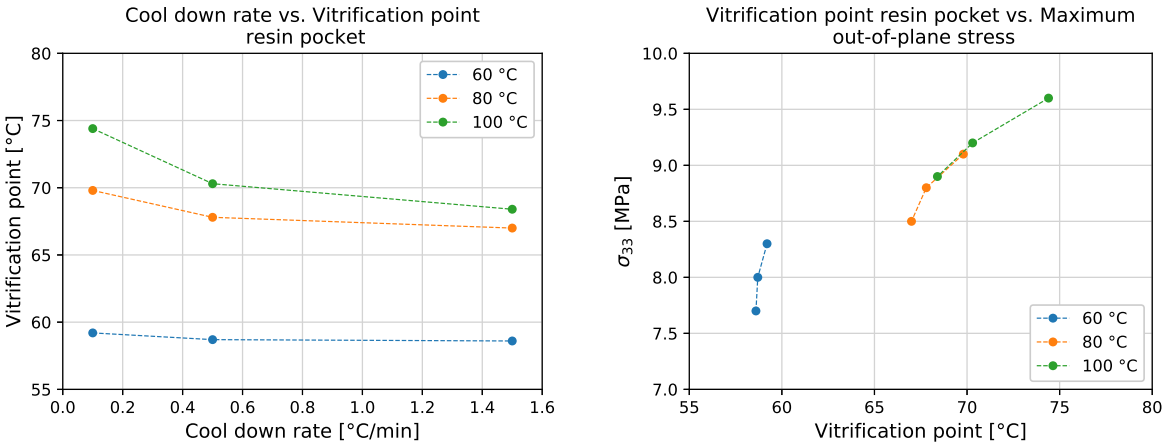

(a) Cool down rate vs. Vitrification point

(b) Vitrification point vs. Maximum out-of-plane stress

Figure 5.15: Influence of cool down rate on vitrification point and maximum out-of-plane stress

These observations suggest that cool down rates can be increased to reduce residual stress development, up to the practical limits of RTM equipment and tooling. Also, additional problems can arise for laminates with larger thickness, such as large temperature gradients during cooling. These may influence the stress development throughout the cool down stage and introduce additional limitations to the maximum feasible cool down rate.

For the 80 and 100 °C cycles, virtually all stress development occurs during the cool down stage, because the dwell temperatures are higher than the maximum reached Tg, which is about 68 °C and

71 °C, respectively. As result, resin vitrification and modulus development only becomes significant during the first part of the cool down stage, which can be observed within figure 5.16. Because the DOC development stabilises at the start of the cool down, the residual stress development is only caused by the thermal contraction of the resin combined with the modulus development as result of the temperature decrease. This effect is depicted by figure 5.17, in which the stress increases linearly from upon the start of the cool down stage. The same effect can be observed for the 100 °C cycles, for which an example is included within appendix G.

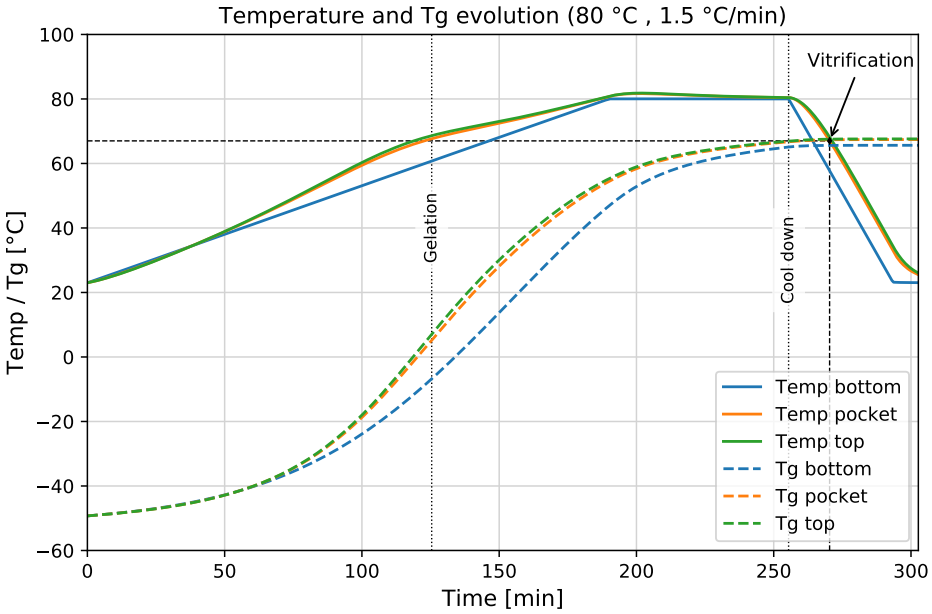

Figure 5.16: Temperature and Tg evolution graph. Dwell temp: 80 °C, cool down rate: 1.5 °C/min

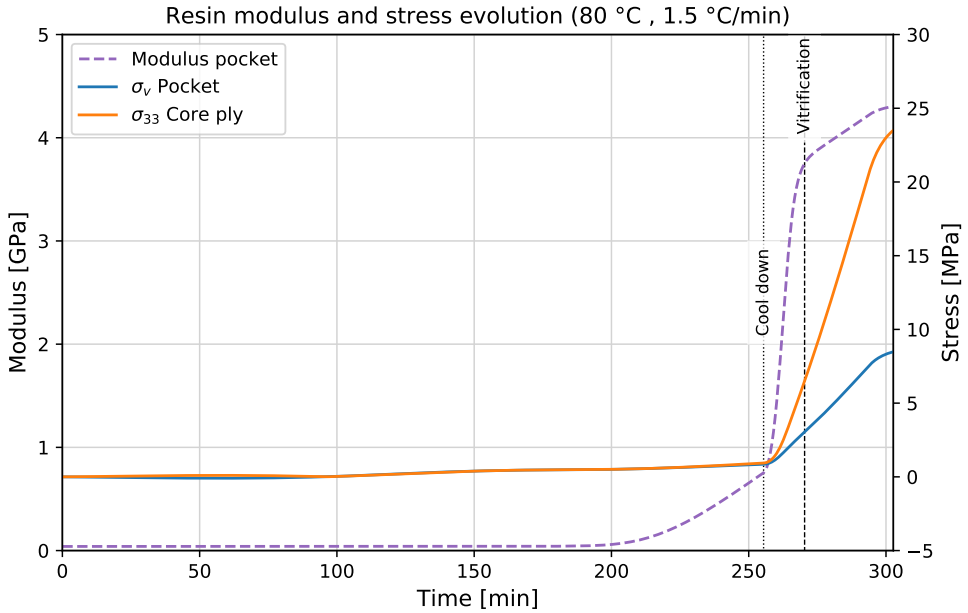

Figure 5.17: Modulus and stress evolution graph. Dwell temp: 80 °C, cool down rate: 1.5 °C/min

5.4.3. Concluding Remarks

From the process influence analysis, it can be concluded that lower dwell temperatures lower the residual stress development and changing the moment where significant stress starts to build up. The latter effect results from the Tg which approaches the dwell temperature during the dwell stage, causing the resin modulus and stress levels to become significant prior to vitrification. No considerable direct influence can be identified between the dwell temperature and stress generation other than via the DOC values, where higher dwell temperatures result in higher final DOC which subsequently increase the final stress levels. Regarding the influence of the cool down rate, an increase of this parameter results in a more rapidly, but lower final stress build-up. This effect originates from the vitrification point, which is postponed to lower temperatures with increased cool down rates, resulting in lower stress development arising from thermal contraction in the glassy state of the resin.

5.5. Conclusions

From this chapter multiple important elements can be identified which are essential for ply drop-off implementation. It was found that the influence of the aspect ratio, defining the pocket geometry, becomes almost negligible whenever this ratio is decreased from 1/12 to 1/24 for layups including 90° orientation for core- and belt plies. This implies that whenever for a given ply drop-off, where due to the in-plane stiffness of the covering belt-ply the aspect ratio becomes around 1/24, potentially more than a single ply can be terminated without resulting in significant out-of-plane stress increases. This is an important consideration as potentially this may require less ply drop-offs within laminates to achieve the required thickness transition.

According to the ply drop-off guidelines from section 2.5.1, it is recommended to first terminate the ply with the highest in-plane stiffness in drop-off direction, i.e. the 0° ply. This rule is in line with the observed influence of the terminated ply orientation from section 5.2, as dropping a 0° ply surrounded by plies with equal- but preferably lower in-plane stiffness results in an in-plane compressive stress region within the terminated ply. This region is advantageous as it decreases the maximum out-of-plane stress at the drop-off region.

Process parameters can be used to lower the final residual stress levels around drop-off regions. By selecting the dwell temperature as such that the Tg can approach this value during the dwell stage, an already significant resin modulus can be achieved during this stage. As result, stress levels become significant prior to vitrification for which it is observed that this early stress development can result in lower final stress levels after vitrification during the cool down stage. In addition, the final stress levels are influenced by the final DOC values as well. Considering these observations, it is essential to select the dwell temperature high enough to obtain a minimal required DOC within the available process time, but not higher than 5-10 °C above the Tg value achievable in practice, so stress generation already takes place during the dwell. Note that his Tg value is not equivalent to the $T_{g\infty}$, as this value is never reached.

Besides the dwell temperature, the cool down rate can also be used to lower the final residual stress levels. As higher cool down rates postpone the vitrification point and therefore decrease the significant stress built-up in the glassy state of the resin, this rate can potentially be selected higher than prescribed by the MRCC. Naturally, this cool down rate is limited to a some extent by the practical limits of the process equipment. In addition, increasing cool down rates may induce significant through-thickness temperature gradients which can introduce additional problems regarding stress generation and laminate distortions, which therefore must be considered.

6

Cure-Induced Residual Stress and Interactions of Multiple Ply Drop-Off regions

This chapter is dedicated to the analysis regarding the influence of multiple ply drop-off regions on the residual stress. In section 6.1, the influence of the multiple drop-off implementation, the stagger distance and stress interactions introduced by different ply orientations are investigated. This chapter is ended with the conclusions in section 6.2.

6.1. Influence of Stagger Distance

As described within chapter 2, the stagger distance is often selected using conservative guidelines, where the lower bound originates from the prevention of large stress concentrations around the drop-off regions, while the upper bound is driven by the maximum available length of the required thickness reduction along the laminate. Within this section, the influence of the stagger distance on the cure-induced residual stress around multiple ply drop-off regions is investigated for two topologies. These topologies are based on implementing multiple drop-offs using the two most basic arrangements; a shared core- or belt ply (see section 4.3). Since the stress evolutions at these regions can introduce stress interactions between each drop-off as result of the different ply orientations, these interactions are evaluated as well.

6.1.1. Methodology of Analysis

In total three different stagger distance variations are evaluated using the multiple ply drop-off model from section 4.3: the variation range is based on 1.5B, 2B and 3B (see definition of B in section 4.3). The centre value of this variation is based on the minimum stagger distance guidelines reported by [77]. The lower- and upper bound of the variation is defined by respectively decreasing and increasing the distance by 0.5B and 1B with respect to the centre value.

The maximum out-of-plane direct tensile stress within both the core- and belt ply at each drop-off is analysed for each topology. The stress values at these locations are compared to the results of the thick laminate single drop-off model. By comparing these stress values, the influence of the multiple ply drop-off implementation and the stagger distance can be investigated. Additional simulation is performed where both the thick laminate single ply drop-off model and multiple ply drop-off models are implemented with a layup only consisting of 0° ply orientations, to evaluate the combined influence of multiple drop-offs and ply orientations, and its relation with the stagger distance.

Besides the maximum stress values, contour plots visualizing the out-of-plane and in-plane stress regions are being analysed for each topology and layup. Using these plots, the coupling effects between the in-plane stress induced by different ply orientations and their effect on the out-of-plane stress can be analysed.

6.1.2. Results and Discussion

In the following sections, both topologies and corresponding stress results are discussed individually.

Stress Results - Topology 1

Within figure 6.1, the maximum out-of-plane direct tensile stress values are plotted against the stagger distance for both the core- and belt ply separately. As can be seen in both graphs, implementing multiple ply drop-off regions within a laminate using topology 1 results overall in higher out-of-plane stress levels within both the core- and belt ply.

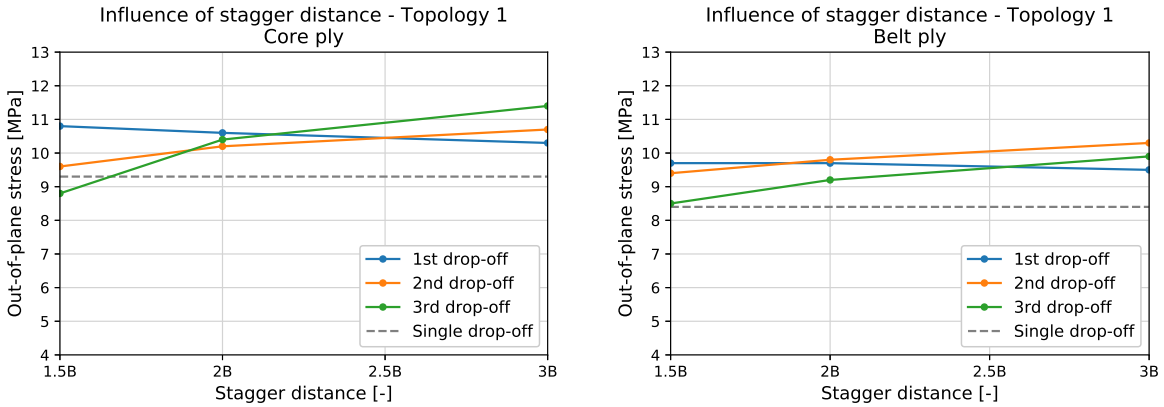

(a) Core ply

(b) Belt ply

Figure 6.1: Influence of stagger distance on maximum out-of-plane stress within core- and belt ply. Multiple ply drop-off model with aspect ratio of 1/1.5. Topology 1

Important to emphasize are the changes in stress levels around the 1st drop-off regardless the stagger distance, where the surrounding plies at this drop-off have equal orientations as the single drop-off model. This implies that the increase in stress around this 1st drop-off can only be caused by the multiple drop-off implementation. The effective difference can be observed within figure 6.2, where the out-of-plane tensile stress region below the single drop-off, depicted by figure 6.2a, is less significant compared to the stress region at the same location below the 1st drop-off, depicted by region I in figure 6.2b. This region becomes smaller with increasing stagger distance, as shown in figures 6.2c and 6.2d, causing the decreasing trend of the maximum out-of-plane stress for the 1st drop-off in figure 6.1.

Another effect which can be explained by figures 6.2b to 6.2d, is the increasing trend of the out-of-plane stress around the 3rd drop-off with increasing stagger distance. As shown in these contour plots, the significance of the compressive stress concentration at the right corner of the pocket, indicated by location II, decreases when the stagger distance increases. This decrease implies that the compressive stress levels around the region where the core- and belt ply come together, become less significant for larger stagger distances. When these compressive stress levels are lower, effectively the maximum out-of-plane stress within core- and belt ply, induced by the shrinkage and contraction of the pocket, becomes higher. This observation is substantiated by the tensile stress region, indicated by location III within figure 6.2d, which increases in size with increasing stagger distance.

In-plane Interactions - Topology 1

Within figure 6.3 the in-plane stress contour plots of both the single ply drop-off model and multiple ply drop-off model for different stagger distances is illustrated. Note that within these contour plots all stress values are transformed to the global coordinate system.

The first interaction effect which can be observed using the in-plane stress contour plots is the changing tensile stress region within the 2nd terminated ply-end, indicated by location I within figures 6.3b to 6.3d. By increasing the stagger distance, this region separates over the oblique- and straight section of the 2nd terminated ply. It is expected that this tensile stress region increases the out-of-plane stress at the

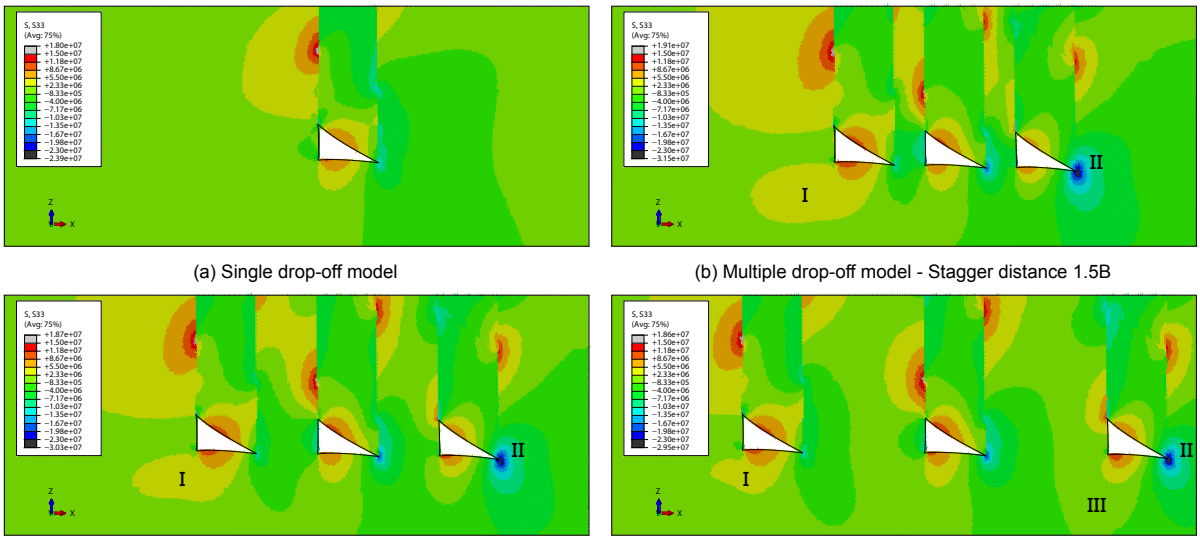

(a) Single drop-off model

(b) Multiple drop-off model - Stagger distance 1.5B

(c) Multiple drop-off model - Stagger distance 2B

(d) Multiple drop-off model - Stagger distance 3B

Figure 6.2: Contour plots of out-of-plane stress in local z-direction. Single- and multiple ply drop-off model with aspect ratio of 1/1.5 and topology 1. Resin pockets are hidden for clarification. Unit of contour limit values in Pascal. (I) Increased tensile stress region at 1st drop-off. (II) Compressive stress concentration at 3rd drop-off. (III) Increased size of tensile stress region at 3rd drop-off with increasing stagger distance

1st drop-off, which justifies the decreasing trend as shown in figure 6.1 for increasing stagger distance as this region becomes less dominant.

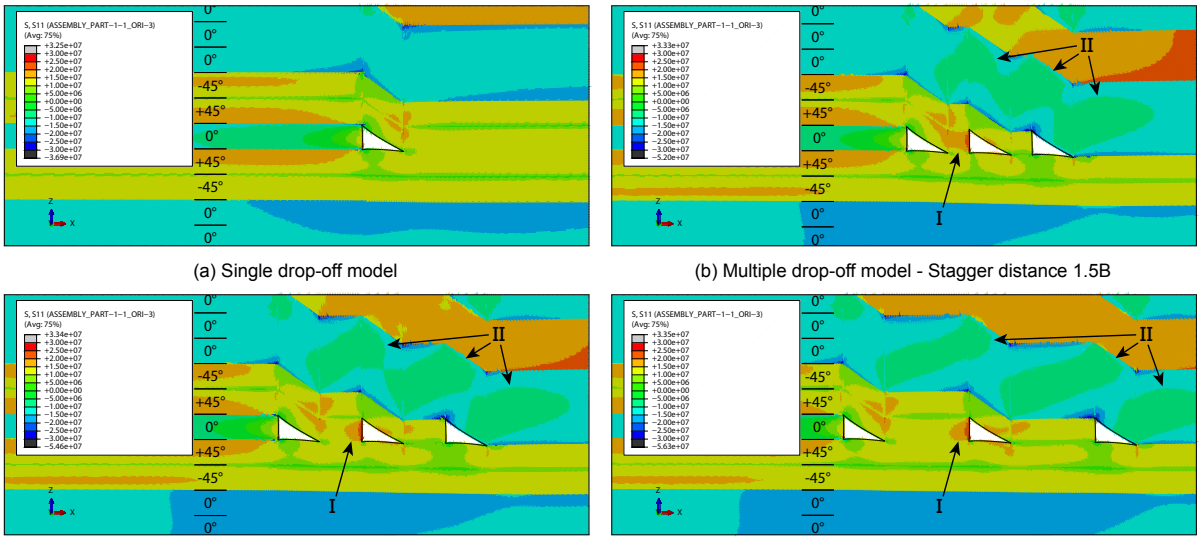

(a) Single drop-off model

(b) Multiple drop-off model - Stagger distance 1.5B

(c) Multiple drop-off model - Stagger distance 2B

(d) Multiple drop-off model - Stagger distance 3B

Figure 6.3: Contour plots of in-plane stress in global x-direction. Single- and multiple ply drop-off model with aspect ratio of 1/1.5 and topology 1. Resin pockets are hidden for clarification. Unit of contour limit values in Pascal. (I) Increased tensile stress region at 2nd terminated ply-end. (II) Lower compressive stress regions above the multiple drop-offs

An additional interaction effect is based on the three regions of lower compressive stress within the 0° plies above the multiple drop-offs, which are influenced by the stagger distance. It can be observed that these regions, indicated by location II within figures 6.3b to 6.3d, lengthen in longitudinal direction and concentrate more towards the oblique- and right edge of each pocket with increasing stagger distance, primarily for the 3rd drop-off. Due to the shift of these regions, effectively the in-plane compressive stress decreases at these locations. This effect is the origin of the decrease in significance of the out-of-plane compressive stress concentration observed within figures 6.2b to 6.2d, which causes the increase in out-of-plane tensile stress within the core- and belt ply of the 3rd drop-off with increasing

stagger distance. Similar as described in section 5.2, the in-plane compressive stress regions within the 0° plies arise from the difference in in-plane thermal contraction and chemical shrinkage with respect to its surroundings, which are 45° and 90° plies.

Stress Results - Topology 2

As can be seen within figure 6.4, similar trends of increased out-of-plane direct tensile stress with increasing stagger distance as for topology 1 can be observed for all drop-offs. One important difference is that the stress values of the 2nd and 3rd drop-off are lower compared to the induced stress for the single drop-off implementation. Both these drop-offs have similar core- and belt ply orientations as the single drop-off configuration, which implies that this decrease in stress originates from effects introduced by the multiple drop-off implementation. The stress values of both drop-offs increase with increasing stagger distance, where for the 3rd drop-off these approach the single drop-off values.

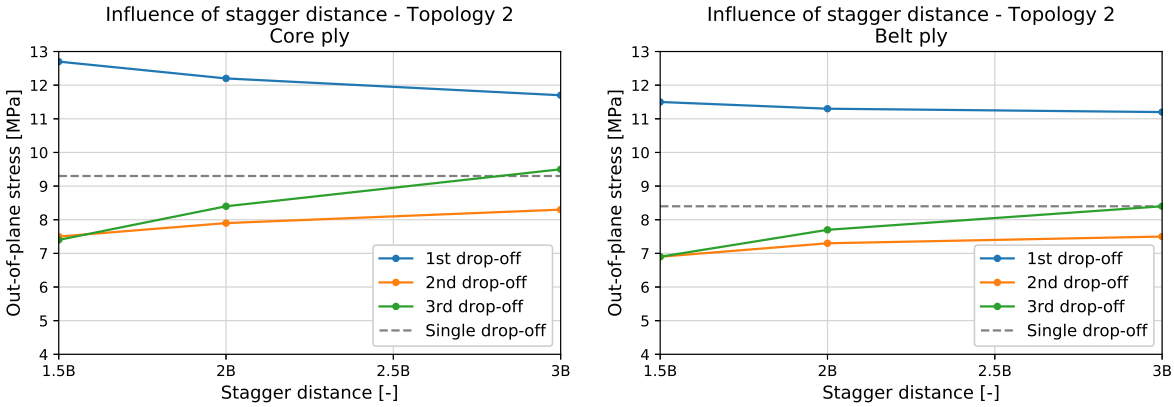

(a) Core ply

(b) Belt ply

Figure 6.4: Influence of stagger distance on maximum out-of-plane stress within core- and belt ply. Multiple ply drop-off model with aspect ratio of 1/1.5. Topology 2

Another difference is the significantly increased out-of-plane stress around the 1st drop-off, observable in figure 6.4. As shown in figure 6.4a, the stress component within the core ply of this 1st drop-off is increased to almost 13 MPa, while this stress for the single drop-off model is around 9.5 MPa. The increase of this stress for the multiple drop-off model can be explained partially by the 0° orientation of the core ply, for which it was already concluded within section 5.2 that higher in-plane stiffness of a 0° ply orientation can result in an increased out-of-plane stress at this location.

The out-of-plane stress within the belt ply at this 1st drop-off is significantly higher compared to the same ply for the single drop-off model as well, as shown in figure 6.4b. This increase can be partially justified by the increased stress within the core ply, which is expected to influence the stress at the belt ply via the resin pocket. However, as the stress within both the core- and belt change with increasing stagger distance, it is expected that the ply orientation alone is not the only origin of this increase. The increased stress levels are related to the tensile stress region below the 1st drop-off, indicated by region I in the contour plots depicted by figures 6.5b to 6.5d. As the stagger distance is increased, this region decreases which explains the decreasing trend of the out-of-plane stress at this drop-off. As can be seen in the contour plot for the single drop-off implementation, depicted by figure 6.5a, this region is still significantly smaller compared to the regions for the multiple drop-offs with different stagger distances. Therefore, it is expected that interaction effects due to the ply orientations combined with the multiple drop-off implementation influences the overall changes in out-of-plane stress.

In-plane Interactions - Topology 2

The interaction effects as result of the different ply orientations are more emphasized with this topology. The increased in-plane tensile stress region before and after the 1st resin pocket, indicated by location I in figures 6.6b to 6.6d, can be related to the significantly increased out-of-plane stress observable within the graphs of figure 6.4. Since tensile stress regions are present within both the 1st and 3rd

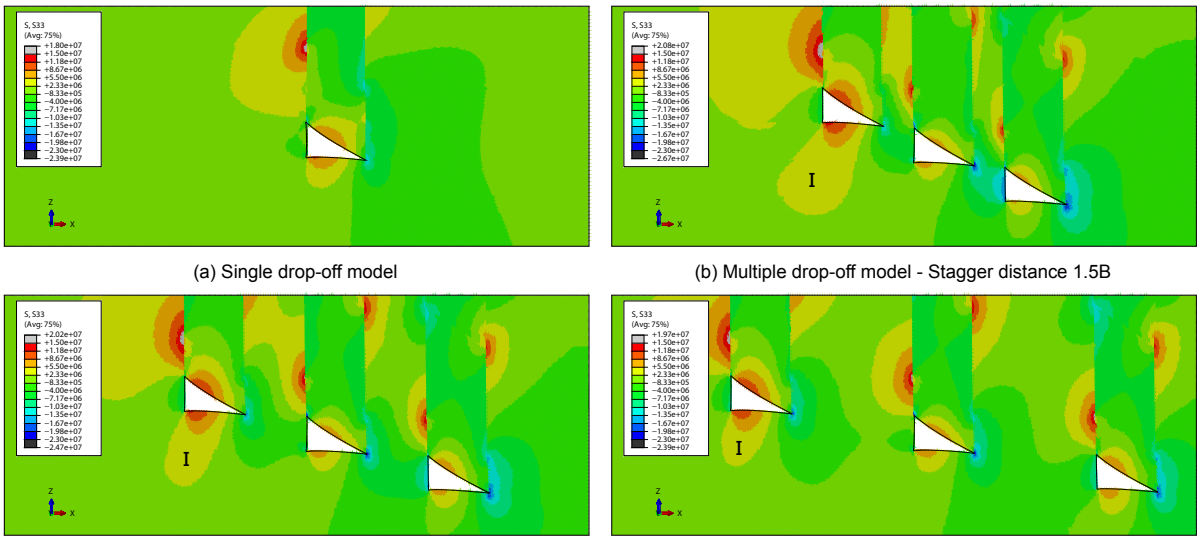

(a) Single drop-off model

(b) Multiple drop-off model - Stagger distance 1.5B

(c) Multiple drop-off model - Stagger distance 2B

(d) Multiple drop-off model - Stagger distance 3B

Figure 6.5: Contour plots of out-of-plane stress in local z-direction. Single- and multiple ply drop-off model with aspect ratio of 1/1.5 and topology 2. Resin pockets are hidden for clarification. Unit of contour limit values in Pascal. (I) Increased tensile stress region at 1st drop-off

terminated ply, location I and II respectively, it can be concluded that these are caused as counteracting effect on the induced compressive stress within the 2nd terminated ply. As this ply is 0° orientated, it encounters the same relatively lower in-plane thermal contraction and chemical shrinkage compared to its surroundings, resulting in compressive stress build up.

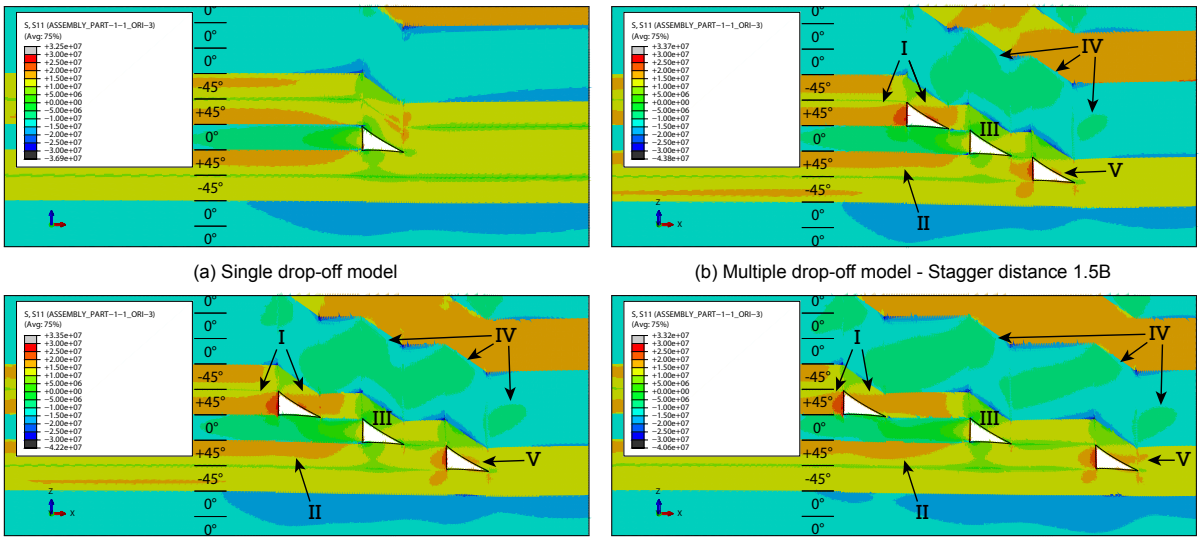

(a) Single drop-off model

(b) Multiple drop-off model - Stagger distance 1.5B

(c) Multiple drop-off model - Stagger distance 2B

(d) Multiple drop-off model - Stagger distance 3B

Figure 6.6: Contour plots of in-plane stress in global x-direction. Single- and multiple ply drop-off model with aspect ratio of 1/1.5 and topology 2. Resin pockets are hidden for clarification. Unit of contour limit values in Pascal. (I) Increased tensile stress regions before and after the 1st resin pocket. (II) Increased tensile stress region within 3rd terminated ply. (III) Stress-free region above 2nd resin pocket. (IV) Lower compressive stress regions above the multiple drop-offs. (V) Increasing tensile stress region within 3rd belt ply

Resulting from the interaction effect described above, an additional effect causes the out-of-plane tensile stress within the core- and belt ply of the 2nd drop-off to be lower compared to the single drop-off values. Since the terminated ply of the 2nd drop-off encounters the in-plane compressive stress, the corresponding resin pocket is forced between the core- and belt ply which effectively lowers the out-of-plane tensile stress within these plies. This is substantiated by the emphasized stress region above

the 2nd resin pocket, indicated by location III in figures 6.6b to 6.6d, which is about stress-free. This justifies the overall lower out-of-plane tensile stress within this core- and belt ply with increasing stagger distance, depicted by figure 6.4, as this stress-free region remains present for all stagger distances variations.

The last interaction effect resulting from the different ply orientations around the drop-off regions arises from the aforementioned compressive stress regions within the 0° plies above the multiple drop-offs, indicated by location IV in figures 6.6b to 6.6d. These relatively lower compressive stress regions lengthen in longitudinal direction where the region above the 3rd drop-off enlarges and approaches the corresponding belt ply. As result, the in-plane tensile stress within the belt ply increases at this drop-off, which is observable within the contour plot with increasing stagger distance and indicated by location V in figures 6.6b to 6.6d. This effect explains the increase in out-of-plane tensile stress around this 3rd drop-off as shown in figure 6.4.

Stress Results - All 0° Layup

From the results with only 0° ply orientation it becomes clear that even without the large in-plane stress differences and related interactions caused by the different ply orientations, the three successive drop-offs still have significant influence on the out-of-plane stress within the core- and belt ply. As can be seen in figure 6.7, where the out-of-plane stress is plotted against the stagger distance for topology 1, all stress levels converge to the single drop-off model values. This effect is expected because with increasing stagger distance, the interaction effects between the drop-offs become less dominant where each individual region approaches the single drop-off configuration. This converging trend with increasing stagger distance is similar for topology 2, for which the graph is included within appendix H.

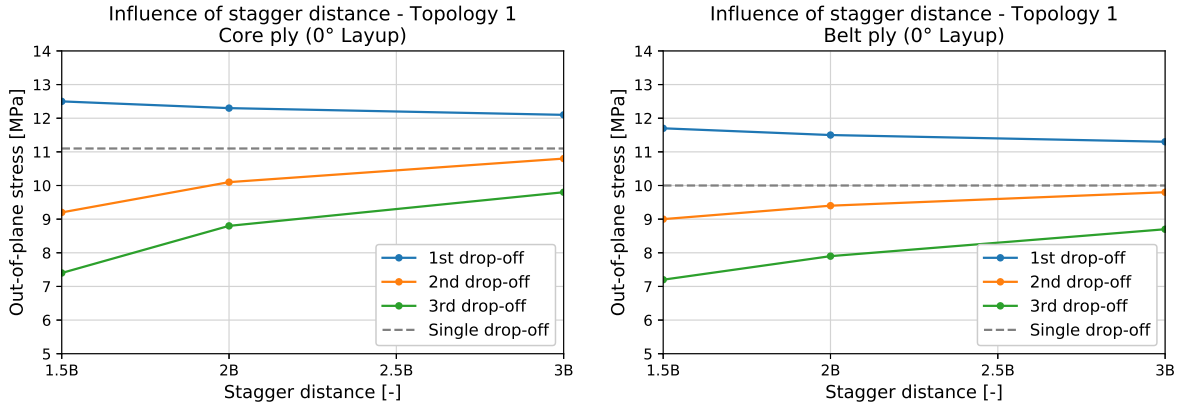

(a) Core ply

(b) Belt ply

Figure 6.7: Influence of stagger distance on maximum out-of-plane stress within core- and belt ply. Multiple ply drop-off model with aspect ratio of 1/1.5. Topology 1. All 0° layup

The origin of the increase and decrease of the out-of-plane stress within core- and belt ply can be explained by the in-plane stress contour plots as shown in figure 6.8. Within this figure, where only the contour plots for the stagger distance of 1.5B for both topologies are illustrated, can be observed that in-plane tensile stress regions are only induced at the end of each terminated ply. These stress regions are caused by the relatively higher thermal contraction and chemical shrinkage of the resin pocket. From this it can be concluded that the increase in out-of-plane stress within the 1st, and decrease in out-of-plane stress within the 2nd/3rd drop-off, is in essence caused by interaction effects of the induced stress between the multiple drop-off regions. With the implementation of different ply orientations around multiple drop-off regions, stress levels are influenced and changed in magnitude depending on which terminated- and surrounding plies are loaded in tensile- or compressive stress. This influencing effect becomes less substantial whenever the stagger distance between the multiple drop-offs is increased.

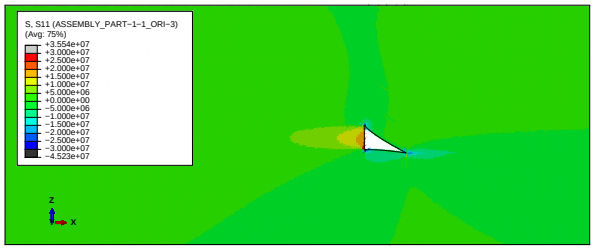

(a) Single drop-off model

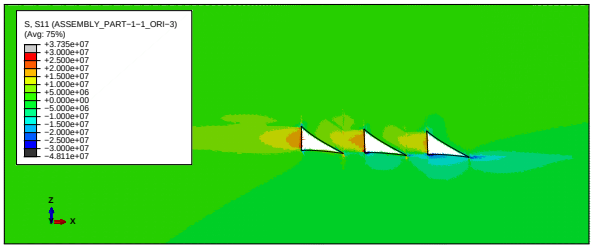

(b) Multiple drop-off model - Stagger distance 1.5B. Topology 1

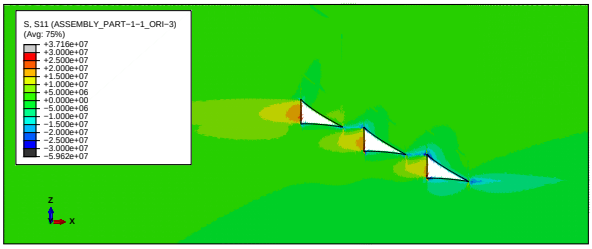

(c) Multiple drop-off model - Stagger distance 1.5B. Topology 2

Figure 6.8: Contour plots of in-plane stress in global x-direction. Single- and multiple ply drop-off model with aspect ratio of 1/1.5. All 0° layup. Resin pockets are hidden for clarification. Unit of contour limit values in Pascal

6.2. Conclusions

Based on the changing stress levels and the local stress regions observed in the contour plots it can be concluded that implementing multiple ply drop-off regions within a laminate influences the residual stress around these regions significantly. Without taking into account the influence of stress interactions caused by different ply orientations, implementing multiple ply drop-offs influences the maximum out-of-plane stress within the core- and belt ply by increasing this stress at the 1st drop-off, while it is decreased at the 2nd drop-off and even lower for the 3rd drop-off. Whenever multiple drop-offs are arranged with a common core ply (topology 1), the largest stress increase occurs within the belt ply, while a common belt ply arrangement (topology 2) results in the largest stress increase within the core ply, both being located at the 1st drop-off.

Whenever the influence of stress interactions caused by different ply orientations is taken into account, it can be concluded that when implementing multiple drop-offs using topology 1, generally all stress levels at each drop-off are increased compared to a single drop-off. This effect was unexpected considering the overall decrease in stress at the 2nd and 3rd drop-off whenever the influence of different ply orientations is being neglected. The stress at the 1st drop-off decreases with increasing stagger distance, while the stress at the 2nd/3rd drop-off is increased.

By arranging multiple drop-offs using topology 2 and by including the influence of interactions caused by ply orientations, the obtained results are more in line with the results of implementing multiple ply drop-offs without considering different ply orientations. The relatively higher stress within core- and belt ply at the 1st drop-off increases even further, while the stress levels at the 2nd and 3rd drop-off are still lower than the single drop-off. Minor decrease in stress at the 1st drop-off and increase in stress at the 2nd drop-off can be observed for increasing stagger distance, where for the 3rd drop-off the stress increases to the single drop-off value.

Overall it can be concluded that the first drop-off is most critical regarding stress increases, regardless whether different ply orientations are implemented around the multiple drop-off regions. Similar as observed in section 5.2, the effect of stress increase resulting from higher in-plane thermal contraction and shrinkage within the terminated ply compared to surrounding plies remains applicable for multiple drop-off implementations, where this effect is most dominant for topology 2.

When evaluating the ply drop-off guidelines from section 2.5.1, it can be concluded that these must be further specified for each topology when cure-induced stress around drop-off regions are incorporated. The existing guidelines recommend a stagger distance of at least three times or eight times the ply

thickness for 0°/90° or 45° orientation for the terminated ply, respectively. These minimal values correspond to a stagger distance S of 2B and 5.3B for the applicable pocket geometries within the multiple drop-off model. For topology 1 with different ply orientations, no excessively large stress levels can be observed for the stagger distance variations used. Considering this, the minimal stagger distances of 2B and 5.3B prescribed by the guidelines cannot be substantiated by these results, as both 0° and 45°plies are terminated without resulting in significant differences in stress level. This is different for topology 2 with multiple ply orientations, where the stress levels at the 1^{st} drop-off are considerably increased, resulting from the 45° terminated ply. These relatively higher absolute stress levels can only become more damaging whenever the laminate is loaded in the direction of the drop-off, which is why these increased local stress levels should be prevented. Considering this, the larger minimal stagger distance of eight times the thickness for 45° dropped plies is valid for this topology.

7

Conclusions and Recommendations

This research project was initiated to increase the understanding of cure-induced residual stress generation around ply drop-off regions within thick composite laminates. As result, the following main research question is formulated:

> 'What is the influence of ply drop-off regions and related process and laminate parameters within thick composite laminates on the cure-induced residual stress generation and related distortions as result of RTM manufacturing processes?'

which is answered in section 7.1. Hereafter, recommendations regarding implementation of ply drop-off regions and further research are presented in section 7.2.

7.1. Conclusions

Cure-induced residual stress affects composite laminates in different ways. Literature review showed that for thin laminates, stress redistribution results in geometry distortions such as bending curvature or warpage. Whenever laminate thickness is increased, redistribution through deformation becomes more difficult and can result in distortions such as ply delamination and matrix cracking when out-of-plane tensile stress levels increase. Cure simulations showed that single ply drop-off regions influence the cure-induced out-of-plane tensile stress by increasing it locally, where the most significant stress levels occur below and above the resin pocket, within the core- and belt ply, respectively. An influence of the ply drop-off on the global stress distribution of the laminate cannot be identified, whether being implemented in thin- or thick laminates. Whenever the laminate thickness is increased, no significant influence on local stress levels within drop-off regions related to this thickness increase can be observed.

Since both thermal expansion and chemical shrinkage of the resin pocket develop in counteracting manner during the heating stage of the cure process, an almost stress-free drop-off region is present at the end of this stage. As at this point the resin modulus is still insignificant and vitrifaction has not taken place, it is highly unlikely that stress related laminate distortions occur during this stage. As result, under these conditions the heating stage can be seen as a non-critical part of the cure phase in terms of process defects. From upon the dwell stage, the chemical shrinkage surpasses the thermal expansion. This effect combined with the resin modulus becoming significant and the vitrification of the resin when the Glass transition temperature (Tg) approaches the dwell temperature, it results in an effective out-of-plane tensile stress within core- and belt ply. These stress levels become even more critical during the cool down stage as result of the thermal contraction of the resin pocket in glassy state combined with the increasing resin modulus due to the temperature decrease.

Regarding the influence of process parameters, the dwell temperature and cool down rate can be identified as most significant. Primarily the cool down rate, where increasing this rate results in lower final stress levels. Despite that this effect is counterintuitive, it can be related to the vitrification point which is postponed to lower temperatures as the rate increases. Consequently, lower effective thermal

contraction after resin vitrification takes place in the glassy state, which results in lower final stress levels.

This is an interesting effect because even with the most basic cure cycle profile used, which results in almost all Degree of Cure (DOC) development takes place during the heating- and dwell stage, still the cool down stage has an influence on the final stress levels. Naturally this effect is dependent on the type of resin and its exothermic reactivity, because whenever vitrification of the resin occurs already during the dwell stage, the cool down rate may have a less pronounced effect on the final stress values. For the dwell temperature, only significant influences on the stress development can be identified via the DOC, where increased dwell temperatures result in higher DOC values which subsequently results in higher stress levels. Whenever the dwell temperature is selected as such that the Tg development approaches about equal values as the dwell temperature during this stage, significant stress development can occur prior to vitrification as the resin modulus already becomes significant.

The geometry of the resin pocket is in essence related to the flexibility of the covering belt ply in the direction of the drop-off and therefore the in-plane stiffness, where lower stiffness results in larger aspect ratios. Different combinations of aspect ratios and ply orientations for core- and belt ply demonstrated that both these parameters have a significant influence on the maximum out-of-plane tensile stress. Higher in-plane stiffness of these plies and higher aspect ratios result in an increased out-of-plane stress within the core- and belt ply. More interesting is the combined effect of these two parameters. By considering that the lower in-plane stiffness of these plies inherently results in larger aspect ratios, the combination of these opposing effects turned out to be advantageous by reducing the significance of the stress increase. Furthermore, increasing the aspect ratio results in a non-linear increase of the maximum out-of-plane stress, where the differences between relatively smaller ratios, i.e. a/b values below 1/12, become almost negligible. This increasing effect for larger aspect ratios is less significant for drop-offs when core- and belt ply have lower in-plane stiffness. Another influence arises from the terminated ply orientation within the drop-off. Lower in-plane shrinkage and contraction relative to the surrounding core- and belt ply is beneficial as it decreases the out-of-plane stress, where relatively higher in-plane shrinkage and contraction is more detrimental and can double the stress for higher aspect ratios.

Often multiple ply drop-off regions are implemented in composite laminates to obtain the required thickness reduction along the part. Within these regions, the stagger distance is introduced as an important parameter which defines the distance between the multiple ply drop-offs. When these drop-offs are implemented, it cannot be avoided to influence the out-of-plane stress around these regions. When considering the fundamental influence, and thus ignoring stress interactions caused by different ply orientations, the maximum out-of-plane stress increases at the 1st drop-off and decreases at the 2nd and 3rd drop-off. This effect holds regardless whether a common core- or belt ply topology is used. When taking the influence of stress interactions into account, local regions of increased in-plane tensile stress between drop-offs, and decreased in-plane compressive stress above and below drop-offs can be observed. Whenever these regions occur close to the resin pocket within the core- and belt ply, both types of stress regions have an increasing effect on the maximum out-of-plane stress.

When implementing multiple ply drop-offs using topologies based a common core ply, all stress levels at each drop-off are higher compared to the single drop-off whenever different ply orientations are included. With increasing stagger distance, stress levels at the 1st drop-off decrease, where at both the 2nd and 3rd drop-off these stress levels increase to a greater extent. Using common belt ply topologies for multiple drop-off implementations, changes in stress level caused by stress interactions are more in accordance with the fundamental influence of the multiple drop-off region itself. Where for the 1st drop-off stress levels are significantly higher, for 2nd and 3rd drop-off these levels are still lower than the single drop-off. With increasing stagger distance, each stress level progresses towards the single drop-off value.

7.1.1. Ply Drop-off Guidelines

Resulting from the conclusions, the following guidelines can be proposed to reduce the out-of-plane tensile stress increase as result of the implementation of ply drop-off regions:

- The number of terminated plies within a drop-off region should be kept at a minimum, i.e. preferably a single ply per drop-off, as dropping multiple plies at once increases the aspect ratio of the resin pocket and consequently the out-of-plane tensile stress at this location.
- The core- and belt ply orientation should be selected as such that the in-plane thermal contraction and chemical shrinkage of these plies in the direction of the drop-off is at least equal-, but preferably higher than the dropped ply:
  - When a 0° orientated ply must be dropped, select an orientation for core- and belt ply of 0° but preferably 45° or 90°.
  - When a 45° orientated ply must be dropped, select an orientation for core- and belt ply of 45° but preferably 90°.
  - When a 90° orientated ply must be dropped, select an orientation for core- and belt ply of 90°.
- The dwell temperature must be selected high enough to obtain the required DOC within the available process time, but not higher than 5-10 °C above the practical achievable Tg. Dwell temperatures which are significantly higher result in unnecessary stress development around drop-off regions.
- The cool down rate should be increased, up to the limits of the process equipment and assuring no significant temperature gradients are induced throughout the part, to reduces tensile stress development after vitrification of the resin during the cool down stage.
- Implementing multiple drop-offs should be achieved by a common core ply arrangement, as this topology results in the most evenly distributed increase in out-of-plane tensile stress around all drop-offs. This can extent the margin to whenever these stress levels can become critical upon loading of the laminate.
  - Whenever a common belt ply arrangement is required for implementing multiple drop-offs, select the layup as such that the 1st drop-off consist of a 0° terminated ply surrounded by 90° core- and belt ply, as this drop-off naturally results in the largest stress increase.
- The stagger distance between multiple drop-off regions should be determined based on the applicable drop-off:
  - The distance between the 1st and 2nd drop-off should be at least 4.5 times the ply thickness, but preferably as large as possible within the multiple drop-off arrangement.
  - The distance between the 2nd and 3rd drop-off can be selected smaller, preferably between 2-3 times the ply thickness.
- Avoid aligning multiple ply drop-offs vertically, as it is expected that the observed out-of-plane tensile stress regions above and below each resin pocket can have a mutually increasing effect on the maximum stress at these locations.
- When multiple ply drop-offs are implemented, integrate applicable design guidelines at the first drop-off primarily as the highest increase in out-of-plane tensile stress occurs at this location.

7.2. Recommendations

For further research related to the influence of ply drop-off regions on the cure-induced residual stress the following is proposed. First of all, the thermal-mechanical Finite Element Analysis (FEA) model established for this study can be improved in various ways. Implementing a more realistic ply drop-off and resin pocket geometry where voids, slippage of plies and thickness reduction of the terminated ply-end are all included, it can result in an improved prediction accuracy of the residual stress around these regions. For instance by including a void at the ply-boundary of the resin pocket, this can influence the

location and magnitude of the maximum out-of-plane tensile stress observed within the core- and belt ply significantly.

By adding cohesive elements around drop-off regions, delamination mechanisms can be incorporated within the analysis to investigate if and when stress levels can become critical. Furthermore, evaluation of the critical stress locations within drop-off regions via contour plots can be improved by implementing a more gradual transition of local material orientations between the straight- and oblique ply sections. As of the orthotropic nature of modelling composites in FEA, it can be recommended to implement corner regions and inter-ply layers of isotropic resin material to avoid overestimations in stress levels resulting from the singularities arising at sharp corners around the resin pocket.

Expanding the variation range of the input parameters for the ply drop-off model can result in additional data to improve the understanding of this laminate feature. For instance the ply orientations, where for the current study equal values were implemented for both the core- and belt ply. By alternating the orientations for each of these plies, more layup combinations within the drop-off region can be investigated to assess the influence. Increasing the maximum stagger distance variation can confirm if and when the observed stress interactions are no longer of influence on the stress levels within the drop-off regions.

In addition, as the process used by FLG is based on RTM, changing the model boundary conditions into a two-sided rigid mould process can influence the stress levels around the drop-off regions as well. Whenever RTM boundary conditions are implemented, it is expected that the thickness reduction observed for VARTM cannot occur in the same amount as it is restricted by the rigid mould surfaces. This process variation can result in significant changes in the overall stress built-up around ply drop-off regions, as less relaxation of the laminate in through-thickness direction is possible.

At last, implementing other types of resin systems for the matrix material within the simulation model can increase the understanding of the influence of different resin states on the residual stress development. As it is observed that early stress development during the dwell and prior to vitrification can effect the final stress levels around drop-off regions, varying in different types of resin systems can confirm if this effect holds for other resin systems as well.

Bibliography

[1] C. Meola, S. Boccardi, and G. M. Carlomagno. Composite Materials in the Aeronautical Industry. In *Infrared Thermography in the Evaluation of Aerospace Composite Materials*, chapter 1, pages 1–24. Elsevier Science Ltd, 2017. doi:10.1016/b978-1-78242-171-9.00001-2.

[2] J. A. E. Manson, M. D. Wakeman, and N. Bernet. Composite Processing and Manufacturing—An Overview. In *Comprehensive Composite Materials*, chapter 16, pages 577–607. Elsevier, 2000. doi:10.1016/b0-08-042993-9/00167-4.

[3] E. M. Sozer, P. Simacek, and S. G. Advani. Resin transfer molding (RTM) in polymer matrix composites. In *Manufacturing Techniques for Polymer Matrix Composites (PMCs)*, chapter 9, pages 245–309. Woodhead Publishing Limited, 2012. doi:10.1016/B978-0-85709-067-6.50009-2.

[4] Netherlands Aerospace Centre. Composites R&D - Online Brochure, 2020.

[5] S. G. Advani and E. M. Sozer. Liquid Molding of Thermoset Composites. In *Comprehensive Composite Materials*, chapter 2.23, pages 807–844. Elsevier Science Ltd, 2000. doi:10.1016/b0-08-042993-9/00171-6.

[6] M. W. Nielsen. *Prediction of process induced shape distortions and residual stresses in large fibre reinforced composite laminates: With application to Wind Turbine Blades*. PhD thesis, Technical University of Denmark, 2013.

[7] E. Ruiz and F. Trochu. Thermomechanical properties during cure of glass-polyester RTM composites: Elastic and viscoelastic modeling. *Journal of Composite Materials*, 39(10):881–916, 2005. doi:10.1177/0021998305048732.

[8] A. A. Johnston. *An Integrated Model Of The Development Of Process-Induced Deformation In Autoclave Processing Of Composite Structures (PhD thesis*. Phd thesis, The University Of British Columbia, 1997.

[9] T. Garstka, N. Ersoy, K. D. Potter, and M. R. Wisnom. In situ measurements of through-the-thickness strains during processing of AS4/8552 composite. *Composites Part A: Applied Science and Manufacturing*, 38(12):2517–2526, dec 2007. doi:10.1016/j.compositesa.2007.07.018.

[10] R. J. Young and P. A. Lovell. *Introduction to Polymers: Third Edition*. Taylor & Francis Group, Boca Raton, 3rd ed. edition, 2011.

[11] S. M. Sabzevari. *Cure kinetics and process modeling of a carbon-fiber thermoplastic-toughened epoxy resin prepreg*. Msc thesis, Wichita State University, 2010.

[12] P. P. Parlevliet and H. Bersee. Measurement of polymerisation shrinkage of matrices for liquid moulding. *ICCM International Conferences on Composite Materials*, 2009.

[13] L. Boogh and R. Mezzenga. Processing Principles for Thermoset Composites. In *Comprehensive Composite Materials*, chapter 19, pages 671–699. Elsevier, 2000. doi:10.1016/b0-08-042993-9/00221-7.

[14] D. J. Michaud, A. N. Beris, and P. S. Dhurjati. Curing behavior of thick-sectioned RTM composites. *Journal of Composite Materials*, 32(14):1273–1296, jul 1998. doi:10.1177/002199839803201402.

[15] A. G. Cassano, S. E. Stapleton, C. J. Hansen, and M. Maiaru. Prediction of Cure Overheating in Thick Adhesive Bondlines for Wind Energy Applications. In *Guidelines for Papers to be Presented at the ABAQUS Users' Conference*, pages 1–10, Lowell, Massachusetts, 2002.

[16] L. J. Lee, W. B. Young, and R. J. Lin. Mold filling and cure modeling of RTM and SRIM processes. *Composite Structures*, 27(1-2):109–120, 1994. doi:10.1016/0263-8223(94)90072-8.

[17] C. L. Tucker. Heat transfer and reaction issues in liquid composite molding. *Polymer Composites*, 17(1):60–72, 1996. doi:10.1002/pc.10591.

[18] J. M. Balvers. *In situ strain & cure monitoring in liquid composite moulding by fibre Bragg grating sensors*. PhD thesis, Delft University of Technology, 2014.

[19] A. C. Loos and G. S. Springer. Curing of Epoxy Matrix Composites. *Journal of Composite Materials*, 17(2):135–169, 1983. doi:10.1177/002199838301700204.

[20] E. Ruiz and F. Trochu. Multi-criteria thermal optimization in liquid composite molding to reduce processing stresses and cycle time. *Composites Part A: Applied Science and Manufacturing*, 37 (6):913–924, 2006. doi:10.1016/j.compositesa.2005.06.010.

[21] K. M. Pillai. Modeling the unsaturated flow in liquid composite molding processes: A review and some thoughts. *Journal of Composite Materials*, 38(23):2097–2118, 2004. doi:10.1177/0021998304045585.

[22] S. R. White and H. T. Hahn. Process Modeling of Composite Materials: Residual Stress Development during Cure. Part I. Model Formulation. *Journal of Composite Materials*, 26(16):2402–2422, 1992. doi:10.1177/002199839202601604.

[23] A. A. Skordos. *Modelling and monitoring of resin transfer moulding*. PhD thesis, Cranfield University, 2000.

[24] M. Hayaty, M. H. Beheshty, and M. Esfandeh. Cure kinetics of a glass/epoxy prepreg by dynamic differential scanning calorimetry. *Journal of Applied Polymer Science*, 120(1):62–69, 2011. doi:10.1002/app.32982.

[25] P. I. Karkanas and I. K. Partridge. Cure modeling and monitoring of epoxy/amine resin systems. I. Cure kinetics modeling. *Journal of Applied Polymer Science*, 77(7):1419–1431, 2000. doi:10.1002/1097-4628(20000815)77:7<1419::AID-APP3>3.0.CO;2-N.

[26] P. I. Karkanas. Modelling the cure of a commercial epoxy resin for applications in resin transfer moulding. *Polymer International*, 41(2):183–191, 1996. doi:10.1002/(SICI)1097-0126(199610)41:2<183::AID-PI621>3.0.CO;2-F.

[27] M. E. Ryan and A. Dutta. Kinetics of epoxy cure: a rapid technique for kinetic parameter estimation. *Polymer*, 20(2):203–206, 1979. doi:10.1016/0032-3861(79)90222-2.

[28] L. Shi. *Heat Transfer in the Thick Thermoset Composites*. PhD thesis, Delft University of Technology, 2016.

[29] H. E. Kissinger. Reaction Kinetics in Differential Thermal Analysis. *Analytical Chemistry*, 29(11): 1702–1706, 1957. doi:10.1021/ac60131a045.

[30] W. I. Lee, A. C. Loos, and G. S. Springer. Heat of Reaction, Degree of Cure, and Viscosity of Hercules 3501-6 Resin. *Journal of Composite Materials*, 16(6):510–520, 1982. doi:10.1177/002199838201600605.

[31] M. R. Kamal. Thermoset characterization for moldability analysis. *Polymer Engineering & Science*, 14(3):231–239, 1974. doi:10.1002/pen.760140312.

[32] K. C. Cole. A New Approach to Modeling the Cure Kinetics of Epoxy Amine Thermosetting Resins. 2. Application to a typical system based on Bis [4- (diglycidylamino)phenyl] methane and Bis(4-aminophenyl) Sulfone. *Macromolecules*, 24(11):3093–3097, 1991. doi:10.1021/ma00011a011.

[33] C. S Chern and G. W. Poehlein. A kinetic model for curing reactions of epoxides with amines. *Polymer Engineering & Science*, 27(11):788–795, 1987. doi:10.1002/pen.760271104.

[34] J. M. Barton. The application of differential scanning calorimetry (DSC) to the study of epoxy resin curing reactions. In *Epoxy Resins and Composites I*, pages 111–154. Springer Berlin Heidelberg, Berlin, Heidelberg, 1985. doi:10.1007/3-540-15546-5_5.

[35] L. Khoun, T. Centea, and P. Hubert. Characterization methodology of thermoset resins for the processing of composite materials - Case study: CYCOM 890RTM Epoxy Resin. *Journal of Composite Materials*, 44(11):1397–1415, 2010. doi:10.1177/0021998309353960.

[36] P. Hubert, A. A. Johnston, A. Poursartip, and K. Nelson. Cure Kinetics and Viscosity Models for Hexcel 8552 Epoxy Resin. *Int SAMPE Symp Exhibit*, 46:2341–2354, 2001.

[37] M. Zarrelli, A. A. Skordos, and I. K. Partridge. Investigation of cure induced shrinkage in unreinforced epoxy resin. *Plastics, Rubber and Composites*, 31(9):377–384, 2002. doi:10.1179/146580102225006350.

[38] J. Balvers, H. Bersee, A. Beukers, and K. Jansen. Determination of Cure Dependent Properties for Curing Simulation of Thick-Walled Composites. In *49th AIAA/ASME/ASCE/AHS/ASC Structures, Structural Dynamics*, number April, pages 1–15. American Institute of Aeronautics and Astronautics, apr 2008. doi:10.2514/6.2008-2035.

[39] J. P. Pascault and R. J. J. Williams. Relationships between glass transition temperature and conversion - Analyses of limiting cases. *Polymer Bulletin*, 24(1):115–121, 1990. doi:10.1007/BF00298330.

[40] A. Yousefi, P. G. Lafleur, and R. Gauvin. Kinetic studies of thermoset cure reactions: A review. *Polymer Composites*, 18(2):157–168, 1997. doi:10.1002/pc.10270.

[41] T. S. Mesogitis, A. A. Skordos, and A. C. Long. Stochastic simulation of the influence of cure kinetics uncertainty on composites cure. *Composites Science and Technology*, 110:145–151, 2015. doi:10.1016/j.compscitech.2015.02.009.

[42] G. Struzziero and A. A. Skordos. Multi-objective optimization of Resin Infusion. *Advanced Manufacturing: Polymer & Composites Science*, 5(1):17–28, 2019. doi:10.1080/20550340.2019.1565648.

[43] C. Bellini, L. Sorrentino, W. Polini, and A. Corrado. Spring-in analysis of CFRP thin laminates: numerical and experimental results. *Composite Structures*, 173:17–24, aug 2017. doi:10.1016/j.compstruct.2017.03.105.

[44] R. Joven, R. Das, A. Ahmed, P Roozbehjavan, and B. Minaie. Thermal properties of carbon fiber-epoxy composites with different fabric weaves. In *International SAMPE Technical Conference*, 2012.

[45] K. I. Tifkitsis, T. S. Mesogitis, G. Struzziero, and A. A. Skordos. Stochastic multi-objective optimisation of the cure process of thick laminates. *Composites Part A: Applied Science and Manufacturing*, 112:383–394, sep 2018. doi:10.1016/j.compositesa.2018.06.015.

[46] G. Struzziero and J.J.E. Teuwen. Residual Stresses Generation in Ultra-Thick Components for Wind Turbine Blades. *Procedia CIRP*, 85:8–12, 2019. doi:10.1016/j.procir.2019.09.002.

[47] R. A. Schapery. Thermal Expansion Coefficients of Composite Materials Based on Energy Principles. *Journal of Composite Materials*, 2(3):380–404, 1968. doi:10.1177/002199836800200308.

[48] G. Struzziero, D. Nardi, J. Sinke, and J. J. E. Teuwen. Cure-induced residual stresses for warpage reduction in thermoset laminates. *Journal of Composite Materials*, 54(22):3055–3065, 2020. doi:10.1177/0021998320908631.

[49] T. S. Mesogitis, A. A. Skordos, and A. C. Long. Stochastic simulation of the influence of fibre path variability on the formation of residual stress and shape distortion. *Polymer Composites*, 38(12): 2642–2652, 2017. doi:10.1002/pc.23856.

[50] Y. Nawab, S. Shahid, N. Boyard, and F. Jacquemin. Chemical shrinkage characterization techniques for thermoset resins and associated composites. *Journal of Materials Science*, 48(16): 5387–5409, aug 2013. doi:10.1007/s10853-013-7333-6.

[51] C. Li, K. Potter, M. R. Wisnom, and G. Stringer. In-situ measurement of chemical shrinkage of MY750 epoxy resin by a novel gravimetric method. *Composites Science and Technology*, 64(1): 55–64, 2004. doi:10.1016/S0266-3538(03)00199-4.

[52] O. G. Kravchenko, S. G. Kravchenko, and R. B. Pipes. Chemical and thermal shrinkage in thermosetting prepreg. *Composites Part A: Applied Science and Manufacturing*, 80:72–81, jan 2016. doi:10.1016/j.compositesa.2015.10.001.

[53] M. R. Wisnom, M. Gigliotti, N. Ersoy, M. Campbell, and K. D. Potter. Mechanisms generating residual stresses and distortion during manufacture of polymer–matrix composite structures. *Composites Part A: Applied Science and Manufacturing*, 37(4):522–529, apr 2006. doi:10.1016/j.compositesa.2005.05.019.

[54] L. Khoun and P. Hubert. Investigation of the dimensional stability of carbon epoxy cylinders manufactured by resin transfer moulding. *Composites Part A: Applied Science and Manufacturing*, 41 (1):116–124, 2010. doi:10.1016/j.compositesa.2009.06.014.

[55] K. D. Potter. Understanding the origins of defects and variability in composites manufacture. In *ICCM International Conferences on Composite Materials*, 2009.

[56] P. P. Parlevliet. *Residual Strains in Thick Thermoplastic Composites*. PhD thesis, Delft University of Technology, 2010.

[57] P. P. Parlevliet, H. E. N. Bersee, and A. Beukers. Residual stresses in thermoplastic composites-A study of the literature-Part I: Formation of residual stresses. *Composites Part A: Applied Science and Manufacturing*, 37(11):1847–1857, 2006. doi:10.1016/j.compositesa.2005.12.025.

[58] T. A. Bogetti and J. W. Gillespie. Process-Induced Stress and Deformation in Thick-Section Thermoset Composite Laminates. *Journal of Composite Materials*, 26(5):626–660, 1992. doi:10.1177/002199839202600502.

[59] A. R. R. Adli and K. M. B. Jansen. Numerical investigation and experimental validation of residual stresses building up in microelectronics packaging. *Microelectronics Reliability*, 62:26–38, 2016. doi:10.1016/j.microrel.2016.03.015.

[60] G. Twigg, A. Poursartip, and G. Fernlund. Tool-part interaction in composites processing. Part I: Experimental investigation and analytical model. *Composites Part A: Applied Science and Manufacturing*, 35(1):121–133, 2004. doi:10.1016/S1359-835X(03)00131-3.

[61] K. D. Potter, M. Campbell, C. Langer, and M. R. Wisnom. The generation of geometrical deformations due to tool/part interaction in the manufacture of composite components. *Composites Part A: Applied Science and Manufacturing*, 36(2):301–308, 2005. doi:10.1016/j.compositesa.2004.06.002.

[62] M. R. Wisnom, L. G. Stringer, R. J. Hayman, and M. J. Hinton. Curing Stresses in Thick Polymer Composite Components, Part I: Analysis. In *Proceedings of the ICCM12*, 1999.

[63] G. Struzziero and A. A. Skordos. Multi-objective optimisation of the cure of thick components. *Composites Part A: Applied Science and Manufacturing*, 93:126–136, feb 2017. doi:10.1016/j.compositesa.2016.11.014.

[64] N. Rabearison, Ch. Jochum, and J. C. Grandidier. A FEM coupling model for properties prediction during the curing of an epoxy matrix. *Computational Materials Science*, 45:715–724, 2009. doi:10.1016/j.commatsci.2008.11.007.

[65] C. C. Chamis. Mechanics of composite materials: Past, present, and future. *Journal of Composites Technology and Research*, 11(1):3–14, 1989. doi:10.1520/ctr10143j.

[66] C. Bellini and L. Sorrentino. Analysis of cure induced deformation of CFRP U-shaped laminates. *Composite Structures*, 197:1–9, aug 2018. doi:10.1016/j.compstruct.2018.05.038.

[67] T. A. Bogetti and J. W. Gillespie. Two-Dimensional Cure Simulation of Thick Thermosetting Composites. *Journal of Composite Materials*, 25(3):239–273, 1991. doi:10.1177/002199839102500302.

[68] Sh. Teplinsky and E. M. Gutman. Computer simulation of process induced stress and strain development during cure of thick-section thermosetting composites. *Computational Materials Science*, 6(1):71–76, 1996. doi:10.1016/0927-0256(96)00035-3.

[69] H. C. Park and S.W. Lee. Cure simulation of thick composite structures using the finite element method. *Journal of Composite Materials*, 35(3):188–201, 2001. doi:10.1106/31G6-F5AL-F87L-WDE8.

[70] J. Zhang, Y. C. Xu, and P. Huang. Effect of cure cycle on curing process and hardness for epoxy resin. *Express Polymer Letters*, 3(9):534–541, 2009. doi:10.3144/expresspolymlett.2009.67.

[71] N. Ersoy, T. Garstka, K. Potter, M. R. Wisnom, D. Porter, and G. Stringer. Modelling of the spring-in phenomenon in curved parts made of a thermosetting composite. *Composites Part A: Applied Science and Manufacturing*, 41(3):410–418, mar 2010. doi:10.1016/j.compositesa.2009.11.008.

[72] B. Varughese and A. Mukherjee. A ply drop-off element for analysis of tapered laminated composites. *Composite Structures*, 39(1-2):123–144, sep 1997. doi:10.1016/S0263-8223(97)00132-3.

[73] A.J. Vizzini. Influence of Realistic Ply-Drop Geometries on Interlaminar Stresses in Tapered Laminates. In *Composite Materials: Fatigue and Fracture: Fifth Volume*, number 1230, pages 467–485. ASTM International, 100 Barr Harbor Drive, PO Box C700, West Conshohocken, PA 19428-2959, 1995. doi:10.1520/STP14030S.

[74] R.K. Cannon. *The Effects of Ply Dropoffs on the Tensile Behavior of Graphite/Epoxy Laminates*. Msc. thesis, Massachusetts Institute of Technology, 1988.

[75] B. Varughese and A. Mukherjee. Analysis of Tapered Laminated Composites with Non-Symmetric Lay-Up. *Journal of Reinforced Plastics and Composites*, 16(7):631–660, 1997.

[76] K. W. Gan, G. Allegri, and S. R. Hallett. A simplified layered beam approach for predicting ply drop delamination in thick composite laminates. *Materials and Design*, 108:570–580, oct 2016. doi:10.1016/j.matdes.2016.06.105.

[77] A. Mukherjee and B. Varughese. Design guidelines for ply drop-off in laminated composite structures. *Composites Part B: Engineering*, 32(2):153–164, 2001. doi:10.1016/S1359-8368(00)00038-X.

[78] P. D. Mangalgiri and K. Vijayaraju. An analytical study on 0/90 ply-drops in composite laminates. *Composite Structures*, 28(2):181–187, 1994. doi:10.1016/0263-8223(94)90047-7.

[79] M. Mulle, F. Collombet, P. Olivier, R. Zitoune, C. Huchette, F. Laurin, and Y. H. Grunevald. Assessment of cure-residual strains through the thickness of carbon-epoxy laminates using FBGs Part II: Technological specimen. *Composites Part A: Applied Science and Manufacturing*, 40(10): 1534–1544, 2009. doi:10.1016/j.compositesa.2009.06.013.

[80] G. Struzziero and J. J. E. Teuwen. Effect of convection coefficient and thickness on optimal cure cycles for the manufacturing of wind turbine components using VARTM. *Composites Part A: Applied Science and Manufacturing*, 123:25–36, aug 2019. doi:10.1016/j.compositesa.2019.04.024.

[81] E. Ruiz and F. Trochu. Numerical analysis of cure temperature and internal stresses in thin and thick RTM parts. *Composites Part A: Applied Science and Manufacturing*, 36(6):806–826, 2005. doi:10.1016/j.compositesa.2004.10.021.

[82] ABAQUS. *Abaqus Analysis User's Guide*. Dassault Systèmes, 6.14 edition, 2014.

[83] L. Sorrentino and C. Bellini. Compaction influence on spring-in of thin composite parts: Experimental and numerical results. *Journal of Composite Materials*, 49(17):2149–2158, 2015. doi:10.1177/0021998314542362.

[84] ABAQUS. *Abaqus User Subroutines Reference Guide*. Dassault Systèmes, 6.14 edition, 2014.

[85] 6.14, editor. *Abaqus/CAE User's Guide*. Dassault Systèmes, 2014.

[86] B. Tavakol, P. Roozbehjavan, A. Ahmed, R. Das, R. Joven, H. Koushyar, A. Rodriguez, and B. Minaie. Prediction of residual stresses and distortion in carbon fiber-epoxy composite parts due to curing process using finite element analysis. *Journal of Applied Polymer Science*, 128(2):941–950, 2013. doi:10.1002/app.38075.

[87] J. D. Farmer and E. E. Covert. Thermal conductivity of a thermosetting advanced composite during its cure. *Journal of Thermophysics and Heat Transfer*, 10(3):467–475, 1996. doi:10.2514/3.812.

[88] H. Z. Shan and T. W. Chou. Transverse elastic moduli of unidirectional fiber composites. *Composites Science and Technology*, 53(5):383–391, 1995. doi:10.2115/fiber.43.10_520.

[89] D. J. O'Brien, P. T. Mather, and S. R. White. Viscoelastic properties of an epoxy resin during cure. *Journal of Composite Materials*, 35(10):883–904, 2001. doi:10.1106/HLYM-5CM7-BP9N-L1Y1.

[90] ASTM International. Standard Test Methods for Kinetic Parameters by Differential Scanning Calorimetry Using Isothermal Methods, 2013.

[91] M. Sadeghinia, K. M B Jansen, and L. J. Ernst. Characterization and modeling the thermo-mechanical cure-dependent properties of epoxy molding compound. *International Journal of Adhesion and Adhesives*, 32(1):82–88, 2012. doi:10.1016/j.ijadhadh.2011.10.007.

A

Fortran Subroutine Code

```
!==============================General comment=====================================!
! This Subroutine code file is written as part of the MSc research study conducted
! by Tom van Loon. Parts of the code are based on the research performed by Giacomo
! Struzziero (https://doi.org/10.1177/0021998320908631) while the rest is
! added/changed to make it applicable suitable for Abaqus CAE 2019.
!
! The following code is based on multiple subroutines that are used by the Abaqus
! solver to describe the evolution of both the thermochemical- and thermomechanical
! properties of the ply material properties. Notes and applicable units for each
! parameter or governing equation are given within each subroutine.
!==========================================================================!
      SUBROUTINE SDVINI(STATEV,COORDS,NSTATV,NCRDS,NOEL,NPT,
     1 LAYER,KSPT)
      INCLUDE 'ABA_PARAM.INC'
      DIMENSION STATEV(NSTATV),COORDS(NCRDS)
      DOUBLE PRECISION DOC_initial
      DOC_initial=8.0D-2        !Set initial DOC
      STATEV(20)=DOC_initial
      RETURN
      END

      SUBROUTINE UMAT(STRESS,STATEV,DDSDDE,SSE,SPD,SCD,
     1 RPL,DDSDDT,DRPLDE,DRPLDT,
     2 STRAN,DSTRAN,TIME,DTIME,TEMP,DTEMP,PREDEF,DPRED,CMNAME,
     3 NDI,NSHR,NTENS,NSTATV,PROPS,NPROPS,COORDS,DROT,PNEWDT,
     4 CELENT,DFGRD0,DFGRD1,NOEL,NPT,LAYER,KSPT,JSTEP,KINC)
      INCLUDE 'ABA_PARAM.INC'
      CHARACTER*80 CMNAME

      IF (CMNAME(1:3) .EQ. 'PLY') THEN
      CALL UMAT_PLY(STRESS,STATEV,DDSDDE,SSE,SPD,SCD,
     1 RPL,DDSDDT,DRPLDE,DRPLDT,
     2 STRAN,DSTRAN,TIME,DTIME,TEMP,DTEMP,PREDEF,DPRED,CMNAME,
     3 NDI,NSHR,NTENS,NSTATV,PROPS,NPROPS,COORDS,DROT,PNEWDT,
     4 CELENT,DFGRD0,DFGRD1,NOEL,NPT,LAYER,KSPT,JSTEP,KINC)

      ELSE IF(CMNAME(1:5) .EQ. 'RESIN') THEN
      CALL UMAT_RESIN(STRESS,STATEV,DDSDDE,SSE,SPD,SCD,
     1 RPL,DDSDDT,DRPLDE,DRPLDT,
     2 STRAN,DSTRAN,TIME,DTIME,TEMP,DTEMP,PREDEF,DPRED,CMNAME,
     3 NDI,NSHR,NTENS,NSTATV,PROPS,NPROPS,COORDS,DROT,PNEWDT,
     4 CELENT,DFGRD0,DFGRD1,NOEL,NPT,LAYER,KSPT,JSTEP,KINC)
      END IF
```

```
      RETURN
      END

      SUBROUTINE UMAT_PLY(STRESS,STATEV,DDSDDE,SSE,SPD,SCD,
     1 RPL,DDSDDT,DRPLDE,DRPLDT,
     2 STRAN,DSTRAN,TIME,DTIME,TEMP,DTEMP,PREDEF,DPRED,CMNAME,
     3 NDI,NSHR,NTENS,NSTATV,PROPS,NPROPS,COORDS,DROT,PNEWDT,
     4 CELENT,DFGRD0,DFGRD1,NOEL,NPT,LAYER,KSPT,JSTEP,KINC)
      INCLUDE 'ABA_PARAM.INC'
      CHARACTER*80 CMNAME
      DIMENSION STRESS(NTENS),STATEV(NSTATV),
     1 DDSDDE(NTENS,NTENS),DDSDDT(NTENS),DRPLDE(NTENS),
     2 STRAN(NTENS),DSTRAN(NTENS),TIME(2),PREDEF(1),DPRED(1),
     3 PROPS(NPROPS),COORDS(3),DROT(3,3),DFGRD0(3,3),DFGRD1(3,3),
     4 JSTEP(4)

      DIMENSION ELASSTRAN(NTENS),DTHERMSTRAN(NTENS),THERMSTRAN(NTENS),
     1 CHEMSTRAN(NTENS),DCHEMSTRAN(NTENS)

      DOUBLE PRECISION DOC_max,v_f,DOC,A,E,n,m,C,alpha_c,alpha_T,H_tot,
     1 R,rho_f,rho_r,rho_laminate,E_lf,E_tf,G12_f,G23_f,NU12_f,a_lf,
     2 a_tf,E_r_glass,E_r_glassT,E_r_rub,NU_r_glass,NU_r_rub,a_glass,
     3 a_rub,y_a,Cm,sigma_m,Tg_0,Tg_inf,LAMBDA,DOC_old,CureRate,Tg,
     4 E_r,NU_r,G_r,a_r,y_r,E1,E2,E3,G12,G13,G23,NU_12,NU_13,NU_23,
     5 NU_21,NU_31,NU_32,DELTA,a_l,a_t,y_l,y_t,DOC_initial,TEMP_initial
      INTEGER I,J
      PARAMETER (ZERO=0.0D0, ONE=1.0D0, TWO=2.0D0)
!====================Manual input of DOC_max and laminate v_f=====================!
      DOC_max = 0.9999        !Set maximum DOC
      v_f=0.54                !Fibre volume fraction of the laminate
!==============Obtaining state variables 1-19 from previous increment=============!
      DO I=1,NTENS
       ELASSTRAN(I) = STATEV(I)
       THERMSTRAN(I) = STATEV(I+NTENS)
       CHEMSTRAN(I) = STATEV(I+TWO*NTENS)
      ENDDO
      DOC=STATEV(20)
!===========Cure kinetic parameters, based on Airstone 780E/785H resin===========!
      A=681085.0                !Pre-exponential Arrhenius factor [s^-1]
      E=59291.0                 !Activation energy [J/mol^-1]
      n=1.67                    !Reaction order [-]
      m=0.12                    !Reaction order [-]
      C=47.7                    ![-]
      alpha_c=0.77              ![-]
      alpha_T=1.60D-3           ![degC^-1]
      H_tot=434.0D3             ![J*kg^-1]
      R=8.3145                  !Universal gas constant [J K-^1 mol-^1]
! ===================Material parameters of constituents=========================!
      !---Glass fibre---!
      !Mechanical
      E_lf=73.1D9               !Modulus glass fibre longitudinal direction [Pa]
      E_tf=73.1D9               !Modulus glass fibre transverse direction [Pa]
      G12_f=30.0D9              !Modulus fibre 12-direction [Pa]
      G23_f=30.0D9              !Modulus fibre 23-direction [Pa]
      NU12_f=0.22               !Poisson's ratio of fibre in 12-direction [-]
      !Thermal
      a_lf=5.0D-6               !CTE in longitudinal direction [1/degC]
      a_tf=5.0D-6               !CTE in transverse direction [1/degC]

      !---Epoxy resin---!
      !Mechanical
```

```
      E_r_glass=4.61D9          !Modulus resin at glassy state [Pa]
      E_r_glassT=-0.012D9       !Temp. dependency modulus at glassy state [Pa/degC]
      E_r_rub=0.04D9            !Modulus resin at rubbery state [Pa]
      NU_r_glass=0.35           !Poisson's ratio resin at glassy state [-]
      NU_r_rub=0.49999          !Poisson's ratio resin at rubbery state [-]

      !Thermal expansion
      a_glass=6.0D-5            !CTE resin at glassy state [1/degC]
      a_rub=1.7D-4              !CTE resin at rubbery state [1/degC]

      !Chemical linear strain due to shrinkage
      y_a=1.9D-2                !Linear shrinkage of resin [-]

      !Other parameters
      Cm=0.4                    !Breadth of transition [1/degC]
      sigma_m=10.2              !Temperature shift of transition [degC]

      !Glass transition temperature parameters
      Tg_0=-55.0                !Minimum Tg of epoxy resin [degC]
      Tg_inf=89.0               !Maximum Tg of epoxy resin [degC]
      LAMBDA=0.476              !Fitting parameter [-]

      !Evolution of Glass transition temperature (DiBenedetto Eq.)
      Tg=Tg_0+((Tg_inf-Tg_0)*LAMBDA*DOC)/(1-(1-LAMBDA)*DOC)

      !Mechanical property evolutions throughout cure development
      E_r= E_r_rub + (E_r_glass+(E_r_glassT*TEMP)-E_r_rub)/
     &               (1+exp(Cm*(TEMP-Tg-sigma_m)))   !Resin modulus [MPa]
      NU_r=NU_r_rub + (NU_r_glass-NU_r_rub)/
     &                (1+exp(Cm*(TEMP-Tg-sigma_m)))  !Resin Poisson's ratio [-]
      G_r=E_r/(2*(1+NU_r))                           !Resin shear modulus [MPa]

!===========Property calculation of composite (transversely isotropic)============!
      !------------Mechanical (transversely isotropic)------!
      E1=v_f*E_lf + (1-v_f)*E_r           !Young's modulus in 1-direction [Pa]
      E2=E_r/(1-sqrt(v_f)*(1-(E_r/E_tf))) !Young's modulus in 2-direction [Pa]
      E3=E2                               !Young's modulus in 3-direction [Pa]

      G12=G_r/(1-sqrt(v_f)*(1-(G_r/G12_f))) !Shear modulus in 12-direction [Pa]
      G13=G12                               !Shear modulus in 13-direction [Pa]
      G23=G_r/(1-sqrt(v_f)*(1-(G_r/G23_f))) !Shear modulus in 13-direction [Pa]

      NU_12=v_f*NU12_f + (1-v_f)*NU_r     !Poisson's ratio in 12-direction [-]
      NU_13=NU_12                         !Poisson's ratio in 13-direction [-]
      NU_23=(E2/(2*G23))-1                !Poisson's ratio in 23-direction [-]

      NU_21=(E2/E1)*NU_12                 !Poisson's ratio in 21-direction [-]
      NU_31=(E3/E1)*NU_13                 !Poisson's ratio in 31-direction [-]
      NU_32=(E3/E2)*NU_23                 !Poisson's ratio in 32-direction [-]

      DELTA=ONE-NU_12*NU_21-NU_13*NU_31-NU_23*NU_32
     &         -NU_12*NU_23*NU_31-NU_21*NU_32*NU_13

!================Resin material parameters evolution models=====================!
      !Calculation curing rate with autocatalytic kinetic model (1st T in kelvin!)
      CureRate = (A*exp(-E/(R*(TEMP+273.15))))/
     &           (1+exp(C*(DOC-alpha_c-alpha_T*(TEMP))))
     &           *(1-DOC)**n * DOC**m
      !Updating DOC for next increment
      DOC_new = DOC + CureRate*DTIME

```

```
166       !When new DOC is exceeding DOC_max, DOC_max is used, CureRate is terminated
167       IF (DOC_new .gt. DOC_max) THEN
168         DOC_new = DOC_max
169         CureRate=0.0
170       END IF
171
172       !Thermal expansion evolutions throughout cure development [1/degC]
173       a_r=a_rub + (a_glass - a_rub)/(1+exp(Cm*(TEMP-Tg-sigma_m)))
174
175       !Incremental Chemical shrinkage of the resin due to DOC development
176       y_r=y_a*(DOC_new-DOC)
177
178       !----------------Thermal expansion--------------!
179       a_l=(((1-v_f)*E_r*a_r)+v_f*E_lf*a_lf)/((1-v_f)*E_r+v_f*E_lf)!CTE_l [1/degC]
180       a_t=(1-v_f)*a_r + v_f*a_tf + (1-v_f)*a_r*NU_r
181      &                + NU12_f*a_lf*v_f-NU_12*a_l                !CTE_t [1/degC]
182
183       !---------------Chemical shrinkage--------------!
184       y_l=(((1-v_f)*E_r*y_r))/((1-v_f)*E_r + v_f*E_lf)!Chemical shr. long. [-]
185       y_t=(1-v_f)*y_r +(1-v_f)*y_r*NU_r - NU12_f*y_l  !Chemical shr. transv. [-]
186
187       !Create empty stiffness matrix
188       DO I=1,NTENS
189        DO J=1,NTENS
190        DDSDDE(I,J)=ZERO
191        ENDDO
192       ENDDO
193       !The following lines define the 12 different entities of the stiffness matrix
194       !for an transversely isotropic linear elastic material.
195       !(Mechanics of Anisotropic Materials, Skrzypek2015)
196       DDSDDE(1,1)=((ONE-NU_23*NU_32)/DELTA)*E1
197       DDSDDE(1,2)=((NU_12+NU_13*NU_32)/DELTA)*E2
198       DDSDDE(1,3)=((NU_13+NU_12*NU_23)/DELTA)*E3
199       DDSDDE(2,1)=DDSDDE(1,2)
200       DDSDDE(2,2)=((ONE-NU_13*NU_31)/DELTA)*E2
201       DDSDDE(2,3)=((NU_23+NU_21*NU_13)/DELTA)*E3
202       DDSDDE(3,1)=DDSDDE(1,3)
203       DDSDDE(3,2)=DDSDDE(2,3)
204       DDSDDE(3,3)=((ONE-NU_12*NU_21)/DELTA)*E3
205       DDSDDE(4,4)=G12
206       DDSDDE(5,5)=G13
207       DDSDDE(6,6)=G23
208       !Define Thermal Strain tensor for current increment
209       DTHERMSTRAN(1)=a_l*DTEMP
210       DTHERMSTRAN(2)=a_t*DTEMP
211       DTHERMSTRAN(3)=DTHERMSTRAN(2)
212       DO J=NDI+1,NTENS
213        DTHERMSTRAN(J)=ZERO
214       ENDDO
215
216       !Define Incremental chemical strain tensor for current increment
217       DCHEMSTRAN(1)=-y_l
218       DCHEMSTRAN(2)=-y_t
219       DCHEMSTRAN(3)=DCHEMSTRAN(2)
220       DO J=NDI+1,NTENS
221        DCHEMSTRAN(J)=ZERO
222       ENDDO
223
224       !Define the new stress tensor by using the previous calculated stiffness
225       ! entity with the corresponding stress vector and strain vector entity.
226       DO I=1,NTENS
```

```
227         DO J=1,NTENS
228          STRESS(J)=STRESS(J)+DDSDDE(J,I)*(DSTRAN(I)-
229       &             (DTHERMSTRAN(I)+DCHEMSTRAN(I)))
230         ENDDO
231        !Sum incremental elastic and thermal strains in total strain arrays
232         ELASSTRAN(I) = ELASSTRAN(I) + (DSTRAN(I)-(DTHERMSTRAN(I)+DCHEMSTRAN(I)))
233         THERMSTRAN(I) = THERMSTRAN(I) + DTHERMSTRAN(I)
234         CHEMSTRAN(I) = CHEMSTRAN(I) + DCHEMSTRAN(I)
235        ENDDO
236
237        !Save Elastic, thermal and chemical strain for next increment.
238        DO I=1,NTENS
239         STATEV(I) = ELASSTRAN(I)
240         STATEV(I+NTENS) = THERMSTRAN(I)
241         STATEV(I+TWO*NTENS) = CHEMSTRAN(I)
242        ENDDO
243        !Save new DOC, CureRate,Tg for next increment
244        STATEV(19)=DOC             !Needed for current increment as DOC in UMATHT
245        STATEV(20)=DOC_new         !Needed for next increment as DOC_old
246        STATEV(21)=CureRate        !Needed to export for heat development in UMATHT
247        STATEV(22)=Tg              !Needed to export the Tg for equations in UMATHT
248        RETURN
249        END
250
251        SUBROUTINE UMAT_RESIN(STRESS,STATEV,DDSDDE,SSE,SPD,SCD,
252       1 RPL,DDSDDT,DRPLDE,DRPLDT,
253       2 STRAN,DSTRAN,TIME,DTIME,TEMP,DTEMP,PREDEF,DPRED,CMNAME,
254       3 NDI,NSHR,NTENS,NSTATV,PROPS,NPROPS,COORDS,DROT,PNEWDT,
255       4 CELENT,DFGRD0,DFGRD1,NOEL,NPT,LAYER,KSPT,JSTEP,KINC)
256        INCLUDE 'ABA_PARAM.INC'
257        CHARACTER*80 CMNAME
258        DIMENSION STRESS(NTENS),STATEV(NSTATV),
259       1 DDSDDE(NTENS,NTENS),DDSDDT(NTENS),DRPLDE(NTENS),
260       2 STRAN(NTENS),DSTRAN(NTENS),TIME(2),PREDEF(1),DPRED(1),
261       3 PROPS(NPROPS),COORDS(3),DROT(3,3),DFGRD0(3,3),DFGRD1(3,3),
262       4 JSTEP(4)
263
264        DIMENSION ELASSTRAN(NTENS),DTHERMSTRAN(NTENS),THERMSTRAN(NTENS),
265       1 CHEMSTRAN(NTENS),DCHEMSTRAN(NTENS)
266
267        DOUBLE PRECISION DOC_max,v_f,DOC,A,E,n,m,C,alpha_c,alpha_T,H_tot,
268       1 R,rho_f,rho_r,rho_laminate,E_lf,E_tf,G12_f,G23_f,NU12_f,a_lf,
269       2 a_tf,E_r_glass,E_r_glassT,E_r_rub,NU_r_glass,NU_r_rub,a_glass,
270       3 a_rub,y_a,Cm,sigma_m,Tg_0,Tg_inf,LAMBDA,DOC_old,CureRate,Tg,
271       4 E_r,NU_r,G_r,a_r,y_r,E1,E2,E3,G12,G13,G23,NU_12,NU_13,NU_23,
272       5 NU_21,NU_31,NU_32,DELTA,a_l,a_t,y_l,y_t,DOC_initial,TEMP_initial
273        INTEGER I,J
274        PARAMETER (ZERO=0.0D0, ONE=1.0D0, TWO=2.0D0, THREE=3.0D0)
275 !=====================Manual input of DOC_max and laminate v_f====================!
276        DOC_max = 0.9999        !Set maximum DOC
277 !==============Obtaining state variables 1-19 from previous increment============!
278        DO I=1,NTENS
279         ELASSTRAN(I) = STATEV(I)
280         THERMSTRAN(I) = STATEV(I+NTENS)
281         CHEMSTRAN(I) = STATEV(I+TWO*NTENS)
282        ENDDO
283        DOC=STATEV(20)
284        !Cure kinetic parameters, based on Airstone 780E/785H resin
285        A=681085.0              !Pre-exponential Arrhenius factor [s^-1]
286        E=59291.0               !Activation energy [J/mol^-1]
287        n=1.67                  !Reaction order [-]
```

```
      m=0.12                  !Reaction order [-]
      C=47.7                  ![-]
      alpha_c=0.77            ![-]
      alpha_T=1.60D-3         ![K^-1]
      H_tot=434.0D3           ![J*kg^-1]
      R=8.3144                 !Universal gas constant [J K-^1 mol-^1]
!====================Material parameters of constituents=========================!
      !---Epoxy resin---!
      !Mechanical
      E_r_glass=4.61D9        !Modulus resin at glassy state [Pa]
      E_r_glassT=-0.012D9     !Temp. dependency modulus at glassy state [Pa/degC]
      E_r_rub=0.04D9          !Modulus resin at rubbery state [Pa]
      NU_r_glass=0.35         !Poisson's ratio resin at glassy state [-]
      NU_r_rub=0.49999        !Poisson's ratio resin at rubbery state [-]

      !Thermal expansion
      a_glass=6.0D-5          !CTE resin at glassy state [1/degC]
      a_rub=1.7D-4            !CTE resin at rubbery state [1/degC]

      !Chemical linear strain due to shrinkage
      y_a=1.9D-2              !Linear shrinkage of resin [-]

      !Others
      Cm=0.4                  !Breadth of transition [1/degC]
      sigma_m=10.2            !Temperature shift of transition [degC]

      !Glass transition temperature parameters
      Tg_0=-55.0              !Minimum Tg of epoxy resin [degC]
      Tg_inf=89.0             !Maximum Tg of epoxy resin [degC]
      LAMBDA=0.476            !Fitting parameter [-]

      !Evolution of Glass transition temperature (DiBenedetto Eq.)
      Tg=Tg_0+((Tg_inf-Tg_0)*LAMBDA*DOC)/(1-(1-LAMBDA)*DOC)

      !Mechanical property evolutions throughout cure development
      E_r= E_r_rub + (E_r_glass+(E_r_glassT*TEMP)-E_r_rub)/
     &               (1+exp(Cm*(TEMP-Tg-sigma_m))) !Resin modulus [Pa]
      NU_r=NU_r_rub + (NU_r_glass-NU_r_rub)/
     &                (1+exp(Cm*(TEMP-Tg-sigma_m)))!Resin Poisson's ratio [-]
!==================Property calculation of resin (isotropic)=====================!
      !Elastic properties
      EMOD=E_r
      ENU=NU_r
      EBULK3=EMOD/(ONE-TWO*ENU)
      EG2=EMOD/(ONE+ENU)
      EG=EG2/TWO
      EG3=THREE*EG
      ELAM=(EBULK3-EG2)/THREE
!====================Resin material parameters evolution models==================!
      !Calculation curing rate with autocatalytic kinetic model (1st T in kelvin!)
      CureRate = (A*exp(-E/(R*(TEMP+273.15))))/
     &           (1+exp(C*(DOC-alpha_c-alpha_T*(TEMP))))
     &           *(1-DOC)**n * DOC**m
      !Updating DOC for next increment
      DOC_new = DOC + CureRate*DTIME

      !When new DOC is exceeding DOC_max, DOC_max is used, CureRate is terminated
      IF (DOC_new .gt. DOC_max) THEN
        DOC_new = DOC_max
        CureRate=0.0
      END IF
```

```
349
350       !Thermal expansion evolutions throughout cure development [1/degC]
351       a_r=a_rub + (a_glass - a_rub)/(1+exp(Cm*(TEMP-Tg-sigma_m)))
352
353       !Incremental Chemical shrinkage of the resin due to DOC development
354       y_r=y_a*(DOC_new-DOC)
355
356       !Create empty stiffness matrix
357       DO I=1,NTENS
358        DO J=1,NTENS
359        DDSDDE(I,J)=ZERO
360        ENDDO
361       ENDDO
362
363       !Define Stiffness matrix
364       DO I=1, NDI
365        DO J=1, NDI
366         DDSDDE(J, I)=ELAM
367       END DO
368        DDSDDE(I, I)=EG2+ELAM
369       END DO
370       DO I=NDI+1, NTENS
371        DDSDDE(I ,I)=EG
372       END DO
373
374       !Define Thermal Strain tensor for this increment
375       DTHERMSTRAN(1)=a_r*DTEMP
376       DTHERMSTRAN(2)=DTHERMSTRAN(1)
377       DTHERMSTRAN(3)=DTHERMSTRAN(1)
378       DO J=NDI+1,NTENS
379        DTHERMSTRAN(J)=ZERO
380       ENDDO
381
382       !Define Incremental chemical strain tensor for this increment
383       DCHEMSTRAN(1)=-y_r
384       DCHEMSTRAN(2)=DCHEMSTRAN(1)
385       DCHEMSTRAN(3)=DCHEMSTRAN(1)
386       DO J=NDI+1,NTENS
387        DCHEMSTRAN(J)=ZERO
388       ENDDO
389
390       !Define the new stress tensor by using the previous calculated stiffness
391       !entity with the corresponding stress vector and strain vector entity.
392       DO I=1,NTENS
393        DO J=1,NTENS
394         STRESS(J)=STRESS(J)+DDSDDE(J,I)*(DSTRAN(I)-
395      &             (DTHERMSTRAN(I)+DCHEMSTRAN(I)))
396        ENDDO
397       !Sum incremental elastic and thermal strains in total strain arrays
398        ELASSTRAN(I) = ELASSTRAN(I) + (DSTRAN(I)-(DTHERMSTRAN(I)+DCHEMSTRAN(I)))
399        THERMSTRAN(I) = THERMSTRAN(I) + DTHERMSTRAN(I)
400        CHEMSTRAN(I) = CHEMSTRAN(I) + DCHEMSTRAN(I)
401       ENDDO
402
403       !Save Elastic, thermal and chemical strain for next increment.
404       DO I=1,NTENS
405        STATEV(I) = ELASSTRAN(I)
406        STATEV(I+NTENS) = THERMSTRAN(I)
407        STATEV(I+TWO*NTENS) = CHEMSTRAN(I)
408       ENDDO
409
```

```
410       !Save new DOC, CureRate,Tg for next increment
411       STATEV(19)=DOC          !Needed for current increment as DOC in UMATHT
412       STATEV(20)=DOC_new      !Needed for next increment as DOC_old
413       STATEV(21)=CureRate     !Needed to export for heat development in UMATHT
414       STATEV(22)=Tg           !Needed to export the Tg for equations in UMATHT
415       RETURN
416       END
417
418       SUBROUTINE DISP(U,KSTEP,KINC,TIME,NODE,NOEL,JDOF,COORDS)
419       INCLUDE 'ABA_PARAM.INC'
420       DIMENSION U(3),TIME(3),COORDS(3)
421       DOUBLE PRECISION T0,T1,Dt1,r1,T2,Dt2,r2,r3
422 !=========================Input variables=========================================!
423       T0=23                   !Predefined Temp. (Equal to CAE model init. Temp.)
424       !First dwell parameters
425       T1=70.0                 !Temperature First dwell [degC]
426       Dt1=240                 !Duration of First dwell [min]
427       r1=0.3                  !Heating rate [degC/min]
428       !Cooldown parameter
429       rc=0.5                  !Cooling rate [degC/min]
430 !=======================Parameter recalculation==================================!
431       !Recalculate dwell times to seconds
432       Dt1 = Dt1*60.0          ![s]
433       Dt2 = Dt2*60.0          ![s]
434       !Recalculate heating rate to seconds
435       r1=r1/60                !Rate 1, [degC/s]
436       r2=r2/60                !Rate 2, [degC/s]
437       rc=rc/60                !Rate 3, [degC/s]
438       !Recalculate Temp's and rates to time durations
439       ra1=(T1-T0)/r1
440       rac=(T1-T0)/rc
441       !Cure cycle definition
442       IF (TIME(2) .le. ra1) THEN
443        U(1)=T0+r1*TIME(2)
444       ELSE IF (TIME(2) .gt. ra1 .and. TIME(2) .le. ra1+Dt1) THEN
445        U(1)=T1
446       ELSE IF (TIME(2) .gt. ra1+Dt1 .and. TIME(2) .le. ra1+Dt1+rac THEN
447        U(1)=T1 - rc*(TIME(2)-Dt1-ra1)
448       ELSE IF (TIME(2) .gt. ra1+Dt1+rac) THEN
449        U(1)=T0
450       END IF
451       RETURN
452       END
453
454       SUBROUTINE FILM(H,SINK,TEMP,KSTEP,KINC,TIME,NOEL,NPT,
455      1 COORDS,JLTYP,FIELD,NFIELD,SNAME,NODE,AREA)
456
457       INCLUDE 'ABA_PARAM.INC'
458       DIMENSION H(2),TIME(2),COORDS(3), FIELD(NFIELD)
459       CHARACTER*80 SNAME
460       DOUBLE PRECISION T0,T1,Dt1,r1,T2,Dt2,r2,r3
461 !==============================Input variables=====================================!
462       H(1)=13.7               !Convection coefficient [W/m or J s^1 m^1]
463       H(2)=0.0                !Rate of change convection coefficient wrt temp.
464       T0=23                   !Predefined Temp. (Equal to CAE model init. Temp.)
465       !First dwell parameters
466       T1=70.0                 !Temperature First dwell [degC]
467       Dt1=240                 !Duration of First dwell [min]
468       r1=0.3                  !Heating rate [degC/min]
469       !Cooldown parameter
470       rc=0.5                  !Cooling rate [degC/min]
```

```
!============================Parameter recalculation============================!
      !Recalculate dwell times to seconds
      Dt1 = Dt1*60            ![s]
      Dt2 = Dt2*60            ![s]
      !Recalculate heating rate to seconds
      r1=r1/60                !Rate 1, [degC/s]
      rc=rc/60                !Rate 3, [degC/s]
      !Recalculate Temp's and rates to time durations
      ra1=(T1-T0)/r1
      rac=(T1-T0)/rc
      !Cure cycle definition
      IF (TIME(2) .le. ra1) THEN
       SINK=T0+r1*TIME(2)
      ELSE IF (TIME(2) .gt. ra1 .and. TIME(2) .le. ra1+Dt1) THEN
       SINK=T1
      ELSE IF (TIME(2) .gt. ra1+Dt1 .and. TIME(2) .le.
     &        ra1+Dt1+rac) THEN
       SINK=T1 - rc*(TIME(2)-Dt1-ra1)
      ELSE IF (TIME(2) .gt. ra1+Dt1+rac) THEN
       SINK=T0
      END IF
      RETURN
      END

      SUBROUTINE UMATHT(U,DUDT,DUDG,FLUX,DFDT,DFDG,
     1 STATEV,TEMP,DTEMP,DTEMDX,TIME,DTIME,PREDEF,DPRED,
     2 CMNAME,NTGRD,NSTATV,PROPS,NPROPS,COORDS,PNEWDT,
     3 NOEL,NPT,LAYER,KSPT,KSTEP,KINC)

      INCLUDE 'ABA_PARAM.INC'
      CHARACTER*80 CMNAME
      IF (CMNAME(1:3) .EQ. 'PLY') THEN
      CALL UMATHT_PLY(U,DUDT,DUDG,FLUX,DFDT,DFDG,
     1 STATEV,TEMP,DTEMP,DTEMDX,TIME,DTIME,PREDEF,DPRED,
     2 CMNAME,NTGRD,NSTATV,PROPS,NPROPS,COORDS,PNEWDT,
     3 NOEL,NPT,LAYER,KSPT,KSTEP,KINC)

      ELSE IF(CMNAME(1:5) .EQ. 'RESIN') THEN
      CALL UMATHT_RESIN(U,DUDT,DUDG,FLUX,DFDT,DFDG,
     1 STATEV,TEMP,DTEMP,DTEMDX,TIME,DTIME,PREDEF,DPRED,
     2 CMNAME,NTGRD,NSTATV,PROPS,NPROPS,COORDS,PNEWDT,
     3 NOEL,NPT,LAYER,KSPT,KSTEP,KINC)

      END IF
      RETURN
      END

      SUBROUTINE UMATHT_PLY(U,DUDT,DUDG,FLUX,DFDT,DFDG,
     1 STATEV,TEMP,DTEMP,DTEMDX,TIME,DTIME,PREDEF,DPRED,
     2 CMNAME,NTGRD,NSTATV,PROPS,NPROPS,COORDS,PNEWDT,
     3 NOEL,NPT,LAYER,KSPT,KSTEP,KINC)

      INCLUDE 'ABA_PARAM.INC'
      CHARACTER*80 CMNAME
      DIMENSION DUDG(NTGRD),FLUX(NTGRD),DFDT(NTGRD),
     1 DFDG(NTGRD,NTGRD),STATEV(NSTATV),DTEMDX(NTGRD),
     2 TIME(2),PREDEF(1),DPRED(1),PROPS(NPROPS),COORDS(3)

      DOUBLE PRECISION DOC,CureRate,Tg,H_tot,v_f,Q,K(NTGRD),K_lf,K_tf,
     1 a_kr,b_kr,c_kr,d_kr,e_kr,f_kr,K_r,K11,K22,K33,A_fcp,B_fcp,A_rcp
     2 B_rcp,delta_rcp,C_rcp,sigma,rho_f,rho_r,w_f,Cp_f,Cp_r,Cp_c
```

```
      PARAMETER (ZERO=0.0D0, ONE=1.0D0, TWO=2.0D0)
      !Initialize STATEV.
      DOC = STATEV(19)        !Obtaining DOC from UMAT
      CureRate=STATEV(21)     !Obtaining CureRate from UMAT
      Tg=STATEV(22)           !Obtaining Tg from UMAT
      H_tot=434.0D3           !Reaction energy [J*kg^-1]
      v_f=0.54                !Assumed fibre volume fraction of the laminate
      !Heat generation source definition
      Q=(1-v_f)*H_tot*CureRate*DTIME
!===================Material Constants - Thermal conductivity=====================!
      !Fibre Material
      K_lf=1.03               !Longitudinal thermal conductivity fibre [W/(m degC)]
      K_tf=1.03               !Transverse thermal conductivity fibre [W/(m degC)]
      !Resin Material
      a_kr=0.0008             ![W/(m degC^2)]
      b_kr=-0.0011            ![W/(m degC^2)]
      c_kr=-0.0002            ![W/(m degC^2)]
      d_kr=-0.0937            ![W/(m degC)]
      e_kr=0.22               ![W/(m degC)]
      f_kr=0.12               ![W/(m degC)]
!===================Calculation orthotropic conductivity development==============!
      K_r=a_kr*TEMP*DOC**2 + b_kr*TEMP*DOC + c_kr*TEMP + d_kr*DOC**2 +
     &    e_kr*DOC + f_kr     !Resin conductivity
      K11=v_f*K_lf + (1-v_f)*K_r
      K22=v_f*K_r*(K_tf/K_r - 1) + K_r*(ONE/TWO - K_tf/(TWO*K_r))
     &          + K_r*(K_tf/K_r - ONE)*
     & sqrt(v_f**2-v_f+((K_tf/K_r + ONE)**2)/((TWO*K_tf/K_r - TWO)**2))
      K33=K22
      !Set orthotropic conductivity in array formation
      K(1)=K11
      K(2)=K22
      K(3)=K33
!=======================Material Constants - Specific heat=======================!
      !Fibre Material
      A_fcp=0.0014D3          ![J/(kg degC^2)]
      B_fcp=0.841D3           ![J/(kg degC)]
      !Resin Material
      A_rcp=0.0025D3          ![J/(kg degC^2)]
      B_rcp=1.80D3            ![J/(kg degC)]
      delta_rcp=-0.25D3       ![J/(kg degC)]
      C_rcp=1.10              ![1/degC]
      sigma=16.5              ![degC]
      rho_f=2580.0            ![kg/m^3]
      rho_r=1105.0            ![kg/m^3]
!======================Calculation specific heat development====================!
      w_f= (v_f*rho_f)/(v_f*rho_f + (1-v_f)*rho_r)
      Cp_f=A_fcp*TEMP + B_fcp
      Cp_r=A_rcp*TEMP + B_rcp +
     &     (delta_rcp/(ONE+exp(C_rcp*(TEMP-Tg-sigma))))
      Cp_c=w_f*Cp_f + (1-w_f)*Cp_r
      DUDT = Cp_c             !Specific heat Composite
      DU = DUDT * DTEMP
      U = U + DU - Q
      !Define Heat flux vector
      DO i=1, NTGRD
       FLUX(i) = -K(i)*DTEMDX(i)
      END DO
      !Define variation of heat flux vector as conductivity vector
      DO i=1, NTGRD
       DFDG(i,i)=-K(i)
      END DO
```

```
      RETURN
      END

      SUBROUTINE UMATHT_RESIN(U,DUDT,DUDG,FLUX,DFDT,DFDG,
     1 STATEV,TEMP,DTEMP,DTEMDX,TIME,DTIME,PREDEF,DPRED,
     2 CMNAME,NTGRD,NSTATV,PROPS,NPROPS,COORDS,PNEWDT,
     3 NOEL,NPT,LAYER,KSPT,KSTEP,KINC)

      INCLUDE 'ABA_PARAM.INC'
      CHARACTER*80 CMNAME
      DIMENSION DUDG(NTGRD),FLUX(NTGRD),DFDT(NTGRD),
     1 DFDG(NTGRD,NTGRD),STATEV(NSTATV),DTEMDX(NTGRD),
     2 TIME(2),PREDEF(1),DPRED(1),PROPS(NPROPS),COORDS(3)

      DOUBLE PRECISION DOC,CureRate,Tg,H_tot,v_f,Q,K1,K_lf,K_tf,
     1 a_kr,b_kr,c_kr,d_kr,e_kr,f_kr,K_r,K11,K22,K33,A_fcp,B_fcp,A_rcp
     2 B_rcp,delta_rcp,C_rcp,sigma,rho_f,rho_r,w_f,Cp_f,Cp_r,Cp_c
      PARAMETER (ZERO=0.0D0, ONE=1.0D0, TWO=2.0D0)
      !Initialize STATEV.
      DOC = STATEV(19)         !Obtaining DOC from UMAT
      CureRate=STATEV(21)      !Obtaining CureRate from UMAT
      Tg=STATEV(22)            !Obtaining Tg from UMAT
      H_tot=434.0D3            !Reaction energy [J*kg^-1]
      !Heat generation source definition, for neat resin only
      Q=H_tot*CureRate*DTIME
!====================Material Constants - Thermal conductivity (isotropic)=========!
      !Resin Material
      a_kr=0.0008              ![W/(m degC^2)]
      b_kr=-0.0011             ![W/(m degC^2)]
      c_kr=-0.0002             ![W/(m degC^2)]
      d_kr=-0.0937             ![W/(m degC)]
      e_kr=0.22                ![W/(m degC)]
      f_kr=0.12                ![W/(m degC)]
!====================Calculation isotropic conductivity development================!
      K_r=a_kr*TEMP*DOC**2 + b_kr*TEMP*DOC + c_kr*TEMP + d_kr*DOC**2 +
     &    e_kr*DOC + f_kr
!======================Material Constants - Specific heat=========================!
      !Resin Material
      A_rcp=0.0025D3           ![J/(kg degC^2)]
      B_rcp=1.80D3             ![J/(kg degC)]
      delta_rcp=-0.25D3        ![J/(kg degC)]
      C_rcp=1.10               ![1/degC]
      sigma=16.5               ![degC]
!======================Calculation specific heat development======================!
      Cp_r=A_rcp*TEMP + B_rcp +
     &     (delta_rcp/(ONE+exp(C_rcp*(TEMP-Tg-sigma))))
      DUDT = Cp_r              !Specific heat resin
      DU = DUDT * DTEMP
      U = U + DU - Q
      !Define Heat flux vector
      DO i=1, NTGRD
       FLUX(i) = -K_r*DTEMDX(i)
      END DO
      !Define variation of heat flux vector as conductivity vector
      DO i=1, NTGRD
       DFDG(i,i)=-K_r
      END DO
      RETURN
      END
```

B

Definition of Output - Fortran Subroutine Code

SDV01 — Total effective strain - xx
SDV02 — Total effective strain - yy
SDV03 — Total effective strain - zz
SDV04 — Total effective strain - xy
SDV05 — Total effective strain - yz
SDV06 — Total effective strain - xz
SDV07 — Thermal strain - xx
SDV08 — Thermal strain - yy
SDV09 — Thermal strain - zz
SDV13 — Shrinkage strain - xx
SDV14 — Shrinkage strain - yy
SDV15 — Shrinkage strain - zz
SDV19 — DOC at the beginning of the increment
SDV20 — DOC at the end of the increment
SDV21 — Cure rate $(d\alpha/dt)$
SDV22 — Tg

C

Sensitivity Analysis - Output graphs

Within this appendix, the output graphs of the sensitivity analysis are presented. Figures C.1 and C.2 are the resulting interpolated DOC evolution data and the DOC evolution true error graphs for the isothermal cure cycles. In addition, figures C.3 to C.5 are the resulting interpolated DOC evolution data, the DOC evolution true error and the DOC evolution relative error for the dynamic cure cycle.

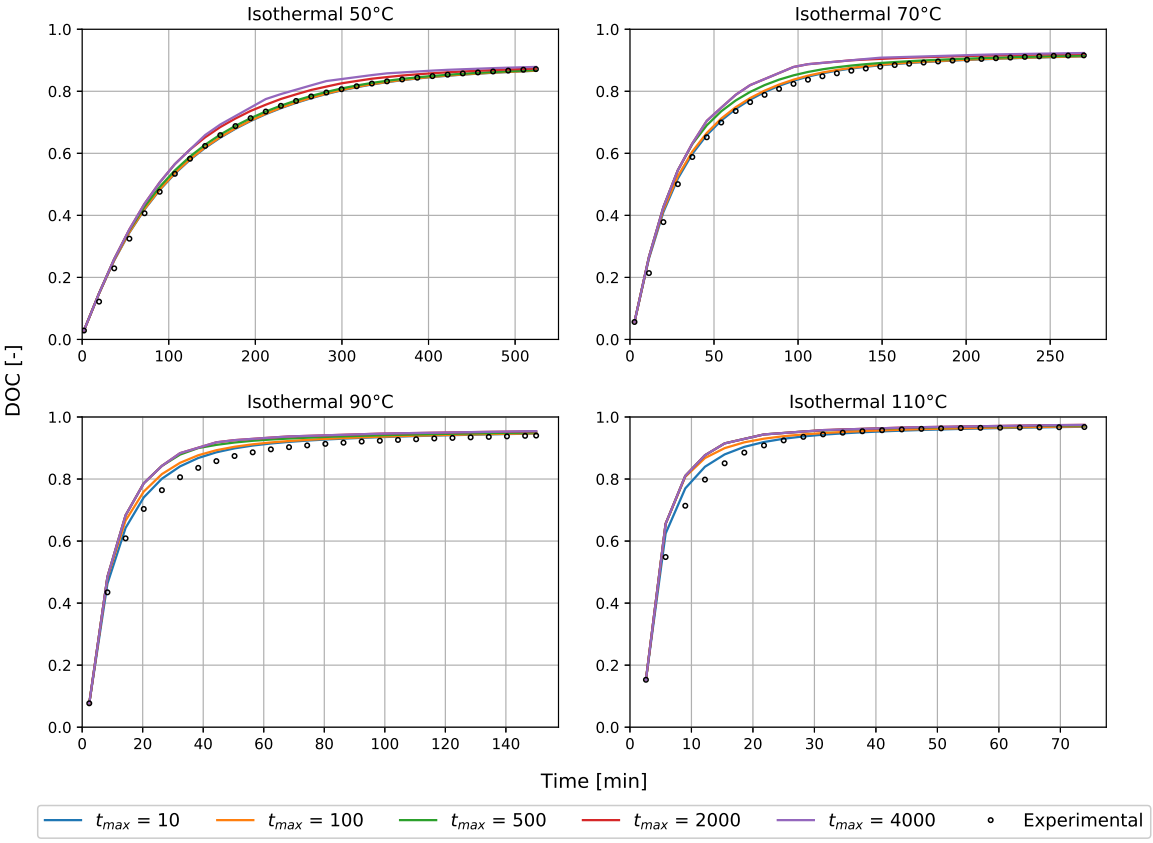

Figure C.1: DOC development, Numerical vs. Experimental (after interpolation) - Isothermal cycles with 50, 70, 90 and 110 °C

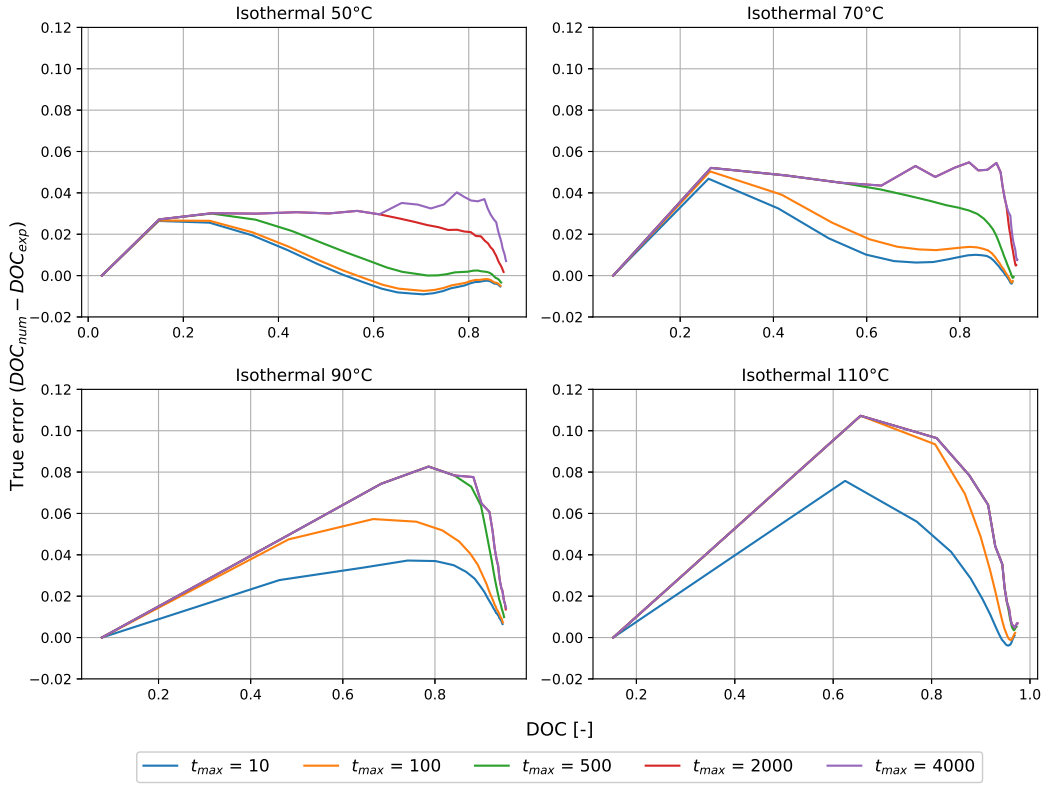

Figure C.2: True error - DOC development, Numerical vs. Experimental - Isothermal cycles with 50, 70, 90 and 110 °C

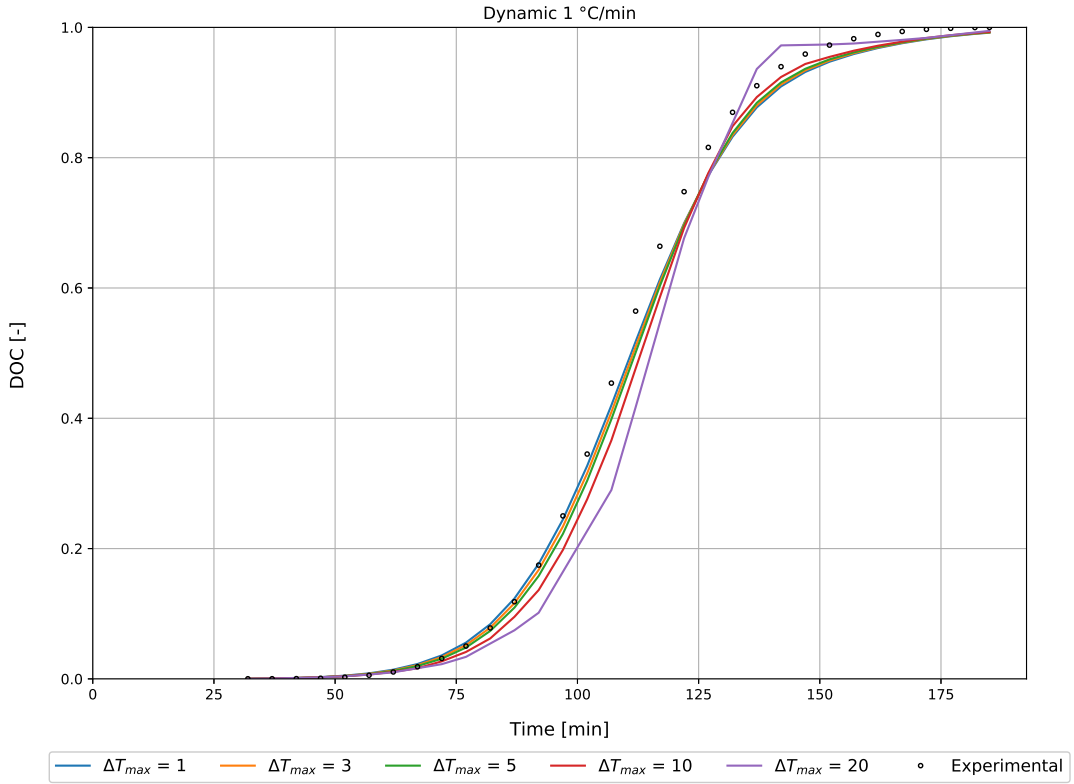

Figure C.3: DOC development, Numerical vs. Experimental (after interpolation) - Dynamic cycle with 1 °C/min

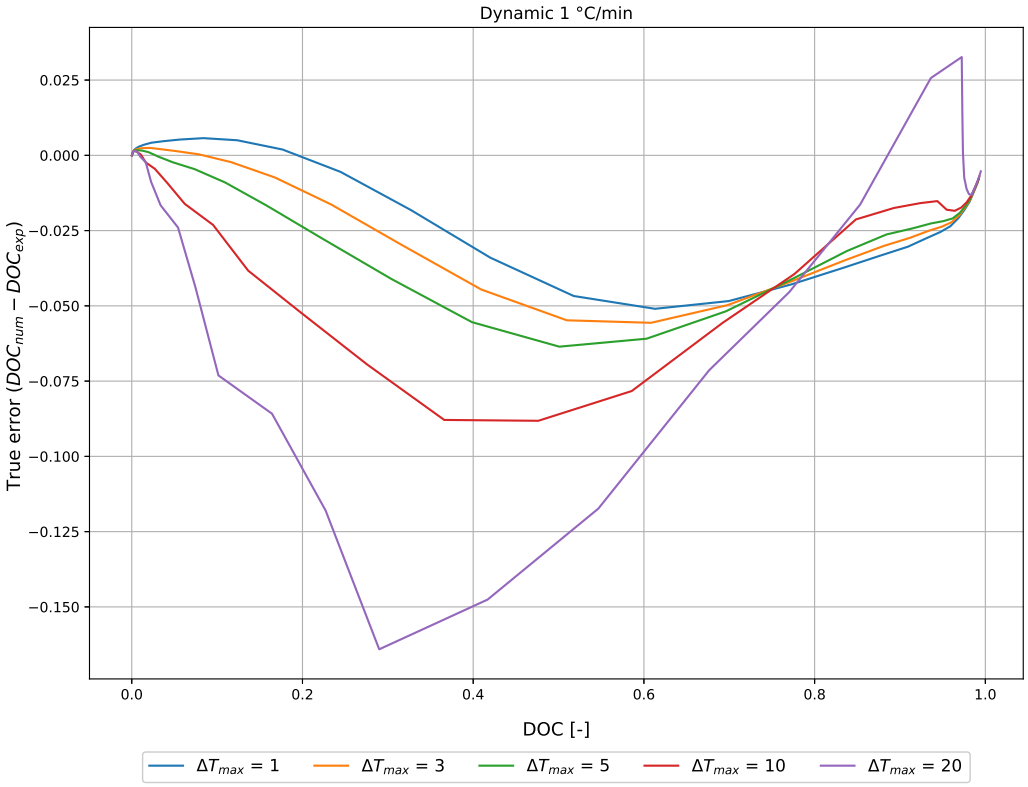

Figure C.4: True error - DOC development, Numerical vs. Experimental - Dynamic cycle with 1 °C/min

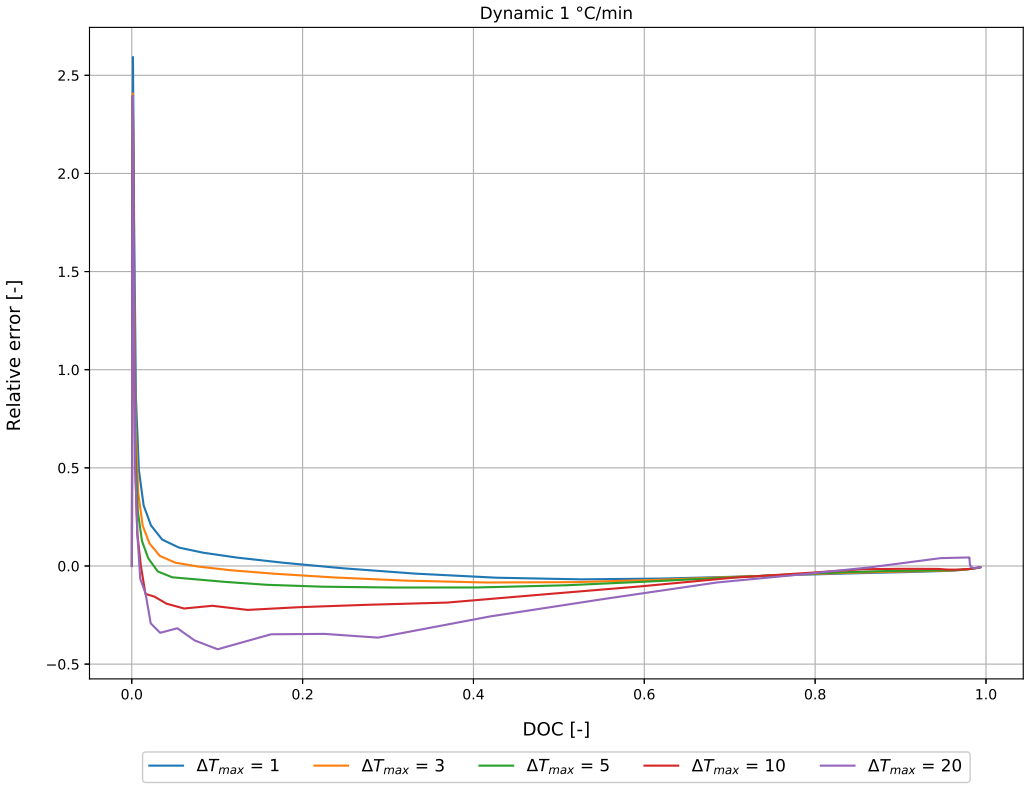

Figure C.5: Relative error - DOC development, Numerical vs. Experimental - Dynamic cycle with 1 °C/min

D

Verification Model - Output Graphs

This page intentionally left blank

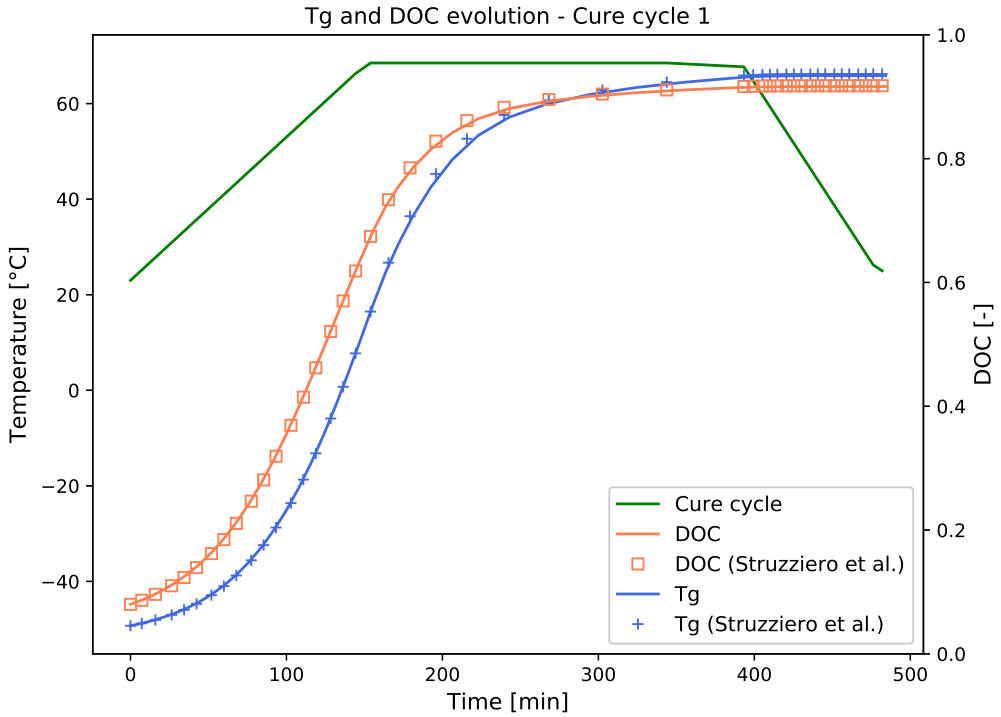

Figure D.1: Cure cycle 1: Development of the DOC and Tg within the 0° plies. Data for correlation obtained from [48]

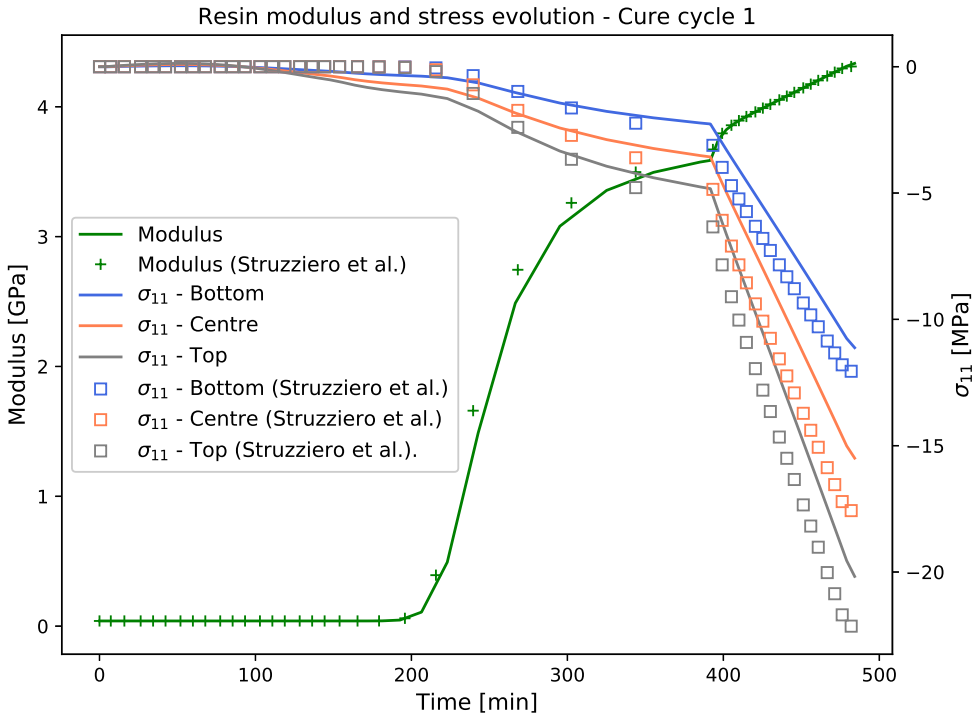

Figure D.2: Cure cycle 1: Development of the resin modulus and residual stress generation within the 0° plies. Data for correlation obtained from [48]

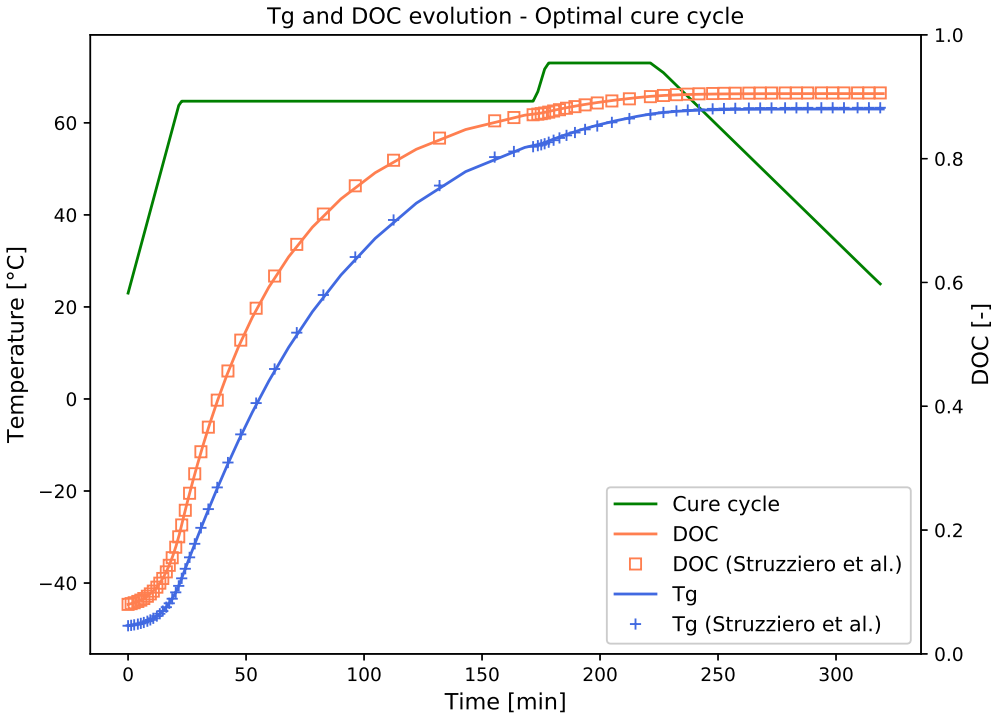

Figure D.3: Optimal cure cycle: Development of the DOC and Tg within the 0° plies. Data for correlation obtained from [48]

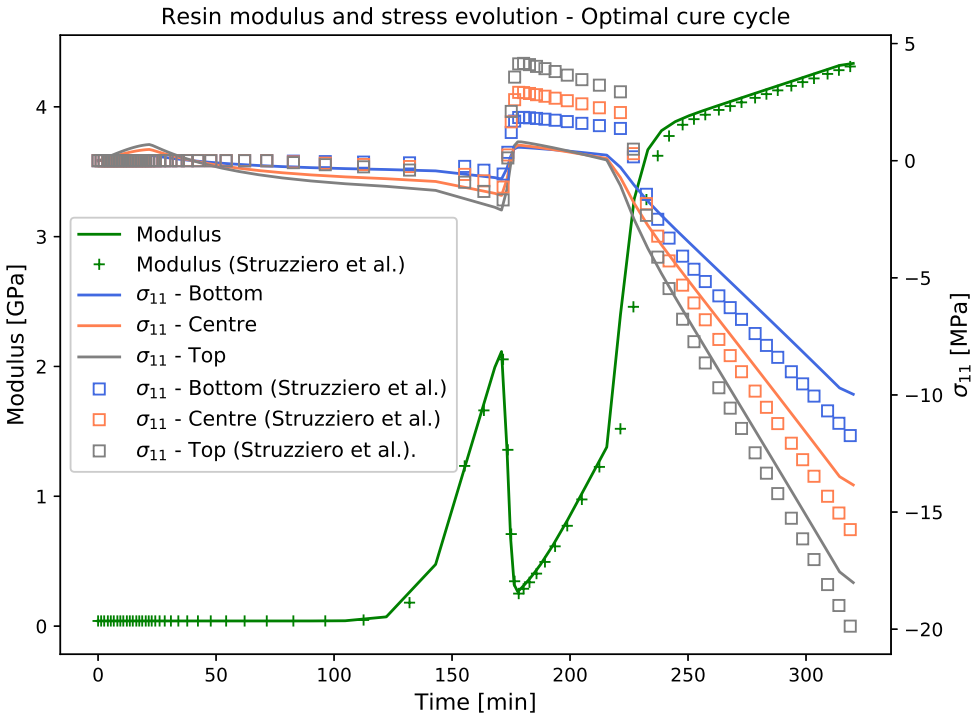

Figure D.4: Optimal cure cycle: Development of the resin modulus and residual stress generation within the 0° plies. Data for correlation obtained from [48]

E

Mesh Strategy - Ply Drop-off Model

Within this appendix, the mesh structure strategy of each ply drop-off model is given. As can be seen in figure E.1, four different mesh seed edge groups are implemented within the thin laminate model. For the thick laminate model, as shown in figure E.2, five different mesh seed edge groups are implemented. The subsequent steps of assigning mesh seeds and implement mesh elements for the thick laminate drop-off model and multiple drop-off model is identical to the thin laminate model, as shown in figures E.1 and E.3. As result of these standardized methods using different (biased) mesh seed edges, multiple mesh structures can be obtained for the mesh convergence studies.

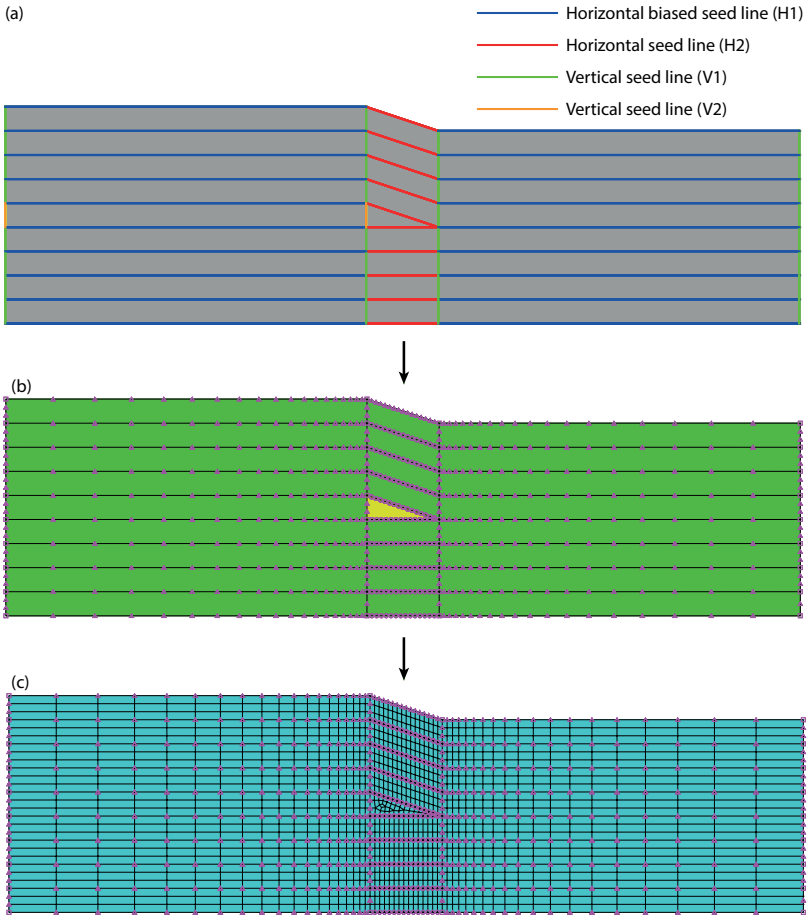

Figure E.1: Mesh strategy of thin laminate ply drop-off model. (a) Visualization of different mesh seed edges, (b) Assigning mesh seeds according to different element sizes and (c) Implementation of mesh elements

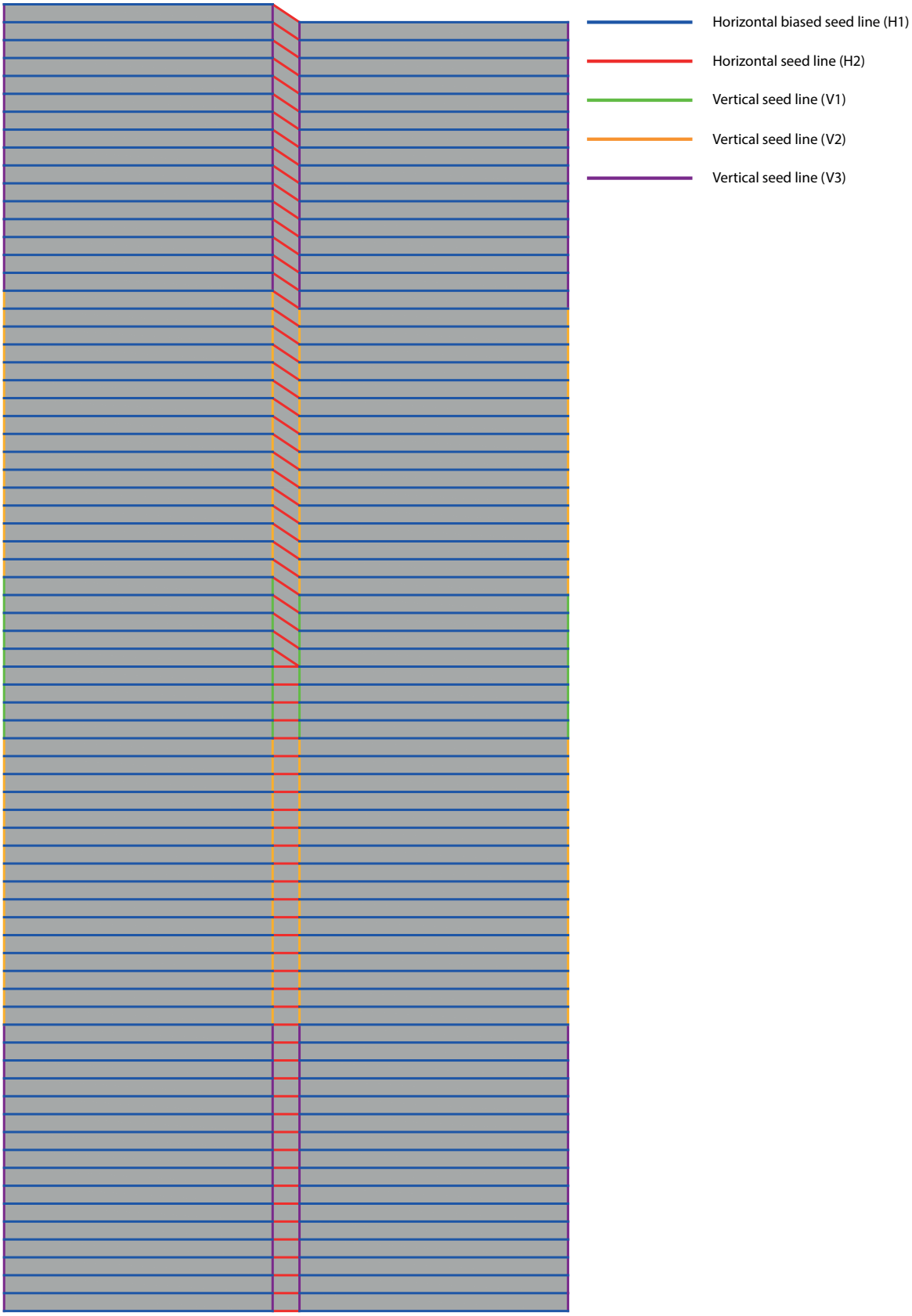

Figure E.2: Mesh strategy of thick laminate ply drop-off model. Visualization of different mesh seed edges

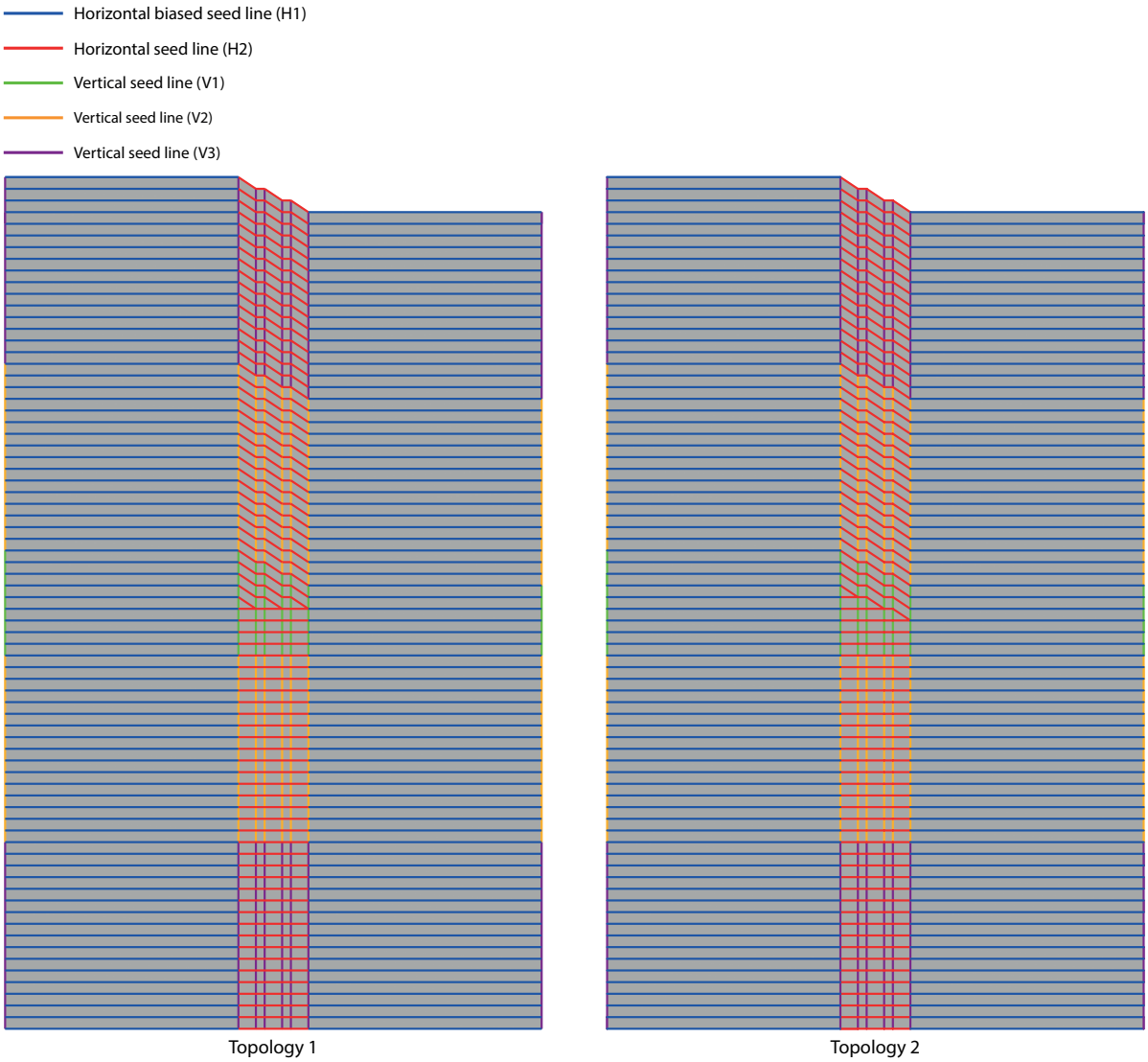

Figure E.3: Mesh strategy of thick laminate multiple ply drop-off model. Visualization of different mesh seed edges for both topologies

F

Resin Pocket Material Properties - Contour Plots

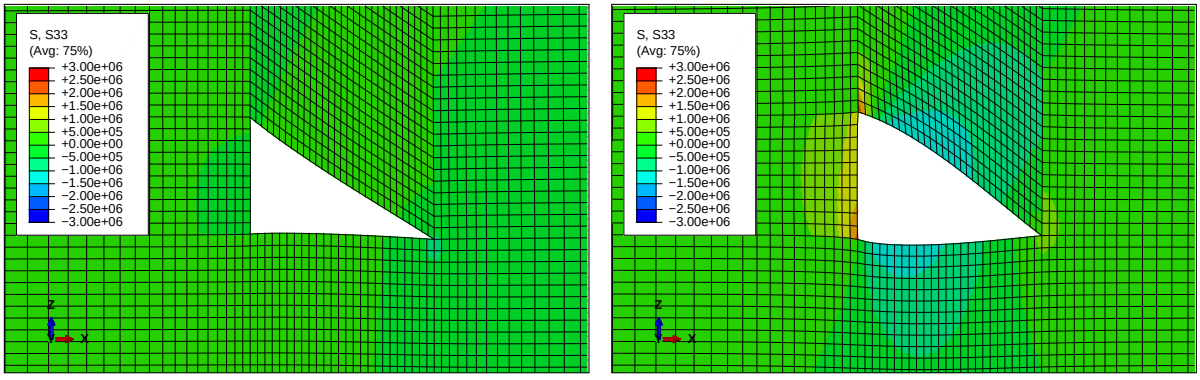

(a) Normal strain development

(b) Only thermal strain

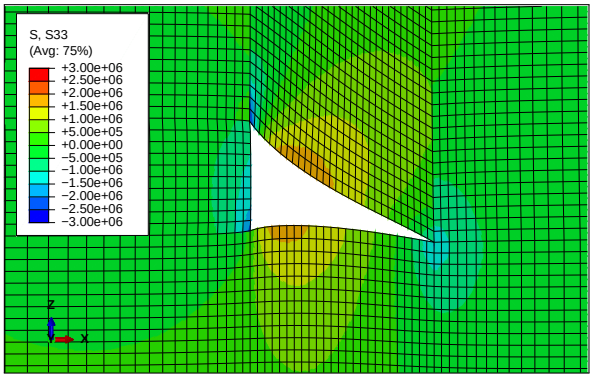

(c) Only chemical strain

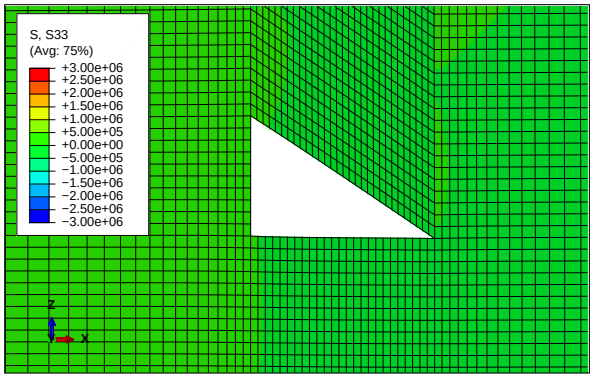

(d) Constant volume

Figure F.1: Out-of-plane stress contour plot as result of material property evolutions within resin pocket. Thin laminate ply drop-off model (a/b = 1/1.5). Time = 156 min (Start dwell), DOC = 0.7. For clarification a deformation scale factor of 10 is used and the resin pocket is hidden. Unit of contour limit values in Pascal. Note that no differences were observed between variation 4 and 5 at this observation point (constant volume and no resin modulus, respectively) and therefore the fifth plot has been left out

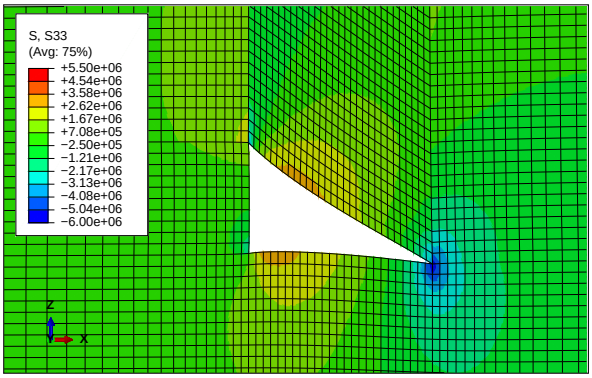

(a) Normal strain development

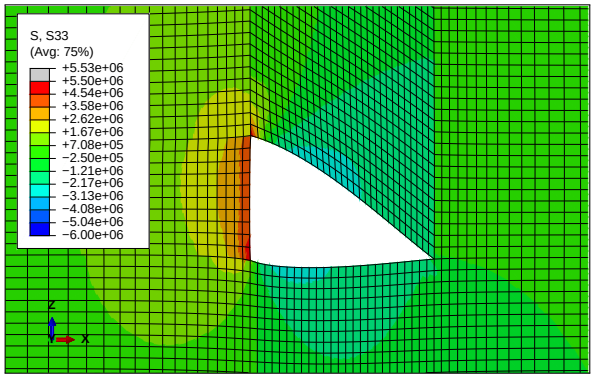

(b) Only thermal strain

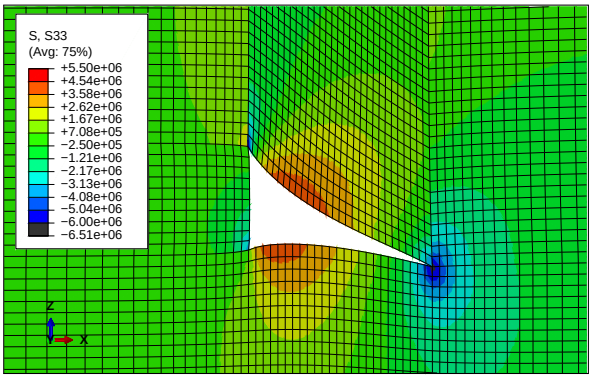

(c) Only chemical strain

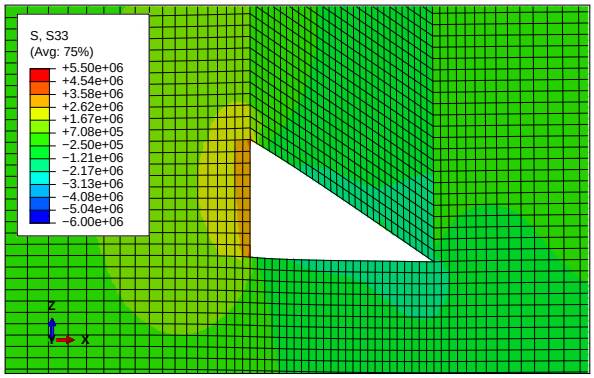

(d) Constant volume

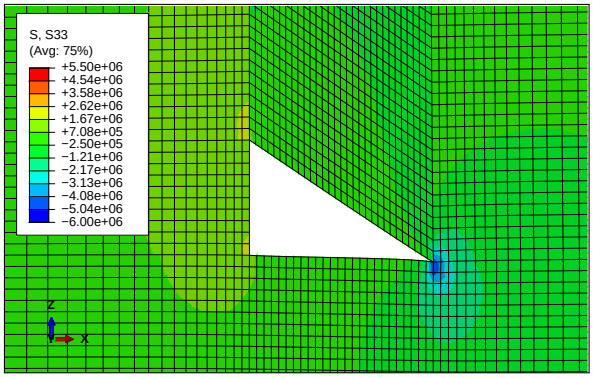

(e) No resin pocket modulus development

Figure F.2: Out-of-plane stress contour plot as result of material property evolutions within resin pocket. Thin laminate ply drop-off model (a/b = 1/1.5). Time = 396 min (End dwell), DOC = 0.92. For clarification a deformation scale factor of 10 is used and the resin pocket is hidden. Unit of contour limit values in Pascal

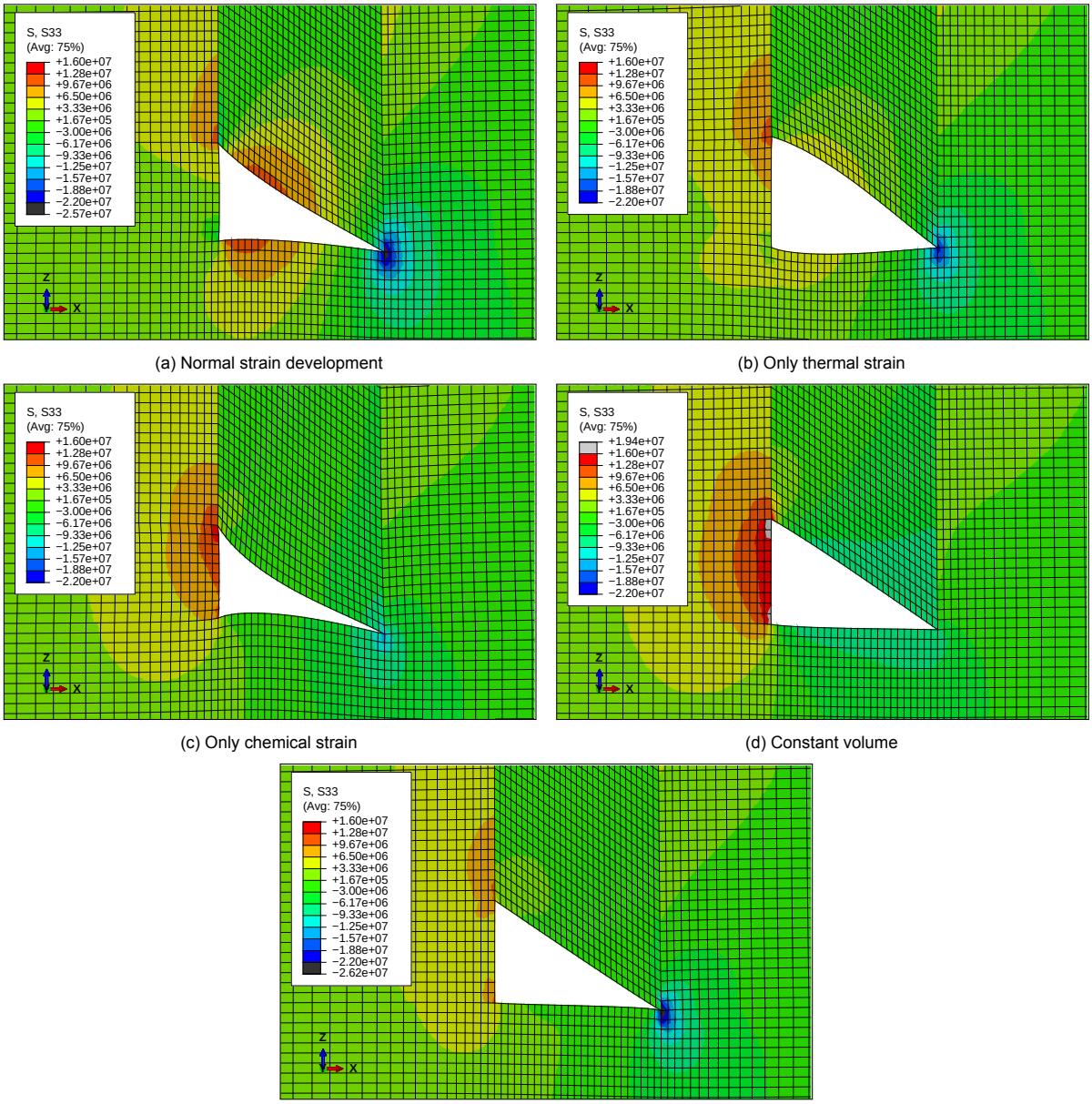

Figure F.3: Out-of-plane stress contour plot as result of material property evolutions within resin pocket. Thin laminate ply drop-off model (a/b = 1/1.5). Time = 490 min (End cycle), DOC = 0.92. For clarification a deformation scale factor of 10 is used and the resin pocket is hidden. Unit of contour limit values in Pascal

G

Influence of Process Parameters - Output Graphs

Within this appendix, the graphs for the Von Mises stress vs. time and vs. DOC within the resin pocket for all cure cycles is given. In addition, for each dwell temperature the output graphs for a single different cool down rate are given.

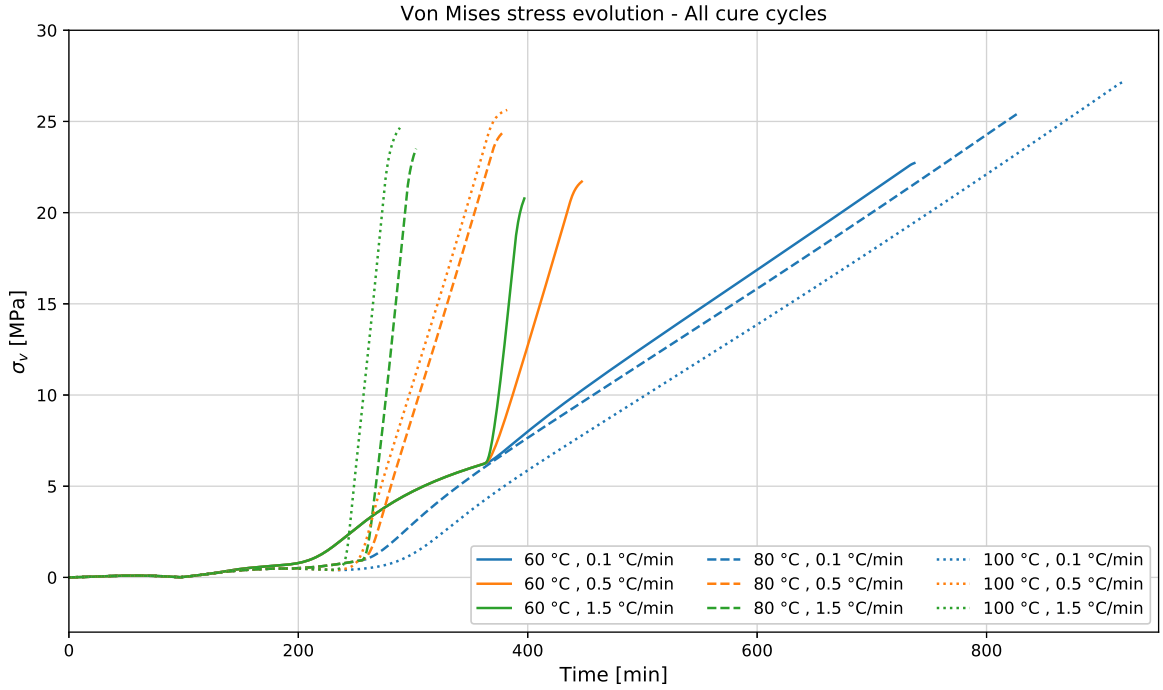

Figure G.1: Maximum Von Mises stress evolution within the pocket. All dwell temperatures and cool down rates

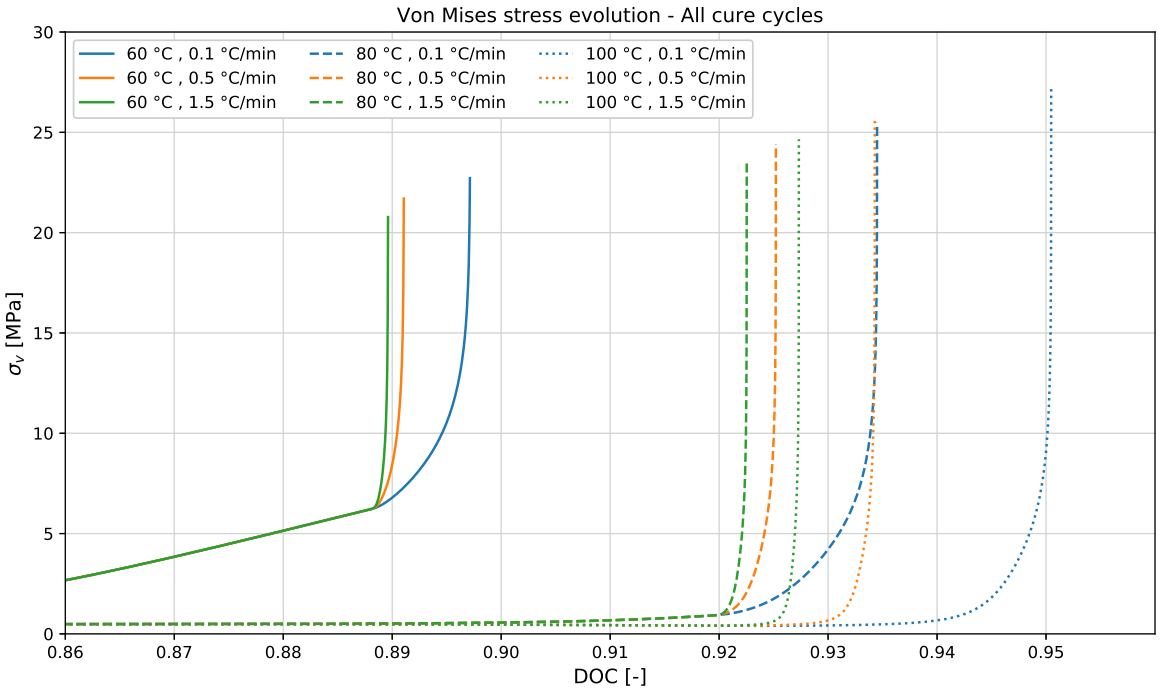

Figure G.2: Maximum Von Mises stress evolution vs. DOC within the pocket. All dwell temperatures and cool down rates

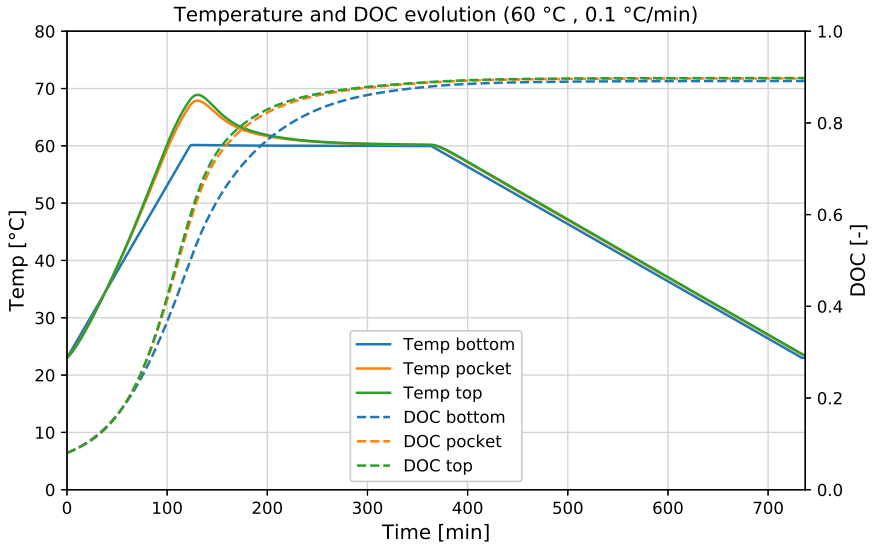

(a) Temperature and DOC evolution graph

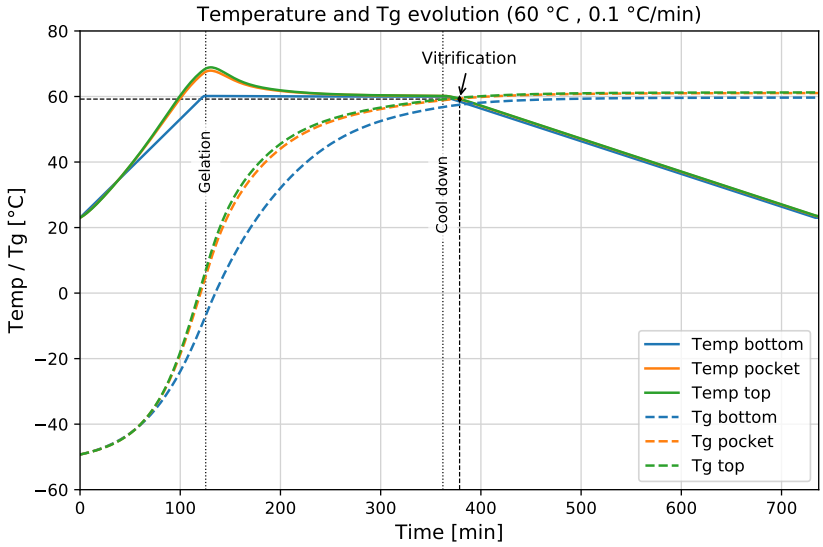

(b) Temperature and Tg evolution graph

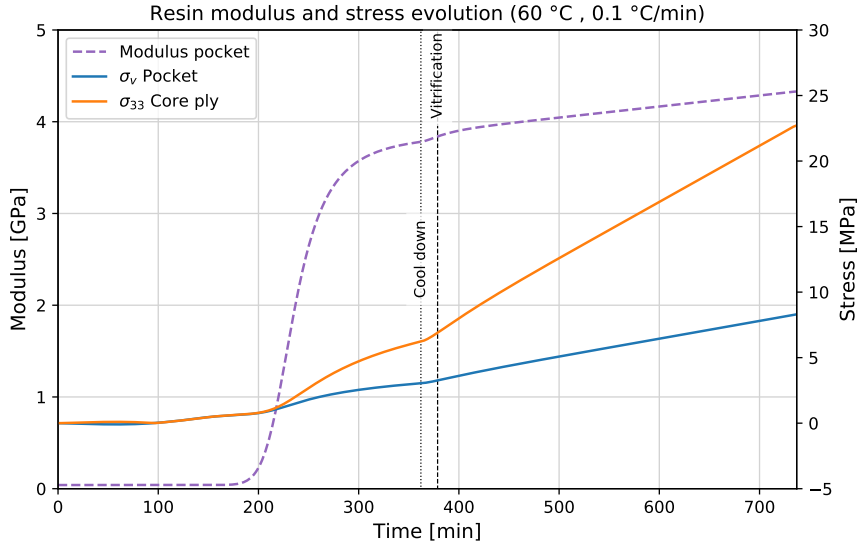

(c) Modulus and stress evolution graph

Figure G.3: Process influence output graphs. Dwell temp: 60 °C, Cool down rate: 0.1 °C/min

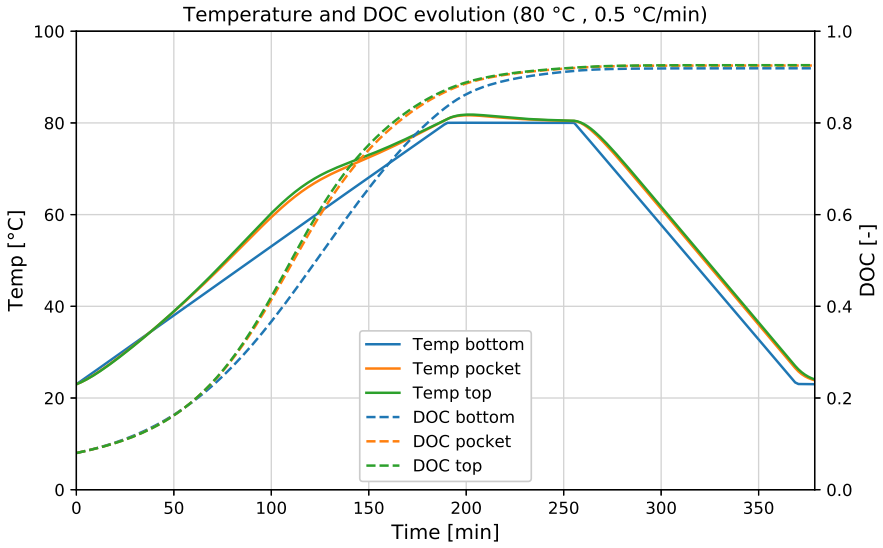

(a) Temperature and DOC evolution graph

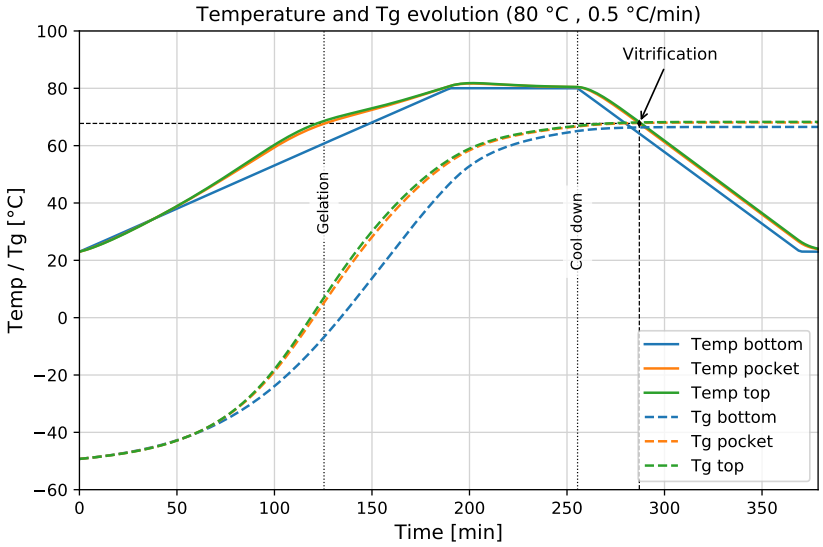

(b) Temperature and Tg evolution graph

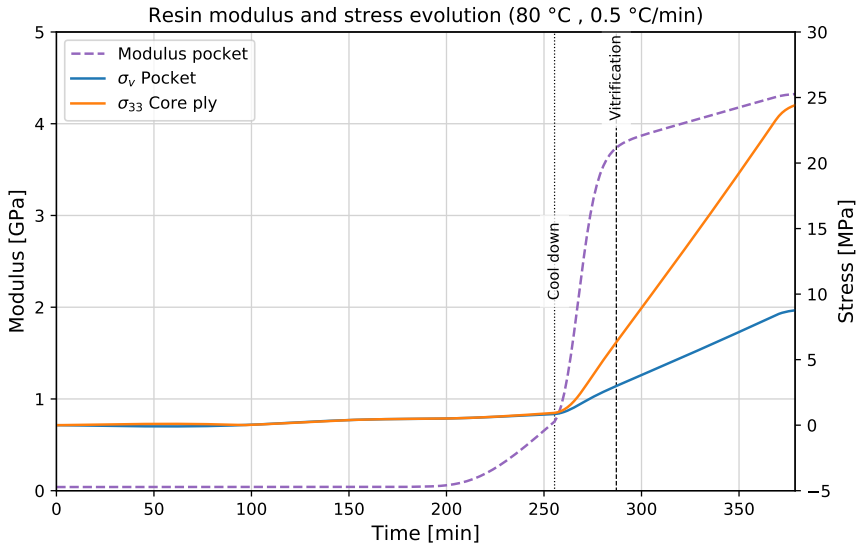

(c) Modulus and stress evolution graph

Figure G.4: Process influence output graphs. Dwell temp: 80 °C, Cool down rate: 0.5 °C/min

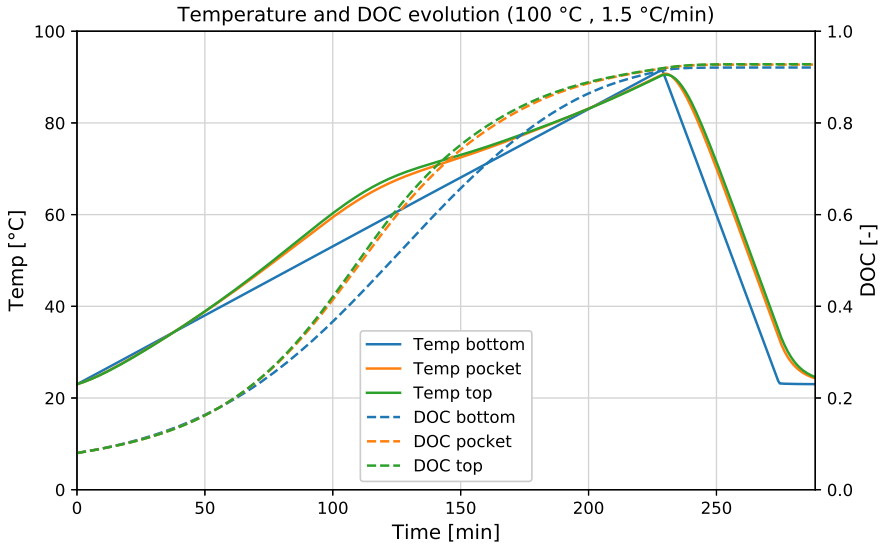

(a) Temperature and DOC evolution graph

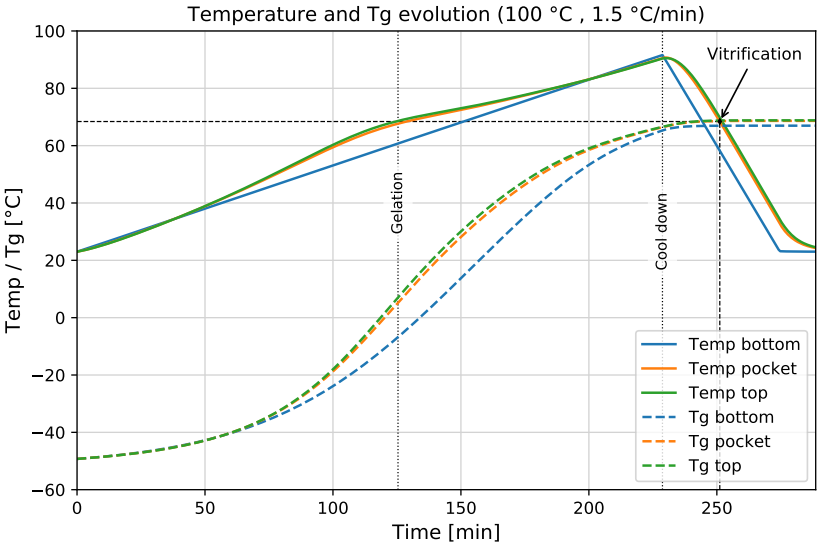

(b) Temperature and Tg evolution graph

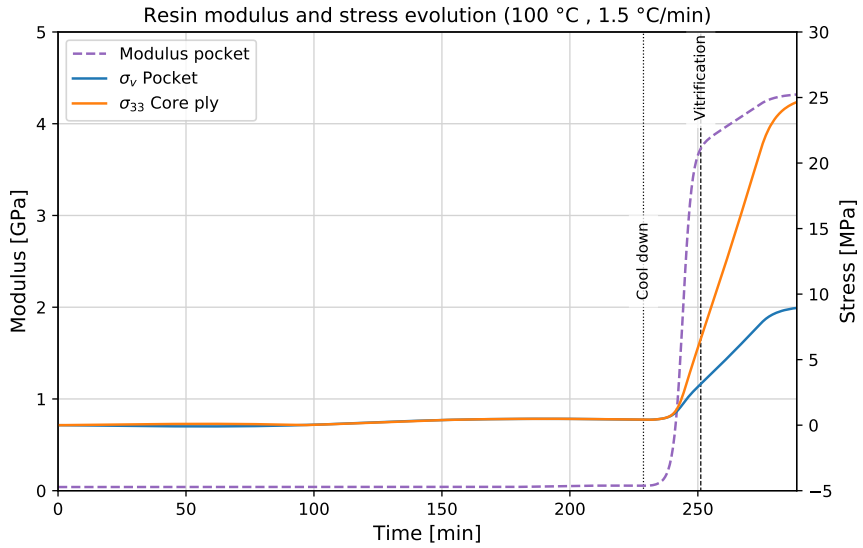

(c) Modulus and stress evolution graph

Figure G.5: Process influence output graphs. Dwell temp: 100 °C, Cool down rate: 1.5 °C/min

H

Influence of Stagger Distance. All 0° Layup - Output Graphs

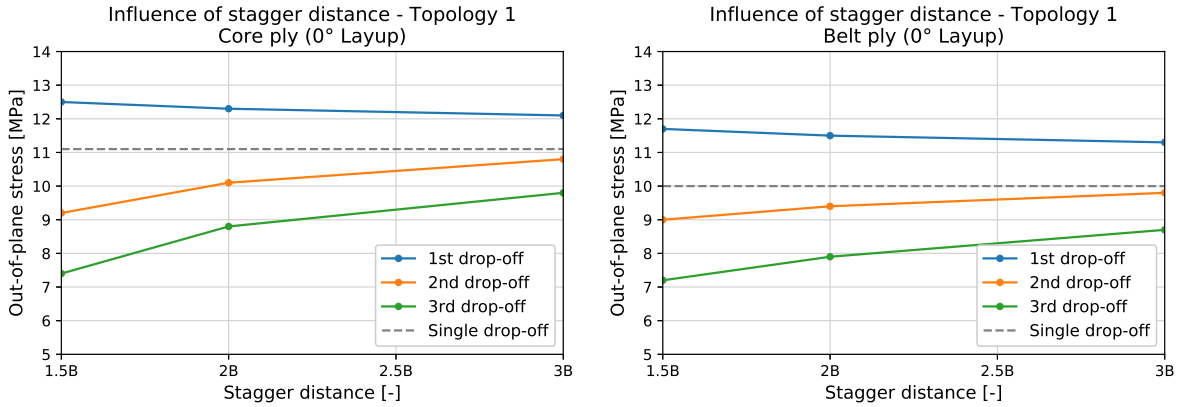

(a) Core-ply

(b) Belt-ply

Figure H.1: Influence of stagger distance on maximum out-of-plane stress within core- and belt ply. Multiple ply drop-off model with aspect ratio of 1/1.5. Topology 1. All 0° layup

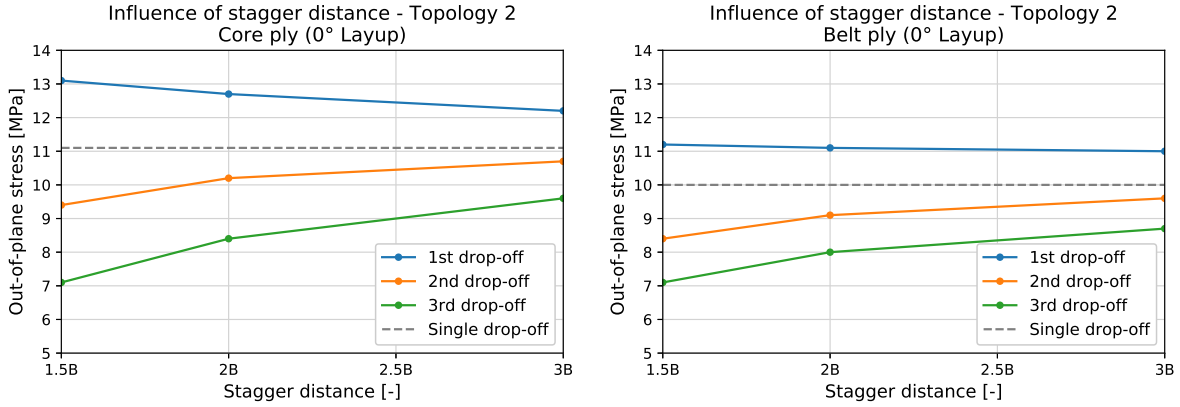

(a) Core-ply

(b) Belt-ply

Figure H.2: Influence of stagger distance on maximum out-of-plane stress within core- and belt ply. Multiple ply drop-off model with aspect ratio of 1/1.5. Topology 2. All 0° layup